A NUMERICAL INVESTIGATION OF A FLUTTER IN A TRANSONIC FAN

by

Kousuke Isomura

GTL Report #223 October 1996

GAS TURBINE LABORATORY
MASSACHUSETTS INSTITUTE OF TECHNOLOGY
CAMBRIDGE, MASSACHUSETTS

A NUMERICAL INVESTIGATION OF A FLUTTER IN A TRANSONIC FAN

by

Kousuke Isomura

GTL Report #223 October 1996

This research was mainly supported by Ishikawajima-Harima Heavy Industries Co., Ltd.

A Numerical Investigation of a Flutter in a Transonic Fan

by

Kousuke Isomura

The mechanism of the bending mode flutter of a modern transonic fan has been studied using a quasi-3D viscous unsteady code. The type of flutter in the scope of this research is that for a highly loaded blade with a tip relative Mach number just above unity, commonly referred to as transonic stall flutter. This type of flutter is often encountered in modern wide chord fans without a part span shroud.

The code written as a part of this research uses an upwinding scheme with Roe's 3rd-order flux differencing, and Johnson and King's turbulence model with later modification by Johnson and Coakley. An extensive series of code validation calculations were performed and the reliability of the code has been verified against data and other calculational procedures.

The calculations of the flow in this fan revealed that the source of the flutter is an oscillation of the passage shock, rather than a stall. As blade loading increases, the passage shock moves forward. Just before the passage shock unstarts, the stability of the passage shock decreases, and the shock oscillates at a large amplitude between unstarted position and started position with small blade vibration. The shock foot of the oscillating passage shock on the blade pressure surface exerts the dominant blade exciting force.

Acknowledgments

My project for studying on the transonic fan flutter took considerably longer than I expected due to a lack of computational power at hand. But because of this long period, I have come to know many excellent people both in academia and in daily life, who are now my big treasure.

First of all I'd like to thank Professor Giles, my first thesis adviser from whom I learned the pleasure of tackling unsteady fluid dynamics. Very sincere thanks to Professor Epstein, who took care of me through e-mail and committee meetings after Professor Giles moved to Oxford. Although isolated from the M.I.T. campus as a non-residential student, he motivated me in many ways to continue the research. I could always sense him through the computer screen, and without his exhortation I would not have completed this thesis. Also. I'd like to thank all of my thesis committee members, Professors Drela, Crawley, and Dr. Tan. All of them are wonderful and unique role models; from them I learned a lot of the important attitudes for doing research, and for being creative. Among these, very special thanks go to Dr. Choon S. Tan, who taught me about the vortical approach to fluid dynamics, attitudes as a graduate student, and good Chinese restaurants. Extra thanks to Professor Greitzer. I always tried hard to earn the respect of this man whom I regard highly.

I'd also like to thank all the members of the CFD lab (which existed while I was in MIT) and the Gas Turbine lab. Bob Haimes helped me learn about computers and configure my computer. Guppy and Eric taught me how to live free. Mike Aftosmis taught me this very important attitude in life, "If you don't try what you want to do now, you won't achieve anything your whole life." Soomyung influenced my attitude to express my feelings frankly. I'd also like to thank Dana, Andre, Elene, Missy, Dave^2,

Tom, Sandy, Brian for helping my daily work in classes and in the lab.

My special thanks go to Mike Aftosmis's family, Charles & Carol, Stephen, and his cousines Pete and Mathew Genta. They all encouraged me in my private life. Were not for this family, my life in the States must have been really painful, and many opportunities from living in the States would have been missed.

Among the many IHI co-workers who helped me, I'd like to acknowledge Mr. Murashima and Mr. Aono who supported sending me out to M.I.T., and Dr. Yasu and Ms. Toi who organized all the support I needed while I was in Boston. Dr. Hiroki and Dr. Henk gave me a lot of useful suggestions on writing the thesis.

Finally, and most of all, I'd like to thank my wife Naoko, and her mother Mrs. Oshima for encouraging me and supporting my family life. It was absolutely impossible for me to succeed without these people.

This thesis is dedicated to the memory of Dr. Keiichi Oshima, my late father in law.

This research was mainly funded by IHI Co., Ltd.

Contents

List of Figures

Nomenclature

A^+	van Driest damping constant
a	speed of sound
C	chord length
C_f	skin friction coefficient
D	near wall damping factor
e	total energy
F, G	flux vectors in directions normal to ξ and η direction cell faces
F_V, G_V	viscous flux vectors in directions normal to ξ and η direction cell faces
H	total enthalpy
H	boundary layer shape factor
h	enthalpy
h	passage height
I	unit matrix
i	grid number in ξ direction
J	Jacobian of a grid cell
$J^\pm$	downstream- and upstream-going characteristics
j	grid number in η direction
k	reduced frequency
Lm	dissipation length
M	Mach number
Pr	Prandtl number
p	pressure
Q	state vector = $(\rho, \rho u, \rho v, \rho e)^T$
R	universal gas constant
Re	Reynolds number
S	correction term vector for moving grids
s	entropy
T	temperature
t	time

u	velocity in x direction
u_b	outward velocity of the cell face
u_s	velocity normal to the cell face
u_τ	boundary-layer friction velocity
v	velocity in y direction
x	axial direction
y	circumferencial direction
y^+	boundary-layer inner coordinate
α	flow angle
β	inter-blade phase angle
γ	specific heat ratio
δ	boundary-layer thickness
η	grid direction approximately normal to the blade surface
κ	von Karman's constant ($= 0.41$)
Λ	eigenvalue matrix
λ_i	eigenvalue
μ	viscous coefficient
ν	kinematic viscosity
ν_t	turbulence kinematic viscosity
Ω	numerical cell control volume
ρ	density
τ	time after coordinate transformation
τ	shear stress
ϕ	characteristic variable
ξ	grid direction approximately parallel to the blade surface

Subscripts and superscripts

$(\ )^n_{i,j}$	value at position (i, j), time step n
$(\ )^p$	time step after ξ direction ADI, but before η direction ADI

$(\bar{\ })$	dimensional values
$(\ )_{in}$	inflow values
$(\ )_{out}$	outflow values
$(\ )_{wall}$	values on the wall
$(\ )_{m}$	values at maximum Reynolds stress height in the boundary layer
$(\ )_{i}$	values in the inner layer in the boundary layer
$(\ )_{o}$	values in the outer layer in the boundary layer
$(\ )_{eq}$	values of equilibrium boundary layer

Chapter 1
Introduction

1.1 Background

One of the most important requirements for jet engines for modern civil transport aircraft is high fuel efficiency at high-subsonic cruising speeds. This requirement results in high bypass-ratio transonic fans, which have very thin and flat blade sections. Such blades with less camber angle are more vulnerable to flow separation at high incidence angle than conventional low-speed blade sections. In a typical compressor/fan the incidence angle increases as the speed is reduced through the operating line. Hence, separation is more likely to be encountered in a transonic fan at a part speed operating point. When separation happens, the blade can experience stall flutter under certain conditions, as we can see as the hatched region-I and region-Ia in Fig. 1.1. In the figure, region-I is categorized as subsonic/transonic stall flutter, but the mechanism of the transonic stall flutter is not well understood yet. What we know of this flutter is that the oscillation mode is in bending, whereas classical stall flutter is predominantly in a torsional mode (a study by Sisto [21] shows less likelihood of classical stall flutter in a bending mode). Some reports point out the possibility of shock wave oscillation being involved [25, 28], but the mechanism of how the shock oscillation occurs is still unknown.

Since higher loading is desirable to achieve higher efficiency with less weight, engine designers often encounter stall flutter in prototype rigs. When they encounter stall flutter, the solution is to reduce the blade loading by reducing the stage pressure ratio, which also results in lower efficiency at the cruise point due to a shifting of the entire operating line towards the lower blade loading side. An alternative solution is thickening the blade, which also reduces the performance. They may use a sophisticated control system to avoid efficiency loss at the cruise point, but this will penalize the performance by increasing the weight and complexity of the system and is not likely to be used yet. Designers may also increase the number of blades to reduce the load of each blade, but this will again increase the weight and losses. Therefore, a better understanding of the flutter itself is needed first, in order to handle this problem with less penalty.

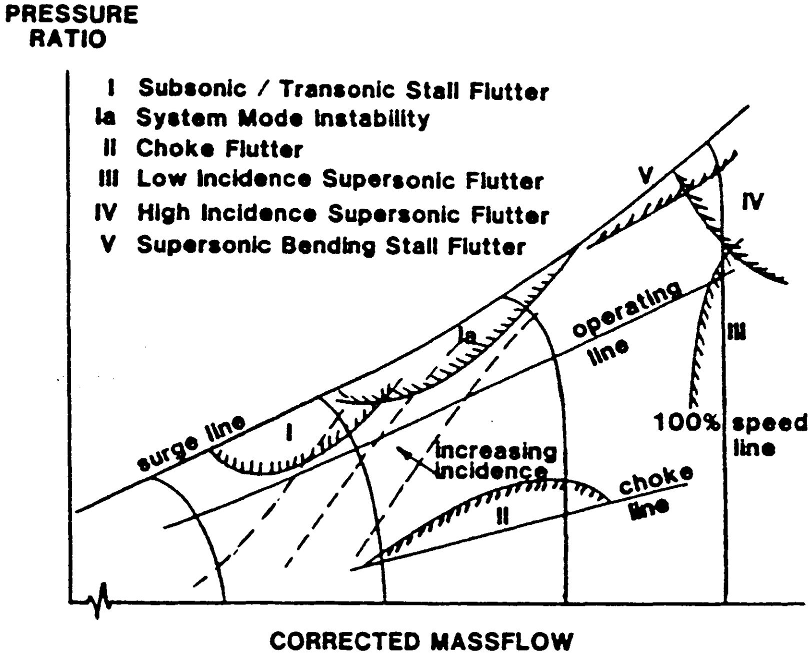

Figure 1.1: Typical axial compressor/fan characteristic map (*from Sisto*[20])

1.2 Previous Work

Because of the difficulty in observing and modeling the behavior of separated flow, there is less research on stall flutter than on flutter with attached flow. Sisto(1953) [21] predicted stall flutter by solving differential equations for blade vibration with aerodynamic forces, derived from subsonic static cascade experiments, used as an exciting force. He treated the effect of stall by describing the dynamic force coefficient versus angle of attack by a polynomial. In his calculation, he showed that the blades in a torsional mode will exhibit large unsteadiness but the one in bending mode may not flutter. Yashima and Tanaka (1977) [32] introduced a leading edge separation model into a potential flow calculation. The modeled separation area was extended far downstream. The match with experimental data was only qualitative. Chi(1980) [5] performed a calculation with a small perturbation equation and a separation model initiating from a certain fixed point on the blade suction surface. The matching of the reduced frequency for the largest negative damping was excellent but the magnitude of damping was not. Sisto, et al (1989) [22] adapted a vortex method used by Spalart [23] in a rotating stall calculation to the stall flutter case. They were very successful in simulating the evolution of separation, but all these calculations were for low subsonic stall flutter in torsional mode. None of them handled viscous effects nor compressibility effects, including shock waves.

For bending mode stall flutter of a transonic fan, Stargardter [25] of Pratt&Whitney performed thorough flutter measurements in a transonic fan rig and pointed out the possibility of shock wave oscillation contributing to the flutter. The flutter occurred only at conditions at which shock waves existed, however he could not find any evidence of the exciting aerodynamic force from the pressure measurements. Szechenyi [28] of ONERA performed two dimensional wind tunnel experiments for the cases in which a shock wave is attached to the leading edge of the blade, and found the shock wave oscillation contributed to a dominant exciting force. But the experiment with the shock wave detached was not successful because it was too difficult to attain a pitchwise periodic condition in the cascade. Also, in an unpublished two dimensional transonic wind tunnel test done by Isomura(1988), a detached shock impinging on the adjacent blade's suction surface was observed to exert a large exciting force (Fig. 1.2). However, due to the lack of a proper mechanism to synchronize the cascaded blades in bending mode oscillation and due to poor pitchwise repeatability of the flow in the cascade, the quality of the data was insufficient to show whether this is the true mechanism for this type of flutter. The experiment was performed by allowing the free oscillation of the cascaded blades, but the resulting inter-blade phase angle was far from uniform, passage to passage (Fig. 1.3). When the shock wave is detached from the leading edge of the blade, the unique incidence condition is lost, and the flow changes its angle continuously in the subsonic region behind the strong shock upstream of the cascade. In an annular cascade, the shock waves extend upstream, and the flow coming into each passage passes through the same number of shock waves to be deflected to the correct flow angle. But in a linear cascade, the flow coming into a passage will experience only the shock waves generated by the blades upstream of it, the blade immediately downstream of it, and the blade itself. Hence, the number of shock waves the flow passes through is different from passage to passage. When the shock is detached, it is not as stable as when it is attached, and so it is extremely difficult to obtain a pitchwise periodic condition in a linear cascade experiment even at steady flow. An annular cascade or rig test will solve such a problem, but it is very expensive to perform unsteady experiments in such facilities and also difficult to visualize the flow to clarify the aerodynamic mechanisms. Hence, numerical simulations are a very useful and feasible tool to study this phenomena, and the author decided to start a research of the flutter mechanisms by numerical simulations.

Joubert [15] of SNECMA performed an unsteady quasi-3D Euler code calculation, and showed that the shock oscillation is indeed a source of exciting force. Since this was an Euler calculation, the shock oscillation was all due to the change of the potential field due to the given blade oscillations and the effect of the shock boundary layer interaction was not included. Thus, he could show the possibility of the instability by the shock movement due to potential effects, but did not show whether it is the most important mechanism for the transonic flutter. In transonic fan with strong shock wave in the flowfield, shock-boundary layer interaction may play an important roll, and therefore the author decided to use a viscous algorithm for his numerical simulations.

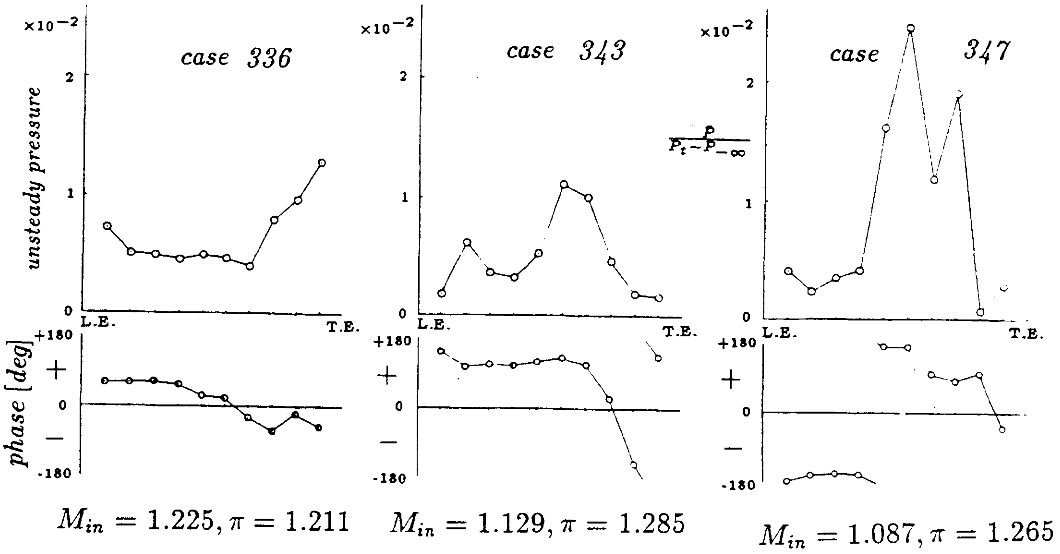

$M_{in} = 1.225, \pi = 1.211$ $M_{in} = 1.129, \pi = 1.285$ $M_{in} = 1.087, \pi = 1.265$

Figure 1.2: Amplitude & phase of the unsteady pressure on the suction surface of the blade (*from Isomura (1988)*)

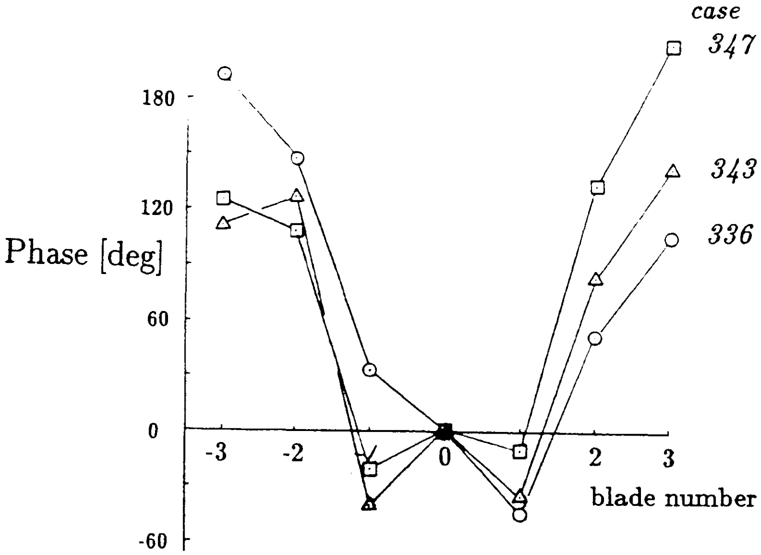

Figure 1.3: Resulting inter-blade phase angle of the cascaded blade in free oscillation (*from Isomura (1988)*)

1.3 Objectives of the thesis

The objective of the dissertation is to reveal the detailed mechanisms of the transonic high-loaded flutter observed in a IHI transonic fan rig at part speed. Some specific questions to answer in this research are as follows.

1. Is this flutter stall flutter or not?
2. Is shock wave playing important role in this flutter?
3. Is the effect of the Reynolds number large enough that the scaled rig test is not a valid method to check the flutter boundary of the engine?
4. Is the effect of the reduced frequency large so that increasing the natural frequency of the blade works effectively to avoid the flutter?
5. Are the mechanisms of this flutter unsteady so that quasi-steady analysis is not valid for this flutter?

Since the cascade test in transonic regime difficult to perform, and because the numerical simulation will facilitate us to study the effect of various aerodynamic parameter one by one, these objectives will be studied by the numerical simulation. One thing to emphasize in using the computational fluid dynamic code is that, it is important to validate the code thoroughly so that we can trust that the output of the computation corresponds to the results of an experiment.

1.4 Numerical approach of the research

The physics to be simulated in the numerical calculations include

1. shock movement,
2. shock-boundary layer interaction,

3. separation.

Therefore the basic equations should be the Navier-Stokes equations. To accurately simulate these phenomena

1. numerical scheme,
2. turbulence model,
3. transition model,
4. proper grid and,
5. proper boundary conditions,

are all important. At the beginning of research, rather than develop new methods for each of these items, the author considered it more important to select the best existing methods for each item. Furthermore he chose to write a code rather than using an existing code in order to have the flexibility to quickly modify the code during the research.

1.5 Construction of the thesis

The thesis consists of two parts. The first part describes the detail of the numerical code and its validation processes. The second part describes the results of the numerical simulation of the transonic flutter using this code.

Chapter 2 and 3 describes the basic equations and the detail of the numerical scheme, respectively. Chapter 4 describes the calculation grid, and Chapter 5 shows the accuracy of the code by a series of the validation calculations. In Chapter 6, numerical investigation of a flutter in a transonic fan is reported, and the effects of a variety of parameters are discussed. Conclusions and recommendations for future work are stated in Chapter 7.

Chapter 2

Basic equations

In a transonic fan flow, shock waves exist in a passage and its interaction with boundary layers on blade surfaces can generate unsteady forces. Since an object of this research is to find the effect of such an interaction on flutter, it is essential to start from viscous equations.

2.1 Non-dimensionalization

The variables are non-dimensionalized as follows:

$$\rho = \frac{\overline{\rho}}{\overline{\rho_{in}}}, \qquad u = \frac{\overline{u}}{\overline{a_{in}}}, \qquad v = \frac{\overline{v}}{\overline{a_{in}}}$$

$$e = \frac{\overline{e}}{\overline{a_{in}}^2}, \qquad p = \frac{\overline{p}}{\overline{\rho_{in} a_{in}}^2}, \qquad t = \frac{\overline{t}\,\overline{a_{in}}}{\overline{c}}$$

$$\mu = \frac{\overline{\mu}}{\overline{\mu_{in}}}, \qquad R_e = \frac{\overline{\rho_{in} a_{in} c}}{\overline{\mu_{in}}}, \qquad P_r = \frac{C_p \overline{\mu_{in}}}{\kappa} = \frac{\gamma R \overline{\mu_{in}}}{\kappa(\gamma - 1)}. \tag{2.1}$$

Hence, relations between some aerodynamic variables are written as follows:

$$p = \rho(\gamma - 1)(e - \frac{1}{2}(u^2 + v^2)) \tag{2.2}$$

$$H = e + \frac{p}{\rho} \tag{2.3}$$

$$a = \sqrt{\frac{\gamma p}{\rho}}. \tag{2.4}$$

2.2 Quasi-three-dimensional thin-shear-layer Reynolds-averaged Navier-Stokes equations

The basic equations to be solved are quasi-three-dimensional thin-shear-layer Reynolds-averaged Navier-Stokes equations. The equations before the thin-shear-layer approximation are as follows.

- Continuity

$$\frac{\partial h\rho}{\partial t} + \frac{\partial h\rho u}{\partial x} + \frac{\partial h\rho v}{\partial y} = 0 \tag{2.5}$$

- X - momentum

$$\frac{\partial h\rho u}{\partial t} + \frac{\partial h\rho u^2}{\partial x} + \frac{\partial h\rho uv}{\partial y} = -h\frac{\partial p}{\partial x} + \frac{1}{R_e}(\frac{\partial h\tau_{xx}}{\partial x} + \frac{\partial h\tau_{xy}}{\partial y}) \tag{2.6}$$

- Y - momentum

$$\frac{\partial h\rho v}{\partial t} + \frac{\partial h\rho uv}{\partial x} + \frac{\partial h\rho v^2}{\partial y} = -h\frac{\partial p}{\partial y} + \frac{1}{R_e}(\frac{\partial h\tau_{xy}}{\partial x} + \frac{\partial h\tau_{yy}}{\partial y}) \tag{2.7}$$

- Energy conservation

$$\frac{\partial h\rho e}{\partial t} + \frac{\partial h\rho ue}{\partial x} + \frac{\partial h\rho ve}{\partial y} = -\frac{\partial hup}{\partial x} - \frac{\partial hvp}{\partial y} + \frac{1}{R_e}(\frac{\partial hf}{\partial x} + \frac{\partial hg}{\partial y}) \tag{2.8}$$

These equations can be written in the matrix equation form as

$$\frac{\partial hQ}{\partial t} + \frac{\partial hF}{\partial x} + \frac{\partial hG}{\partial y} - \frac{1}{R_e}(\frac{\partial hF_V}{\partial x} + \frac{\partial hG_V}{\partial y}) = S \tag{2.9}$$

where

$$Q = \begin{pmatrix} \rho \\ \rho u \\ \rho v \\ \rho e \end{pmatrix}, \qquad F = \begin{pmatrix} \rho u \\ \rho u^2 + p \\ \rho uv \\ \rho u H \end{pmatrix}, \qquad G = \begin{pmatrix} \rho v \\ \rho uv \\ \rho v^2 + p \\ \rho v H \end{pmatrix} \tag{2.10}$$

$$F_V = \begin{pmatrix} 0 \\ \tau_{xx} \\ \tau_{xy} \\ f \end{pmatrix}, \qquad G_V = \begin{pmatrix} 0 \\ \tau_{xy} \\ \tau_{yy} \\ g \end{pmatrix}, \qquad S = \begin{pmatrix} 0 \\ p\frac{\partial h}{\partial x} \\ p\frac{\partial h}{\partial y} \\ 0 \end{pmatrix} \tag{2.11}$$

and

$$\tau_{xx} = \mu(4\frac{\partial u}{\partial x} - 2\frac{\partial v}{\partial y})/3 \tag{2.12}$$

$$\tau_{xy} = \mu(\frac{\partial u}{\partial y} + \frac{\partial v}{\partial x}) \tag{2.13}$$

$$\tau_{yy} = \mu(-2\frac{\partial u}{\partial x} + 4\frac{\partial v}{\partial y})/3 \tag{2.14}$$

$$f = u\tau_{xx} + v\tau_{xy} + \frac{\mu}{P_r(\gamma - 1)}\frac{\partial a^2}{\partial x} \tag{2.15}$$

$$g = u\tau_{xy} + v\tau_{yy} + \frac{\mu}{P_r(\gamma - 1)}\frac{\partial a^2}{\partial y}. \tag{2.16}$$

Since we do not want to restrict the grid to be aligned to the Cartesian co-ordinate system, we transform the basic equations to the arbitrary co-ordinate system ξ, η by

$$\begin{pmatrix} \frac{\partial}{\partial t} \\ \frac{\partial}{\partial x} \\ \frac{\partial}{\partial y} \end{pmatrix} = \begin{pmatrix} 1 & \frac{\partial \xi}{\partial t} & \frac{\partial \eta}{\partial t} \\ 0 & \frac{\partial \xi}{\partial x} & \frac{\partial \eta}{\partial x} \\ 0 & \frac{\partial \xi}{\partial y} & \frac{\partial \eta}{\partial y} \end{pmatrix} \begin{pmatrix} \frac{\partial}{\partial \tau} \\ \frac{\partial}{\partial \xi} \\ \frac{\partial}{\partial \eta} \end{pmatrix}. \tag{2.17}$$

The mapping from (τ,ξ,η) to (t,x,y) can be written as

$$\begin{pmatrix} \frac{\partial}{\partial \tau} \\ \frac{\partial}{\partial \xi} \\ \frac{\partial}{\partial \eta} \end{pmatrix} = \begin{pmatrix} 1 & \frac{\partial x}{\partial \tau} & \frac{\partial y}{\partial \tau} \\ 0 & \frac{\partial x}{\partial \xi} & \frac{\partial y}{\partial \xi} \\ 0 & \frac{\partial x}{\partial \eta} & \frac{\partial y}{\partial \eta} \end{pmatrix} \begin{pmatrix} \frac{\partial}{\partial t} \\ \frac{\partial}{\partial x} \\ \frac{\partial}{\partial y} \end{pmatrix}. \tag{2.18}$$

Because the mapping from (t,x,y) to (τ,ξ,η) is the inverse of the mapping from (τ,ξ,η) to (t,x,y), following relations are derived

$$\begin{pmatrix} 1 & \frac{\partial \xi}{\partial t} & \frac{\partial \eta}{\partial t} \\ 0 & \frac{\partial \xi}{\partial x} & \frac{\partial \eta}{\partial x} \\ 0 & \frac{\partial \xi}{\partial y} & \frac{\partial \eta}{\partial y} \end{pmatrix} = \begin{pmatrix} 1 & \frac{\partial x}{\partial \tau} & \frac{\partial y}{\partial \tau} \\ 0 & \frac{\partial x}{\partial \xi} & \frac{\partial y}{\partial \xi} \\ 0 & \frac{\partial x}{\partial \eta} & \frac{\partial y}{\partial \eta} \end{pmatrix}^{-1} = \frac{1}{J} \begin{pmatrix} J & \frac{\partial y}{\partial \tau}\frac{\partial x}{\partial \eta} - \frac{\partial x}{\partial \tau}\frac{\partial y}{\partial \eta} & \frac{\partial x}{\partial \tau}\frac{\partial y}{\partial \xi} - \frac{\partial y}{\partial \tau}\frac{\partial x}{\partial \xi} \\ 0 & \frac{\partial y}{\partial \eta} & -\frac{\partial y}{\partial \xi} \\ 0 & -\frac{\partial x}{\partial \eta} & \frac{\partial x}{\partial \xi} \end{pmatrix}, \tag{2.19}$$

where J is the determinant of the mapping from (τ,ξ,η) to (t,x,y)

$$J = \frac{\partial x}{\partial \xi}\frac{\partial y}{\partial \eta} - \frac{\partial x}{\partial \eta}\frac{\partial y}{\partial \xi}. \tag{2.20}$$

Then, the Navier-Stokes equations are

$$J\frac{\partial hQ}{\partial \tau} + \frac{\partial F^*}{\partial \xi} + \frac{\partial G^*}{\partial \eta} - \frac{1}{R_e}\left(\frac{\partial F_V^*}{\partial \xi} + \frac{\partial G_V^*}{\partial \eta}\right) = S^*, \tag{2.21}$$

where

$$F^* = h\left(F\frac{\partial y}{\partial \eta} - G\frac{\partial x}{\partial \eta}\right), \qquad G^* = h\left(-F\frac{\partial y}{\partial \xi} + G\frac{\partial x}{\partial \xi}\right) \tag{2.22}$$

$$F_V^* = h\left(F_V\frac{\partial y}{\partial \eta} - G_V\frac{\partial x}{\partial \eta}\right), \qquad G_V^* = h\left(-F_V\frac{\partial y}{\partial \xi} + G_V\frac{\partial x}{\partial \xi}\right) \tag{2.23}$$

$$S^* = \begin{pmatrix} 0 \\ p\left(\frac{\partial y}{\partial \eta}\frac{\partial h}{\partial \xi} - \frac{\partial y}{\partial \xi}\frac{\partial h}{\partial \eta}\right) \\ p\left(-\frac{\partial x}{\partial \eta}\frac{\partial h}{\partial \xi} + \frac{\partial x}{\partial \xi}\frac{\partial h}{\partial \eta}\right) \\ 0 \end{pmatrix} - \frac{\partial hQ}{\partial \xi}\left(\frac{\partial y}{\partial \tau}\frac{\partial x}{\partial \eta} - \frac{\partial x}{\partial \tau}\frac{\partial y}{\partial \eta}\right) - \frac{\partial hQ}{\partial \eta}\left(\frac{\partial x}{\partial \tau}\frac{\partial y}{\partial \xi} - \frac{\partial y}{\partial \tau}\frac{\partial x}{\partial \xi}\right). \tag{2.24}$$

In a high Reynolds number flow like the one in transonic fans, the viscous effect due to the shear normal to the flow direction is dominant and that due to the streamwise gradient of the velocity can be neglected. So if we choose the grid system to be approximately aligned to the flow direction in the boundary layer and in the wake, we can simplify the basic equation by neglecting the streamwise shear stress term. This is called the thin-shear-layer approximation, and the basic equations are written as follows:

$$J\frac{\partial hQ}{\partial \tau} + \frac{\partial F^*}{\partial \xi} + \frac{\partial G^*}{\partial \eta} - \frac{\partial V^*}{\partial \eta} = S^* \tag{2.25}$$

$$V^* \equiv \frac{G_V^*}{R_e} = \frac{1}{R_e}\begin{pmatrix} 0 \\ \mu\frac{\partial u}{\partial \eta} \\ \mu\frac{\partial v}{\partial \eta} \\ \mu\frac{\partial}{\partial \eta}(\frac{1}{2}u^2 + \frac{1}{2}v^2 + \frac{a^2}{(\gamma-1)P_r}) \end{pmatrix}. \tag{2.26}$$

Now, rewrite Eq.(2.25) in "conservation form" to allow the discontinuities at shock waves by integrating the equations over the computational cell

$$\int\int_\Omega Jh\frac{\partial Q}{\partial \tau}d\xi d\eta = -\int\int_\Omega \left[\frac{\partial F^*}{\partial \xi} + \frac{\partial (G^* - V^*)}{\partial \eta} - S^*\right] d\xi d\eta. \tag{2.27}$$

Since the Jacobian is equivalent to the computational cell area, the left hand side (L.H.S.) of these equations can be rewritten by using $\overline{Q}$, the average value of Q in the control volume

$$J\frac{dh\bar{Q}}{d\tau} = -\oint_{\partial\Omega}(F^* d\eta - (G^* - V^*)d\xi) + \int\int S^* d\xi d\eta. \tag{2.28}$$

Note that the area of the computational cell in (ξ, η) coordinate is unity. Also note that the sign in form of $(G^* - V^*)$ is flipped due to the counter-clockwise line integral.

The quasi-three-dimensional assumption was employed because the primary objective of this research is to see the detail of the phenomena at the point where the detached shockwave hits the suction surface of the adjacent blade. There may some objections to this assumption since the shock oscillation in a real fan may be smaller than that in the quasi-three-dimensional calculation because there is a relief effect of the unsteady pressure through the subsonic part which always exist at the hub.

In the rest of the thesis, the time variable will be written as t instead of τ to avoid confusion with shear stress.

Chapter 3

Numerical schemes

In this chapter, detail of the numerical scheme, boundary conditions, turbulence model, and transition model are explained.

3.1 Upwinding ADI scheme

The basic scheme used in this research is the upwinding Alternating Direction Implicit (ADI) scheme formulated by Giles [10]. This scheme is similar to the ADI scheme used by Rai [16] except the difference terms of the other direction are not neglected and are kept in the right hand side of the equations.

The implicit scheme was chosen because of its unconditional stability. In time-accurate, viscous, transonic, turbulent-flow calculations, the grid size in the boundary layer has to be extremely small to resolve the laminar sub-layer which is essential for accurate skin-friction calculation and shock-boundary layer interaction simulation. In such a case, explicit schemes for which the CFL number is limited by unity, take a couple of orders of magnitude longer calculation time than implicit schemes and may not be practical. In implicit schemes, the code can be run with a CFL number larger than 1000, based on the smallest grid size.

An upwinding scheme is chosen because of its ability to capture shockwaves without excessive smearing. The capability to simulate the shock behavior accurately is a very important aspect of the current code.

The basic partial differential equation (PDE) (Eq.(2.25)) is discretized in implicit form by using backward Euler time differencing as

$$\begin{aligned}&\frac{J^{n+1}_{i,j}h^{n+1}_{i,j}}{\Delta t}(Q^{n+1}_{i,j} - Q^{n}_{i,j})+\\&(F^{*n+1}_{i+\frac{1}{2},j} - F^{*n+1}_{i-\frac{1}{2},j}) + (G^{*n+1}_{i,j+\frac{1}{2}} - G^{*n+1}_{i,j-\frac{1}{2}}) - (V^{*n+1}_{i,j+\frac{1}{2}} - V^{*n+1}_{i,j-\frac{1}{2}}) \quad = \quad S^{*n+1}_{i,j}.\end{aligned} \tag{3.1}$$

This non-linear equations cannot be solved directly. The way to solve this problem is to linearize the equations by taking delta-form as follows:

$$\begin{aligned}&\left\{\left(\frac{J_{i,j}h_{i,j}I}{\Delta t}\right)^{n+1}\right.\\&\left.+\left(\frac{\partial F^*_{i+\frac{1}{2},j}}{\partial Q_{i,j}} - \frac{\partial F^*_{i-\frac{1}{2},j}}{\partial Q_{i,j}} + \frac{\partial G^*_{i,j+\frac{1}{2}}}{\partial Q_{i,j}} - \frac{\partial G^*_{i,j-\frac{1}{2}}}{\partial Q_{i,j}} - \frac{\partial V^*_{i,j+\frac{1}{2}}}{\partial Q_{i,j}} + \frac{\partial V^*_{i,j-\frac{1}{2}}}{\partial Q_{i,j}}\right)^n\right\}\Delta Q^{n+1}_{i,j}\\&+\left(\frac{\partial F^*_{i+\frac{1}{2},j}}{\partial Q_{i+1,j}}\right)^n \Delta Q^{n+1}_{i+1,j} - \left(\frac{\partial F^*_{i-\frac{1}{2},j}}{\partial Q_{i-1,j}}\right)^n \Delta Q^{n+1}_{i-1,j}\\&+\left(\frac{\partial G^*_{i,j+\frac{1}{2}}}{\partial Q_{i,j+1}} - \frac{\partial V^*_{i,j+\frac{1}{2}}}{\partial Q_{i,j+1}}\right)^n \Delta Q^{n+1}_{i,j+1} - \left(\frac{\partial G^*_{i,j-\frac{1}{2}}}{\partial Q_{i,j-1}} - \frac{\partial V^*_{i,j-\frac{1}{2}}}{\partial Q_{i,j-1}}\right)^n \Delta Q^{n+1}_{i,j-1} \quad =\\&-(F^*_{i+\frac{1}{2},j} - F^*_{i-\frac{1}{2},j})^n - (G^*_{i,j+\frac{1}{2}} - G^*_{i,j-\frac{1}{2}})^n + (V^*_{i,j+\frac{1}{2}} - V^*_{i,j-\frac{1}{2}})^n + S^{*n}_{i,j},\end{aligned} \tag{3.2}$$

where

$$\Delta Q^{n+1}_{i,j} = Q^{n+1}_{i,j} - Q^{n}_{i,j}. \tag{3.3}$$

Note that the effect of the moving grids are included in the last term in the right hand side (R.H.S.) and in the flux terms in the left hand side (L.H.S.) of the equations. The detail of the treatment of the moving grid is discussed later. These basic difference equations were solved by splitting the implicit matrix inversion calculations in two steps; one step for each dimension. This is the ADI scheme and the basic equations were rewritten as follows:

$$\begin{aligned}&\left\{\left(\frac{J}{\Delta t}\right)^{n+1} + \left(\frac{\partial F^*_{i+\frac{1}{2},j}}{\partial Q_{i,j}} - \frac{\partial F^*_{i-\frac{1}{2},j}}{\partial Q_{i,j}}\right)^n\right\}\Delta Q^{n+1(p1)}_{i,j}\\&+\frac{\partial F^*_{i+\frac{1}{2},j}}{\partial Q_{i+1,j}}^n \Delta Q^{n+1\ (p1)}_{i+1,j} + \frac{\partial F^*_{i-\frac{1}{2},j}}{\partial Q_{i-1,j}}^n \Delta Q^{n+1\ (p1)}_{i-1,j} \quad =\\&-\left(F^*_{i+\frac{1}{2},j} - F^*_{i-\frac{1}{2},j}\right)^n - \left(G^*_{i,j+\frac{1}{2}} - G^*_{i,j-\frac{1}{2}}\right)^n + \left(V^*_{i,j+\frac{1}{2}} - V^*_{i,j-\frac{1}{2}}\right)^n + S^{*n}_{i,j}\end{aligned}$$

$$
-\left(\frac{\partial G^{*}_{i,j+\frac{1}{2}}}{\partial Q_{i,j}} - \frac{\partial G^{*}_{i,j-\frac{1}{2}}}{\partial Q_{i,j}} - \frac{\partial V^{*}_{i,j+\frac{1}{2}}}{\partial Q_{i,j}} + \frac{\partial V^{*}_{i,j-\frac{1}{2}}}{\partial Q_{i,j}}\right)^{n} \Delta Q_{i,j}^{n+1(p0)}
$$

$$
-\left(\frac{\partial G^{*}_{i,j+\frac{1}{2}}}{\partial Q_{i,j+1}} - \frac{\partial V^{*}_{i,j+\frac{1}{2}}}{\partial Q_{i,j+1}}\right)^{n} \Delta Q_{i,j+1}^{n+1\ (p0)} - \left(\frac{\partial G^{*}_{i,j-\frac{1}{2}}}{\partial Q_{i,j-1}} - \frac{\partial V^{*}_{i,j-\frac{1}{2}}}{\partial Q_{i,j-1}}\right)^{n} \Delta Q_{i,j-1}^{n+1\ (p0)} \qquad (3.4)
$$

$$
\left\{\left(\frac{Jh}{\Delta t}\right)^{n+1} + \left(\frac{\partial G^{*}_{i,j+\frac{1}{2}}}{\partial Q_{i,j}} - \frac{\partial G^{*}_{i,j-\frac{1}{2}}}{\partial Q_{i,j}} - \frac{\partial V^{*}_{i,j+\frac{1}{2}}}{\partial Q_{i,j}} + \frac{\partial V^{*}_{i,j-\frac{1}{2}}}{\partial Q_{i,j}}\right)^{n}\right\} \Delta Q_{i,j}^{n+1(p0)}
$$

$$
+\left(\frac{\partial G^{*}_{i,j+\frac{1}{2}}}{\partial Q_{i,j+1}} - \frac{\partial V^{*}_{i,j+\frac{1}{2}}}{\partial Q_{i,j+1}}\right)^{n} \Delta Q_{i,j+1}^{n+1\ (p0)} + \left(\frac{\partial G^{*}_{i,j-\frac{1}{2}}}{\partial Q_{i,j-1}} - \frac{\partial V^{*}_{i,j-\frac{1}{2}}}{\partial Q_{i,j-1}}\right)^{n} \Delta Q_{i,j-1}^{n+1\ (p0)} \quad =
$$

$$
-\left(F^{*}_{i+\frac{1}{2},j} - F^{*}_{i-\frac{1}{2},j}\right)^{n} - \left(G^{*}_{i,j+\frac{1}{2}} - G^{*}_{i,j-\frac{1}{2}}\right)^{n} + \left(V^{*}_{i,j+\frac{1}{2}} - V^{*}_{i,j-\frac{1}{2}}\right)^{n} + S^{*n}_{i,j}
$$

$$
-\left(\frac{\partial F^{*}_{i+\frac{1}{2},j}}{\partial Q_{i,j}} - \frac{\partial F^{*}_{i-\frac{1}{2},j}}{\partial Q_{i,j}}\right)^{n} \Delta Q_{i,j}^{n+1(p1)}
$$

$$
-\frac{\partial F^{*}_{i+\frac{1}{2},j}}{\partial Q_{i+1,j}}^{n} \Delta Q_{i+1,j}^{n+1\ (p1)} - \frac{\partial F^{*}_{i-\frac{1}{2},j}}{\partial Q_{i-1,j}}^{n} \Delta Q_{i-1,j}^{n+1\ (p1)}. \qquad (3.5)
$$

The superscript ($)^{(p0)}$,and ($)^{(p1)}$ indicate the interim time steps after η sweep and ξ sweep, respectively. To calculate these equations, $\Delta Q_{i,j}^{n+1(p0)}$ is set to zero

$$
\Delta Q_{i,j}^{n+1(p0)} = 0, \qquad (3.6)
$$

at the beginning of a time step. ΔQ^{n+1p1} is calculated by ξ sweep calculation of Eq.(3.4), and the results are used in Eq.(3.5) to calculate ΔQ^{n+1p0} by η sweep. The calculations of these two equations will be repeated for a specified number of sub-iterations, and the final result of the time step is attained by

$$
\Delta Q_{i,j}^{n+1} = \Delta Q_{i,j}^{n+1(p0)}, \qquad (3.7)
$$

at the end of the time step.

The 1/2s in the subscripts indicate that the value is evaluated on the face of the calculation cells. This is done by mass-weighted averages as follows:

$$\begin{aligned}
\rho_{i+\frac{1}{2}} &= \frac{\rho_{i+1} + \rho_i}{2} \\
u_{i+\frac{1}{2}} &= \frac{\sqrt{\rho_{i+1}}u_{i+1} + \sqrt{\rho_i}u_i}{\sqrt{\rho_{i+1}} + \sqrt{\rho_i}} \\
v_{i+\frac{1}{2}} &= \frac{\sqrt{\rho_{i+1}}v_{i+1} + \sqrt{\rho_i}v_i}{\sqrt{\rho_{i+1}} + \sqrt{\rho_i}} \\
H_{i+\frac{1}{2}} &= \frac{\sqrt{\rho_{i+1}}H_{i+1} + \sqrt{\rho_i}H_i}{\sqrt{\rho_{i+1}} + \sqrt{\rho_i}}.
\end{aligned} \tag{3.8}$$

The ADI line calculations were executed as shown in Fig. 3.1. The ξ direction calculations were done first and then η direction calculations. The η direction ADIs in the downstream region of the blade were shifted to make the wake boundary just ordinary points.

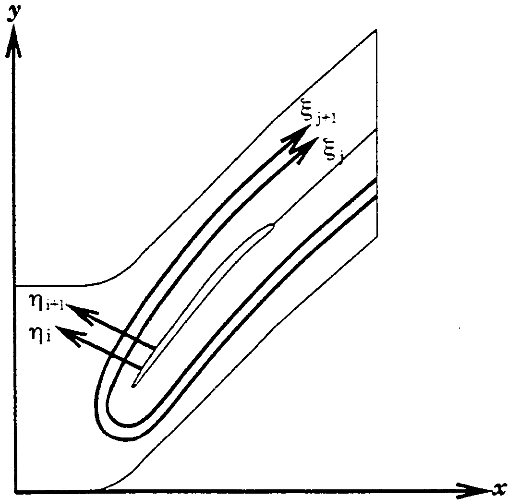

Figure 3.1: The ADI line calculation procedure

The J in Eq.(3.5) are the Jacobians, which state the relation between $x - y$ coordinates and $\xi - \eta$ coordinates. In the current case, the $\xi - \eta$ coordinate system is a rectangular coordinate system with unit spacing both in ξ and η. Thus the Jacobians are simply the area of the computational cells

$$J = x_\xi y_\eta - x_\eta y_\xi \tag{3.9}$$

$$= \quad ((x_{i+1,j} - x_{i-1,j})(y_{i,j+1} - y_{i,j-1}) - (x_{i,j+1} - x_{i,j-1})(y_{i+1,j} - y_{i-1,j}))/4. \tag{3.10}$$

Each Q derivative term of inviscid fluxes in the L.H.S. of the equations can be decomposed into three matrices by similarity transform as in

$$\begin{aligned} A &= \frac{\partial F^*}{\partial Q} \quad \text{or,} \quad \frac{\partial G^*}{\partial Q} && (3.11) \\ &= \frac{\partial F}{\partial Q}\Delta y' - \frac{\partial G}{\partial Q}\Delta x' \\ &\qquad - \vec{u_b} \cdot \vec{n} I \Delta s' && (3.12) \\ &= T^{-1}\Lambda T, && (3.13) \end{aligned}$$

where

$$A = \Delta s' \begin{pmatrix} 0 & 0 & 0 & 0 \\ -u_n u + \frac{\gamma-1}{2}(u^2+v^2)n_x & u_n - (\gamma-2)un_x & un_y - (\gamma-1)vn_x & (\gamma-1)n_x \\ -u_n v + \frac{\gamma-1}{2}(u^2+v^2)n_y & vn_x - (\gamma-1)un_y & u_n - (\gamma-2)vn_y & (\gamma-1)n_y \\ -u_n H + \frac{\gamma-1}{2}(u^2+v^2)u_n & Hn_x - (\gamma-1)uu_n & Hn_y - (\gamma-1)vu_n & \gamma u_n \end{pmatrix} - \vec{u_b} \cdot \vec{n} I \Delta s' \tag{3.14}$$

and

$$\begin{aligned} u_n &= un_x + vn_y \\ u_t &= -un_y + vn_x && (3.15) \\ n_x &= \frac{\Delta y'}{\Delta s'} \\ n_y &= -\frac{\Delta x'}{\Delta s'} && (3.16) \\ \Delta s' &= \sqrt{\Delta x'^2 + \Delta y'^2} \\ \Delta x' &= \frac{h_{i,j}}{2}(x_{i+1,j} - x_{i-1,j}) \quad \text{,or} \quad \frac{h_{i,j}}{2}(x_{i,j+1} - x_{i,j-1}) \end{aligned}$$

$$\Delta y' = \frac{h_{i,j}}{2}(y_{i+1,j} - y_{i-1,j}) \quad \text{,or} \quad \frac{h_{i,j}}{2}(y_{i,j+1} - y_{i,j-1}), \tag{3.17}$$

and where

$$T = \begin{pmatrix} 1 & 1 & 1 & 1 \\ u - an_x & u & -an_y & u + an_x \\ v - an_y & v & an_x & v + an_y \\ H - u_n a & \frac{1}{2}(u^2 + v^2) & u_t a & H + u_n a \end{pmatrix} \tag{3.18}$$

$$T^{-1} = \frac{1}{a^2} \begin{pmatrix} \frac{1}{2}u_n a + \frac{\gamma-1}{4}(u^2 + v^2) & -\frac{1}{2}an_x - \frac{\gamma-1}{2}u & -\frac{1}{2}an_y - \frac{\gamma-1}{2}v & \frac{\gamma-1}{2} \\ a^2 - \frac{\gamma-1}{2}(u^2 + v^2) & (\gamma - 1)u & (\gamma - 1)v & -(\gamma - 1) \\ -u_t a & -au_y & an_x & 0 \\ -\frac{1}{2}u_n a + \frac{\gamma-1}{4}(u^2 + v^2) & \frac{1}{2}an_x - \frac{\gamma-1}{2}u & \frac{1}{2}an_y - \frac{\gamma-1}{2}v & \frac{\gamma-1}{2} \end{pmatrix} \tag{3.19}$$

$$\Lambda = \begin{pmatrix} \lambda_1 & 0 & 0 & 0 \\ 0 & \lambda_2 & 0 & 0 \\ 0 & 0 & \lambda_3 & 0 \\ 0 & 0 & 0 & \lambda_4 \end{pmatrix} \tag{3.20}$$

$$\begin{aligned} \lambda_1 &= \Delta s'((u_n - a) &&- \vec{u_b} \cdot \vec{n}) \\ \lambda_2 &= \Delta s'(u_n &&- \vec{u_b} \cdot \vec{n}) \\ \lambda_3 &= \Delta s'(u_n &&- \vec{u_b} \cdot \vec{n}) \\ \lambda_4 &= \Delta s'((u_n + a) &&- \vec{u_b} \cdot \vec{n}). \end{aligned} \tag{3.21}$$

$\Delta s'$ is the length of the calculation cell face. Note that the additional terms due to the moving grid, which appeared only in the S^* term of the original Navier-Stokes equations Eq.(2.28), are implemented also in Q derivative terms of inviscid fluxes of the L.H.S. of the discretized equations.

The four numbers in the matrix Λ are the eigenvalues of the wave system, corresponding to the upstream going pressure wave $(u-a)$, the downstream going pressure wave $(u+a)$, the vorticity wave (u), and the entropy wave (u).

The eigenvalue matrices can be split into those for positive eigenvalues and those for negative eigenvalues as in

$$
\begin{aligned}
\Lambda^{+} &= diag(\max(0,\lambda_i)) \\
\Lambda^{-} &= diag(\min(0,\lambda_i)).
\end{aligned} \tag{3.22}
$$

Using this notation, the Q derivative terms of the fluxes can be split into positive and negative matrices

$$
A^{\pm} = T^{-1}\Lambda^{\pm}T. \tag{3.23}
$$

Hence, the Q derivative terms of the fluxes in Eq.(3.5) are

$$
\begin{aligned}
\frac{\partial F^{*}_{i+\frac{1}{2},j}}{\partial Q_{i,j}} &= T^{-1}_{i+\frac{1}{2},j}\Lambda^{+}_{i+\frac{1}{2},j}T_{i+\frac{1}{2},j} \equiv \left(\frac{\partial F^{*}}{\partial Q}\right)^{+}_{i+\frac{1}{2},j} \\
\frac{\partial F^{*}_{i-\frac{1}{2},j}}{\partial Q_{i,j}} &= T^{-1}_{i-\frac{1}{2},j}\Lambda^{-}_{i-\frac{1}{2},j}T_{i-\frac{1}{2},j} \equiv \left(\frac{\partial F^{*}}{\partial Q}\right)^{-}_{i-\frac{1}{2},j} \\
\frac{\partial G^{*}_{i,j+\frac{1}{2}}}{\partial Q_{i,j}} &= T^{-1}_{i,j+\frac{1}{2}}\Lambda^{+}_{i,j+\frac{1}{2}}T_{i,j+\frac{1}{2}} \equiv \left(\frac{\partial G^{*}}{\partial Q}\right)^{+}_{i,j+\frac{1}{2}} \\
\frac{\partial G^{*}_{i,j-\frac{1}{2}}}{\partial Q_{i,j}} &= T^{-1}_{i,j-\frac{1}{2}}\Lambda^{-}_{i,j-\frac{1}{2}}T_{i,j-\frac{1}{2}} \equiv \left(\frac{\partial G^{*}}{\partial Q}\right)^{-}_{i,j-\frac{1}{2}}.
\end{aligned} \tag{3.24}
$$

The fluxes F^{*}, G^{*} are defined as follows:

$$
\begin{aligned}
F^{*n}_{i+\frac{1}{2},j} &= \frac{1}{2}(F^{n}_{i,j}+F^{n}_{i+1,j})\Delta y_{i+\frac{1}{2},j} - \frac{1}{2}(G^{n}_{i,j}+G^{n}_{i+1,j})\Delta x_{i+\frac{1}{2},j} \\
&\quad -\frac{\sigma}{2}\left(\left(\frac{\partial F^{*}}{\partial Q}\right)^{+}_{i+\frac{1}{2},j} - \left(\frac{\partial F^{*}}{\partial Q}\right)^{-}_{i+\frac{1}{2},j}\right)(Q^{n}_{i+1,j}-Q^{n}_{i,j}) \\
&\quad -\frac{1-\sigma}{6}\left(\frac{\partial F^{*}}{\partial Q}\right)^{+}_{i+\frac{1}{2},j}(Q^{n}_{i+1,j}-2Q^{n}_{i,j}+Q^{n}_{i-1,j}) \\
&\quad -\frac{1-\sigma}{6}\left(\frac{\partial F^{*}}{\partial Q}\right)^{-}_{i+\frac{1}{2},j}(Q^{n}_{i+2,j}-2Q^{n}_{i+1,j}+Q^{n}_{i,j}),
\end{aligned} \tag{3.25}
$$

$$
\begin{aligned}
{G^{*}}^{n}_{i,j+\frac{1}{2}} &= \frac{1}{2}(F^n_{i,j} + F^n_{i,j+1})\Delta y_{i,j+\frac{1}{2}} - \frac{1}{2}(G^n_{i,j} + G^n_{i,j+1})\Delta x_{i,j+\frac{1}{2}} \\
&\quad -\frac{\sigma}{2}\left(\left(\frac{\partial G^*}{\partial Q}\right)^{+}_{i,j+\frac{1}{2}} - \left(\frac{\partial G^*}{\partial Q}\right)^{-}_{i,j+\frac{1}{2}}\right)(Q^n_{i+1,j} - Q^n_{i,j}) \\
&\quad -\frac{1-\sigma}{6}\left(\frac{\partial F^*}{\partial Q}\right)^{+}_{i,j+\frac{1}{2}}(Q^n_{i,j+1} - 2Q^n_{i,j} + Q^n_{i,j-1}) \\
&\quad -\frac{1-\sigma}{6}\left(\frac{\partial F^*}{\partial Q}\right)^{-}_{i,j+\frac{1}{2}}(Q^n_{i,j+2} - 2Q^n_{i,j+1} + Q^n_{i,j}).
\end{aligned}
\tag{3.26}
$$

When $\sigma = 0$, these are Roe's 3rd-order flux differencing [18]. When $\sigma = 1$, these fluxes are first order.

Second order central differencing was used for the viscous terms

$$
V^*_{i,j+\frac{1}{2}} = \frac{\mu_{i,j} + \mu_{i,j+1}}{2}\frac{\Delta s'}{\Delta n}\begin{pmatrix} 0 \\ u_{i,j+1} - u_{i,j} \\ v_{i,j+1} - v_{i,j} \\ \left(\frac{1}{2}u^2_{i,j+1} + \frac{1}{2}v^2_{i,j+1} + \frac{1}{(\gamma-1)P_r}a^2_{i,j+1}\right) \\ \quad - \left(\frac{1}{2}u^2_{i,j} + \frac{1}{2}v^2_{i,j} + \frac{1}{(\gamma-1)P_r}a^2_{i,j}\right) \end{pmatrix}. \tag{3.27}
$$

Hence, the Q derivatives of the viscous fluxes are

$$
\frac{\partial V^*_{i,j+\frac{1}{2}}}{\partial Q_{i,j}} = \frac{\mu_{i,j} + \mu_{i,j+1}}{2}\frac{\Delta s'}{\Delta n}\begin{pmatrix} 0 & 0 & 0 & 0 \\ -\frac{u_{i,j}}{\rho_{i,j}} & -\frac{1}{\rho_{i,j}} & 0 & 0 \\ -\frac{v_{i,j}}{\rho_{i,j}} & 0 & -\frac{1}{\rho_{i,j}} & 0 \\ -\alpha_1 & -\alpha_2 & -\alpha_3 & -\alpha_4 \end{pmatrix}, \tag{3.28}
$$

where

$$
\begin{aligned}
\alpha_1 &= -\frac{u^2_{i,j}+v^2_{i,j}}{\rho_{i,j}} - \frac{\gamma}{(\gamma-1)P_r}\left(\frac{1}{\rho_{i,j}}\frac{\partial p_{i,j}}{\partial \rho_{i,j}} - \frac{p_{i,j}}{\rho^2_{i,j}}\right) \\
\alpha_2 &= \frac{u_{i,j}}{\rho_{i,j}} + \frac{\gamma}{(\gamma-1)P_r}\frac{1}{\rho_{i,j}}\frac{\partial p_{i,j}}{\partial \rho_{i,j} u_{i,j}} \\
\alpha_3 &= \frac{v_{i,j}}{\rho_{i,j}} + \frac{\gamma}{(\gamma-1)P_r}\frac{1}{\rho_{i,j}}\frac{\partial p_{i,j}}{\partial \rho_{i,j} v_{i,j}} \\
\alpha_4 &= \frac{\gamma}{(\gamma-1)P_r}\frac{1}{\rho_{i,j}}\frac{\partial p_{i,j}}{\partial \rho_{i,j} e_{i,j}}.
\end{aligned}
\tag{3.29}
$$

3.2 Sonic point treatment

In the upwinding scheme, the information corresponding to each eigenvalue propagates in the direction of the sign of the eigenvalues, with the speed of the magnitude of the eigenvalues. Hence, across the point at which the sign of eigenvalue changes, the direction of the eigenvalues are opposite and there can be no information exchange. In such a case, a flow variable can be discontinuous. This can be physically true in the case of compression wave, which is a shockwave. But in the case of expansion wave this is not true. A straight implementation of the upwinding scheme will cause an "expansion shock" at the sonic point. However, in physical reality an expansion will take place isentropically, requiring the exchange of the information in both directions. So the scheme needs a correction to simulate this phenomena. The basic idea of the sonic point treatment is illustrated in Fig. 3.2. The eigenvalues are split into positive and negative parts while keeping the sum of these two parts equal to the one found by straight application of the upwinding scheme. We found that this treatment should be applied not only to the sonic point, but over several grid cells on both sides of the sonic point in order to achieve practical stability. The best number of cells was found to be three by numerical experiments.

The numerical formula used for the sonic point treatment was thus

$$\begin{aligned} \lambda^+ &= \max(0,\lambda) + 0.5\max(0, 3\Delta\lambda - |\lambda|) \\ \lambda^- &= \min(0,\lambda) - 0.5\max(0, 3\Delta\lambda - |\lambda|), \end{aligned} \tag{3.30}$$

where

$$\Delta\lambda = \lambda_{i+1} - \lambda_i. \tag{3.31}$$

Mathematically, it looks better to use a smooth function as

$$\lambda^{\pm} = \pm 2\frac{(\widehat{\lambda^{\pm}})^2}{\Delta\lambda}, \tag{3.32}$$

where

$$\widehat{\lambda^{\pm}} = \frac{1}{2}(\lambda_{i+\frac{1}{2}} \pm \frac{\delta\lambda}{2}), \tag{3.33}$$

which van Leer, Lee, and Powell proposed [29] (Fig. 3.2). But numerically Eq.(3.30) is more robust since there is no division by a small number. The difference of the formulation is negligible since the positive part and the negative part are continuous functions, and their sum is kept equal to the correct eigenvalue.

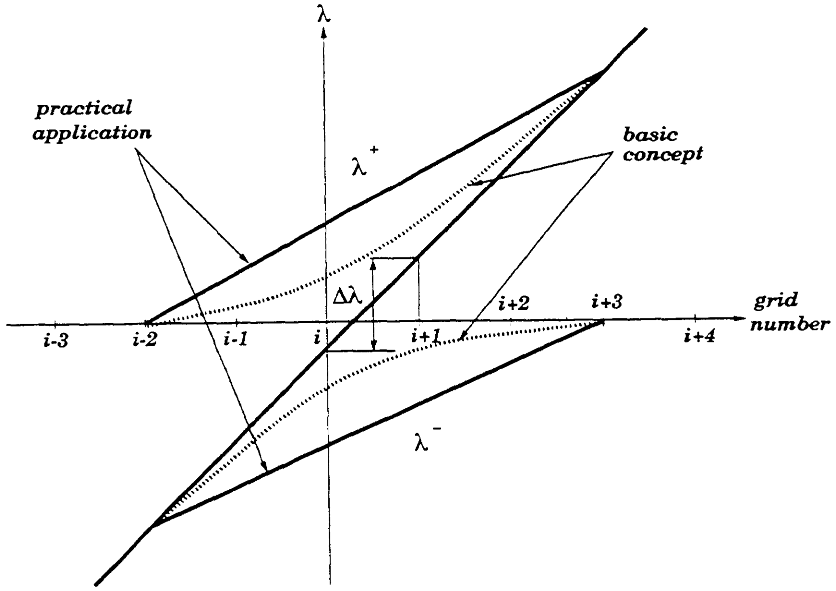

Figure 3.2: Sonic point treatment used in the code

3.3 Johnson and King's turbulence model

Since the basic equations are the Reynolds-averaged Navier-Stokes equations, turbulence viscosity terms ν_t appear in the equations. The turbulent viscosity term is used to model the Reynolds-stress term $\overline{u'v'}$ emerging from the averaging of the sub-grid scale activities in the fluid. The value of ν_t has to be determined by a certain modeling. In the current work, because a non-equilibrium transonic flow including mild separations needs to be well simulated, a one-half equation model by Johnson and King [14] with later correction by Johnson and Coakley [13] was used. The model is called a "*one-half equation*" model because the outer (wake) region uses a one-equation model and the inner sub layer uses a zero-equation equilibrium model. The non-equilibrium effect in the inner layer is imposed by matching the outer edge of the inner layer with the inner edge of the outer layer. The Johnson and King's model is known to perform best for cases with shock-boundary layer interaction [6, 24] Therefore this model was chosen for the current code in order to simulate the key phenomenon of shock-boundary layer interaction on the transonic blade's suction surface. Another attractive point of this model is that it has only three empirical constants.

In Johnson and King's model, the inner turbulent viscosity is expressed as

$$\nu_{ti} = D^2 \kappa y u_s, \tag{3.34}$$

where

$$D = 1 - \exp\left(\frac{-y^+}{A^+}\right) \quad \text{near-wall damping factor} \tag{3.35}$$

$$A^+ = 17 \quad \text{Van Driest damping constant} \tag{3.36}$$

$$y^+ = \frac{y u_\tau}{\nu} \tag{3.37}$$

$$\kappa = 0.41 \quad \text{von Karman's constant} \tag{3.38}$$

$$u_s = \sqrt{\frac{\rho_w}{\rho}} u_\tau (1 - \tanh\left(\frac{y}{L_c'}\right)) + \sqrt{\frac{\rho_m}{\rho}} u_m \tanh\left(\frac{y}{L_c'}\right) \tag{3.39}$$

$$L_c' = \frac{\sqrt{\rho_w} u_\tau}{\sqrt{\rho_w} u_\tau + \sqrt{\rho_m} u_m} L_m \tag{3.40}$$

and the outer turbulent viscosity is expressed as

$$\nu_{to}^{n+1} - \nu_{to}^{n} = \frac{\partial \nu_{to}}{\partial \nu_{tm}}(\tilde{\nu}_{tm} - \nu_{tm}^{n}) \quad \approx \frac{\tilde{\nu}_{tm} - \nu_{tm}^{n}}{1 - \exp\left(-\frac{\nu_{ti}}{\nu_{to}}\right)}. \tag{3.41}$$

The $\tilde{\nu}_{tm}$ in this equation is obtained using the PDE of the maximum Reynolds stress $\overline{u'v'}_m \equiv -1/g^2$ in the outer wake region in the boundary layer with the streamwise pressure gradient. Note that the unsteady term is included in this equation

$$\frac{\partial g}{\partial t} + u_m \frac{\partial g}{\partial s} = \frac{a_1}{2L_m}[1 - \frac{g}{g_{eq}} + \frac{C_{dif} L_m}{a_1[0.7\delta - y_m]}|1 - \sqrt{\sigma}|], \tag{3.42}$$

where

$$\begin{aligned}
L_m &\equiv (-\overline{u'v'_m})^{\frac{2}{3}}/\epsilon_m && \text{dissipation length} \\
&= \begin{cases} 0.4 y_m & \text{if} \quad y_m/\delta \leq 0.225 \\ 0.09\delta & \text{if} \quad y_m/\delta > 0.225 \end{cases} && \qquad (3.43) \\
C_{dif} &= 0.25 && \text{modeling constant} \qquad (3.44) \\
a_1 &\equiv -\overline{u'v'_m}/k_m \\
&= 0.50 && \text{modeling constant} \qquad (3.45) \\
\sigma &= \frac{\nu_{to}}{\nu_{to,eq}}. && \qquad (3.46)
\end{aligned}$$

The outer turbulent viscosity is not a self closed turbulence model. It is an iterative modification model, and the iteration starts from the converged result by a certain equilibrium turbulence model, such as Cebeci-Smith, or Baldwin-Lomax. In the current case, Cebeci-Smith model was used for the equilibrium seed to start the calculations. The Cebeci-Smith model is written as

$$\nu_{ti,eq} = \rho \kappa^2 D^2 y^2 \left|\frac{\partial u}{\partial \eta}\right| \nu_{to,eq} = 0.0168 \rho \int_0^{\delta} |u_e - u| dy, \tag{3.47}$$

where

$$A^+ = 26 \tag{3.48}$$

$$\delta = 7\frac{\int_0^\infty y\left|\frac{\partial u}{\partial y}\right| dy}{\int_0^\infty \left|\frac{\partial u}{\partial y}\right| dy}. \tag{3.49}$$

The factor 7 used in calculating the boundary layer thickness may change depending on the type of the boundary layer, so it needs to be found by trial and error.

The final turbulence viscosity to be used in the N-S equation is obtained by blending the inner and outer turbulence viscosities by the following formula

$$\nu_t = \nu_{to}\tanh\left(\frac{\nu_{ti}}{\nu_{to}}\right). \tag{3.50}$$

3.4 Turbulence transition model

In jet-engine transonic fan flow, the inflow will be laminar unless there is a distortion, and will transition to turbulent flow somewhere in the boundary layer on the blade surfaces. Hence a model for switching from the laminar flow to turbulent flow is required.

The transition model used in the current code is the e^n method [30], which has long been a popular method. The flow transitions to turbulent flow when

$$\tilde{n} > \tilde{n}_{limit}, \tag{3.51}$$

where

$$\begin{aligned} \tilde{n} &\equiv \ln\frac{A}{A_0} \\ &= \frac{d\tilde{n}}{dRe_\theta}(H)[Re_\theta - Re_{\theta 0}(H)] \qquad (3.52) \\ & \qquad (3.53) \end{aligned}$$

by approximating that H is constant, and

$$\frac{d\tilde{n}}{dRe_\theta} = 0.01\Big((2.4H - 3.7 + 2.5\tanh[1.5(H-3.1)])^2 + 0.25\Big)^{\frac{1}{2}} \tag{3.54}$$

$$\log Re_{\theta 0} = \left(\frac{1.415}{H-1} - 0.489\right) \tanh\left(\frac{20}{H-1} - 12.9\right) + \frac{3.295}{H-1} + 0.440. \quad (3.55)$$

The critical number, $\tilde{n}_{limit}$, was chosen to be a typical number, 6, but no noticeable difference in the flow field was seen by changing this number from 0 to 10. This is probably because the ξ-grid space is coarse.

3.5 Modeling the movement of the transition point

The e^n method explained in the previous section gives the turbulent transition point in a quasi-steady sense, but will not simulate movement of the transition point. One can easily imagine that the transition point will suddenly move upstream when a new transition occurs upstream of the current transition point. But one may imagine that a turbulent spot won't instantly disappear, therefore a transition point would not suddenly move downstream.

Accurate simulation of the movement of a transition point has not been studied much. But Platzer showed in his pitching helicopter blade calculations that the unsteady blade exciting force cannot be calculated if the transition point is fixed [7]. For this report, accurate modeling of the movement of the transition point is important.

The basis for modeling the downstream movement of the transition point is given by an experimental observation by Schubauer and Klebanoff [19] in 1956. They generated a turbulent spot by an electric spark, and observed how the spot evolves. Fig. 3.3 shows what they observed. The turbulent spot is shed downstream at 0.9 times the freestream velocity (U_1) at its front, and at 0.5 times U_1 at its rear end, with the spreading angle (half angle) of 11.3 degrees. From these data, the maximum velocity of the transition point moving downstream can be modeled as $0.5 \times U_e$, where U_e is the boundary layer edge velocity. In the code, if e^n method predicts larger downstream movement of the transition point than this, the new transition point is set to be $0.5U_e\Delta t$ downstream of the current transition point. For accurate simulation, the precise transition points on both suction and pressure surfaces are kept. When the transition point moves upstream, the new transition point is estimated by linear interpolation of the $\tilde{n}$'s calculated at the two grid points which bound $\tilde{n}_{limit}$.

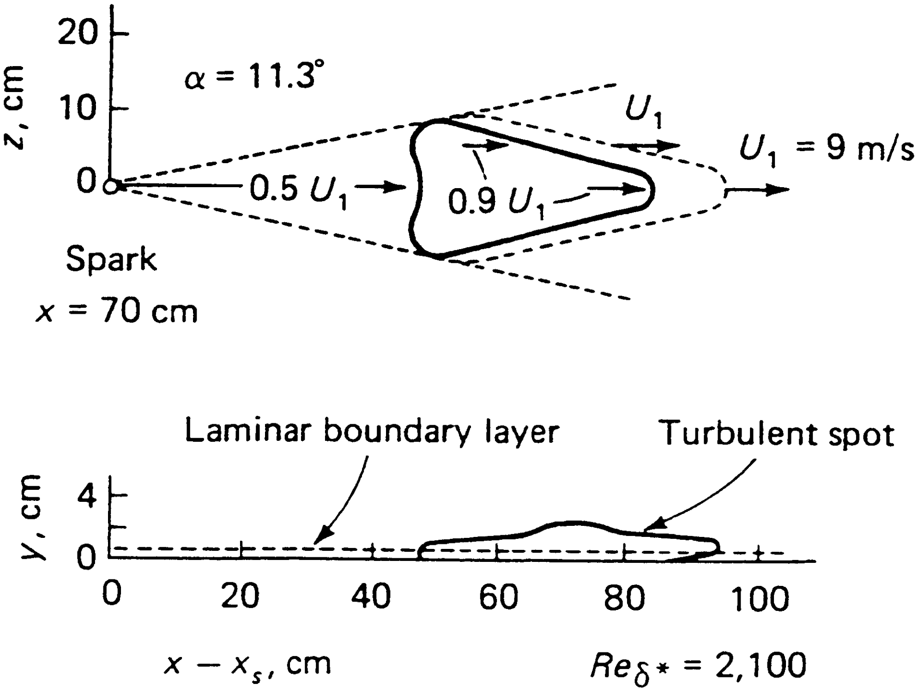

Figure 3.3: The evolution of a turbulent spot. (*from Schubauer and Klebanoff (1956)*[19])

3.6 Boundary conditions

The calculation domain has five different types of boundaries. They are inflow boundary, outflow boundary, wall boundary, wake boundary, and side boundary. The locations of these boundaries are shown in Fig. 3.4. These boundary conditions will now be discussed.

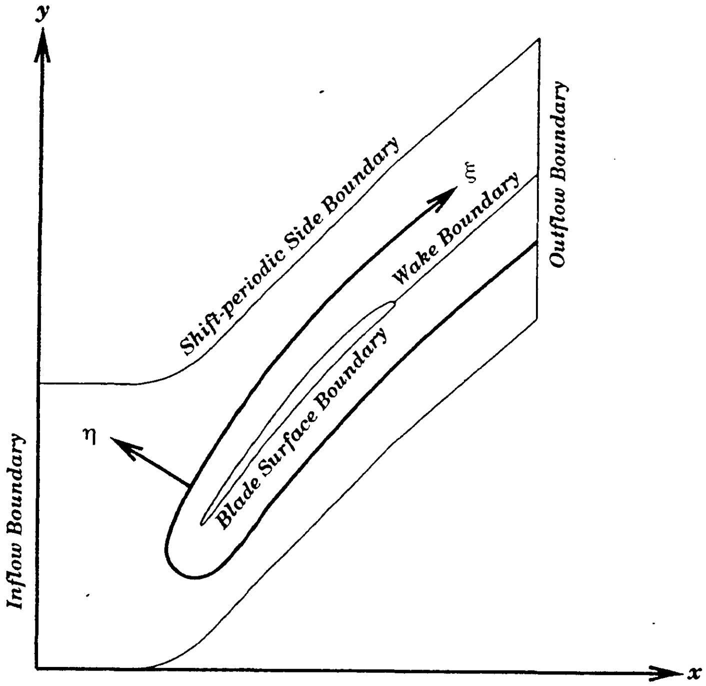

Figure 3.4: The various boundaries in the calculation domain

3.6.1 Inflow & outflow boundary

Steady calculation

At the inflow and outflow boundaries, one-dimensional characteristic boundary conditions were applied for steady calculations. "*One dimensional*" means in the direction normal to the boundary face. Four conditions were applied at the boundaries: three conditions are determined from upstream and one condition is determined from downstream. The three quantities to be conserved from upstream are

1. Entropy

$$s = \ln p - \gamma \ln \rho, \tag{3.56}$$

2. Downstream going characteristics

$$J^+ = u_s + \frac{2a}{\gamma - 1}, \tag{3.57}$$

3. Tangential velocity

$$v. \tag{3.58}$$

The quantity to be conserved from the downstream is

4. Upstream going characteristics

$$J^- = u_s - \frac{2a}{\gamma - 1}. \tag{3.59}$$

Since the inflow and outflow boundaries are selected to be aligned to the circumferential direction of the fan, the velocity normal to the cell face u_s is equal to the axial velocity u. The implementation of these conditions in the ADI scheme was done as follows:

- inflow boundary

$$\begin{pmatrix} 0 & 0 & 0 & 0 \\ 0 & 0 & 0 & 0 \\ \frac{\partial J^-}{\partial \rho} & \frac{\partial J^-}{\partial \rho u} & \frac{\partial J^-}{\partial \rho v} & \frac{\partial J^-}{\partial \rho e} \\ 0 & 0 & 0 & 0 \end{pmatrix}_{i,jmax-1}^{n} \Delta Q^n_{i,jmax-1}$$

$$- \begin{pmatrix} \frac{\partial s}{\partial \rho} & \frac{\partial s}{\partial \rho u} & \frac{\partial s}{\partial \rho v} & \frac{\partial s}{\partial \rho e} \\ \frac{\partial J^+}{\partial \rho} & \frac{\partial J^+}{\partial \rho u} & \frac{\partial J^+}{\partial \rho v} & \frac{\partial J^+}{\partial \rho e} \\ \frac{\partial J^-}{\partial \rho} & \frac{\partial J^-}{\partial \rho u} & \frac{\partial J^-}{\partial \rho v} & \frac{\partial J^-}{\partial \rho e} \\ \frac{\partial v}{\partial \rho} & \frac{\partial v}{\partial \rho u} & \frac{\partial v}{\partial \rho v} & \frac{\partial v}{\partial \rho e} \end{pmatrix}_{i,jmax}^{n} \Delta Q^n_{i,jmax} = \begin{pmatrix} s^n_{i,jmax} & - & s_{in} \\ {J^+}^n_{i,jmax} & - & {J^+}_{in} \\ {J^-}^n_{i,jmax} & - & {J^-}^n_{i,jmax-1} \\ v^n_{i,jmax} & - & v_{in} \end{pmatrix} \tag{3.60}$$

- outflow boundary

$$\begin{pmatrix} \frac{\partial s}{\partial \rho} & \frac{\partial s}{\partial \rho u} & \frac{\partial s}{\partial \rho v} & \frac{\partial s}{\partial \rho e} \\ \frac{\partial J^+}{\partial \rho} & \frac{\partial J^+}{\partial \rho u} & \frac{\partial J^+}{\partial \rho v} & \frac{\partial J^+}{\partial \rho e} \\ 0 & 0 & 0 & 0 \\ \frac{\partial v}{\partial \rho} & \frac{\partial v}{\partial \rho u} & \frac{\partial v}{\partial \rho v} & \frac{\partial v}{\partial \rho e} \end{pmatrix}_{2,j}^{n} \Delta Q^n_{2,j} - \begin{pmatrix} \frac{\partial s}{\partial \rho} & \frac{\partial s}{\partial \rho u} & \frac{\partial s}{\partial \rho v} & \frac{\partial s}{\partial \rho e} \\ \frac{\partial J^+}{\partial \rho} & \frac{\partial J^+}{\partial \rho u} & \frac{\partial J^+}{\partial \rho v} & \frac{\partial J^+}{\partial \rho e} \\ \frac{\partial J^-}{\partial \rho} & \frac{\partial J^-}{\partial \rho u} & \frac{\partial J^-}{\partial \rho v} & \frac{\partial J^-}{\partial \rho e} \\ \frac{\partial v}{\partial \rho} & \frac{\partial v}{\partial \rho u} & \frac{\partial v}{\partial \rho v} & \frac{\partial v}{\partial \rho e} \end{pmatrix}_{1,j}^{n} \Delta Q^n_{1,j}$$

$$= \begin{pmatrix} s^n_{1,j} & - & s^n_{2,j} \\ {J^+}^n_{1,j} & - & {J^+}^n_{2,j} \\ {J^-}^n_{1,j} & - & J^-_{out} \\ v^n_{1,j} & - & v^n_{2,j} \end{pmatrix} \tag{3.61}$$

and similarly for $i = imax$, where $imax$ and $jmax$ are the maximum grid number in ξ and η direction, respectively.

Unsteady calculation

The one-dimensional, unsteady, non-reflecting boundary conditions were applied for unsteady calculations. Again, "*one-dimensional*" means only in the direction normal to the boundary face. The fundamental idea of the non-reflecting boundary conditions is to specify the incoming perturbation wave from the steady solution to be null. The basic equations used in the current code were formulated by Giles [11] as follows. First, rewrite the basic 2D Euler equation in a form using ρ, u, v, and p as the primitive variables

$$\frac{\partial}{\partial t}\begin{pmatrix}\rho\\ u\\ v\\ p\end{pmatrix}+\begin{pmatrix}u & \rho & 0 & 0\\ 0 & u & 0 & \frac{1}{\rho}\\ 0 & 0 & u & 0\\ 0 & \gamma p & 0 & u\end{pmatrix}\frac{\partial}{\partial x}\begin{pmatrix}\rho\\ u\\ v\\ p\end{pmatrix}+\begin{pmatrix}v & 0 & \rho & 0\\ 0 & v & 0 & 0\\ 0 & 0 & v & \frac{1}{\rho}\\ 0 & 0 & \gamma p & v\end{pmatrix}\frac{\partial}{\partial y}\begin{pmatrix}\rho\\ u\\ v\\ p\end{pmatrix}=0. \quad (3.62)$$

Then, substitute the primitive variables with those which contain steady solution ( ), and perturbation (˜)

$$\begin{aligned}\rho &= \bar{\rho}+\tilde{\rho}\\ u &= \bar{u}+\tilde{u}\\ v &= \bar{v}+\tilde{v}\\ p &= \bar{p}+\tilde{p}\end{aligned} \quad (3.63)$$

and subtract the steady equation. The resulting perturbation equations are

$$\frac{\partial}{\partial t}\begin{pmatrix}\tilde{\rho}\\ \tilde{u}\\ \tilde{v}\\ \tilde{p}\end{pmatrix}+\begin{pmatrix}u & \rho & 0 & 0\\ 0 & u & 0 & \frac{1}{\rho}\\ 0 & 0 & u & 0\\ 0 & \gamma p & 0 & u\end{pmatrix}\frac{\partial}{\partial x}\begin{pmatrix}\tilde{\rho}\\ \tilde{u}\\ \tilde{v}\\ \tilde{p}\end{pmatrix}+\begin{pmatrix}v & 0 & \rho & 0\\ 0 & v & 0 & 0\\ 0 & 0 & v & \frac{1}{\rho}\\ 0 & 0 & \gamma p & v\end{pmatrix}\frac{\partial}{\partial y}\begin{pmatrix}\tilde{\rho}\\ \tilde{u}\\ \tilde{v}\\ \tilde{p}\end{pmatrix}=0. \quad (3.64)$$

Four perturbation waves are found by substituting solutions in wave form

$$\tilde{Q}(x,y,t)=\hat{Q}e^{i(kx+ly-\omega t)} \quad (3.65)$$

into the perturbation equations

$$\frac{\partial\tilde{Q}}{\partial t}+A\frac{\partial\tilde{Q}}{\partial x}+B\frac{\partial\tilde{Q}}{\partial y}=0. \quad (3.66)$$

Here $\hat{Q}$ is a constant vector.

Then

$$(-\omega I + kA + lB)\hat{Q} = 0. \tag{3.67}$$

The x-direction wave number k of the four waves are found as the eigenvalues of the equation

$$\det(-\omega I + kA + lB) = 0 \tag{3.68}$$

as

$$\begin{aligned} k_{1,2} &= \frac{\omega - vl}{u} \\ k_{3,4} &= \frac{(\omega - vl)(-u \pm \sqrt{a^2 - (a^2 - u^2)l^2/(\omega - vl)^2})}{a^2 - u^2}. \end{aligned} \tag{3.69}$$

After choosing the simplest eigenvectors, the four perturbation waves are found as

$$\begin{pmatrix} c_1 \\ c_2 \\ c_3 \\ c_4 \end{pmatrix} = \begin{pmatrix} -a^2 & 0 & 0 & 1 \\ 0 & 0 & \rho a & 0 \\ 0 & \rho a & 0 & 1 \\ 0 & -\rho a & 0 & 1 \end{pmatrix} \begin{pmatrix} \tilde{\rho} \\ \tilde{u} \\ \tilde{v} \\ \tilde{p} \end{pmatrix}. \tag{3.70}$$

The non-reflecting condition is obtained by specifying

- inflow boundary

$$\begin{pmatrix} c_1 \\ c_2 \\ c_3 \end{pmatrix} = 0 \tag{3.71}$$

- outflow boundary

$$c_4 = 0. \tag{3.72}$$

This is implemented in the code as follows:

- inflow boundary

$$\left(\frac{\partial c_k}{\partial Q}\Delta Q + c_k\right)_{i,jmax} = \begin{cases} 0 & for \quad k = 1,2,3 \\ \left(\frac{\partial c_k}{\partial Q}\Delta Q + c_k\right)_{i,jmax-1} & for \quad k = 4 \end{cases} \tag{3.73}$$

- outflow boundary

$$\left(\frac{\partial c_k}{\partial Q}\Delta Q + c_k\right)_{1,j} = \begin{cases} \left(\frac{\partial c_k}{\partial Q}\Delta Q + c_k\right)_{2,j} & for \quad k = 1,2,3 \\ 0 & for \quad k = 4 \end{cases} \tag{3.74}$$

and similarly for $i = imax$.

3.6.2 Side boundary

The side boundary is where the effect of inter-blade phase angle is imposed. There are two typical approaches for the side boundary conditions. One is "Shift periodic side boundary conditions" and the other is "Wrapped periodic side boundary conditions". The advantages of the former method are that arbitrary interblade phase angles can be chosen, and required memory size is smaller than the latter method. The advantage of the latter method is that the stability is larger and can handle the cases where nonlinearities such as shock waves cross the side boundary.

Shift periodic side boundary

This is done by keeping the timewise data of the state vectors on the boundary and using it in the difference equation at the side boundary with the correct amount of time shifting as did Erdos [9]. The number of grids in η direction is 2 to maintain third-order accuracy. The timewise data are kept at every nth time step, which is specified in the input file. The data are interpolated to get the value at the correct time. This procedure is used to reduce the memory requirements.

Wrapped periodic side boundary

Wrapped periodic side boundary conditions is just a multi-passage calculation, in other words. The concept is shown in Fig. 3.5. Number of the passages to calculate is given by dividing 2π by the inter-blade phase angle. Since the blade number has to be an integer, the choice of the inter-blade phase angle is limited to divisors of 2π. A disadvantage of this boundary treatment is that you need to keep the state vector values of all the grid points of all the passages. If a smaller inter-blade phase angle is requested, a larger number of blade passages is required and the calculation takes a larger memory area. The merit of this approach is the stability on the side boundaries. Because the information is exchanged across the boundary at every blade number iteration, sudden change of the state vector values across the side boundaries won't happen.

In subsonic attached flow case, shift periodic side boundary condition works fine. However, for cases with shock waves and large separations, introducing wrapped periodic side boundary conditions is essential.

3.6.3 Wake boundary

The wake boundary is the same as the side boundary, except there is no time shifting across the boundary. Therefore no furthere detail is discussed here.

3.6.4 Wall boundary

The wall boundary is assumed to be an adiabatic wall boundary in current calculations, since in fan flow the heat transfer is not large. The basic equations for wall boundary are hence

$$\begin{aligned} u &= u_{wall} \\ v &= v_{wall} \end{aligned} \tag{3.75}$$

$$\begin{aligned} \frac{\partial p}{\partial n} &= 0, \text{and} \qquad (3.76) \\ \frac{\partial H}{\partial n} &= 0 \text{or} \qquad (3.77) \\ \frac{\partial \rho}{\partial n} &= 0. \qquad (3.78) \end{aligned}$$

Numerically, these conditions were implemented as

$$\begin{pmatrix} 0 & 0 & 0 & 0 \\ 0 & 0 & 0 & 0 \\ \frac{\partial p}{\partial \rho} & \frac{\partial p}{\partial \rho u} & \frac{\partial p}{\partial \rho v} & \frac{\partial p}{\partial \rho e} \\ \frac{\partial \rho}{\partial \rho} & \frac{\partial \rho}{\partial \rho u} & \frac{\partial \rho}{\partial \rho v} & \frac{\partial \rho}{\partial \rho e} \end{pmatrix}_{i,2}^{n} \Delta Q_{i,2}^{n+1} - \begin{pmatrix} \frac{\partial u}{\partial \rho} & \frac{\partial u}{\partial \rho u} & \frac{\partial u}{\partial \rho v} & \frac{\partial u}{\partial \rho e} \\ \frac{\partial v}{\partial \rho} & \frac{\partial v}{\partial \rho u} & \frac{\partial v}{\partial \rho v} & \frac{\partial v}{\partial \rho e} \\ \frac{\partial p}{\partial \rho} & \frac{\partial p}{\partial \rho u} & \frac{\partial p}{\partial \rho v} & \frac{\partial p}{\partial \rho e} \\ \frac{\partial \rho}{\partial \rho} & \frac{\partial \rho}{\partial \rho u} & \frac{\partial \rho}{\partial \rho v} & \frac{\partial \rho}{\partial \rho e} \end{pmatrix}_{i,1}^{n} \Delta Q_{i,1}^{n+1} = \begin{pmatrix} u_{i,1}^{n} - u_{wall} \\ v_{i,1}^{n} - v_{wall} \\ p_{i,1}^{n} - p_{i,2}^{n} \\ \rho_{i,1}^{n} - \rho_{i,2}^{n} \end{pmatrix}. \qquad (3.79)$$

One thing to note on the wall boundary in the current code is that the grid cells are different from those of the usual points. This is shown in Fig. 3.6. The difference of the grid size appears in the Jacobian calculations, the calculations of the fluxes on the cell faces, and the cell face length calculations.

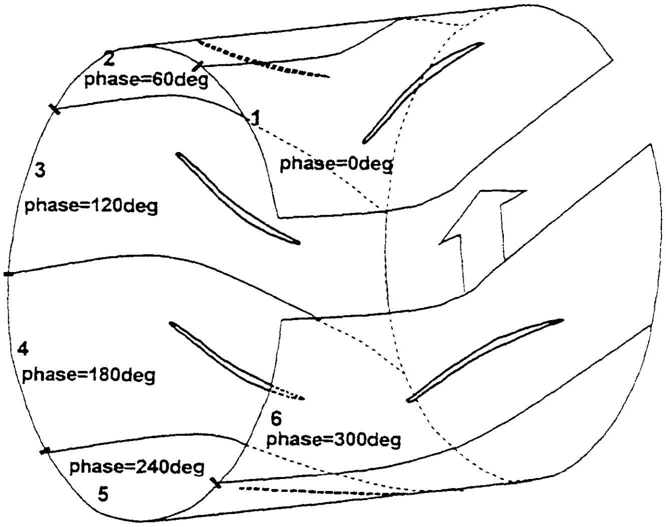

Figure 3.5: Wrapped periodic computational domain

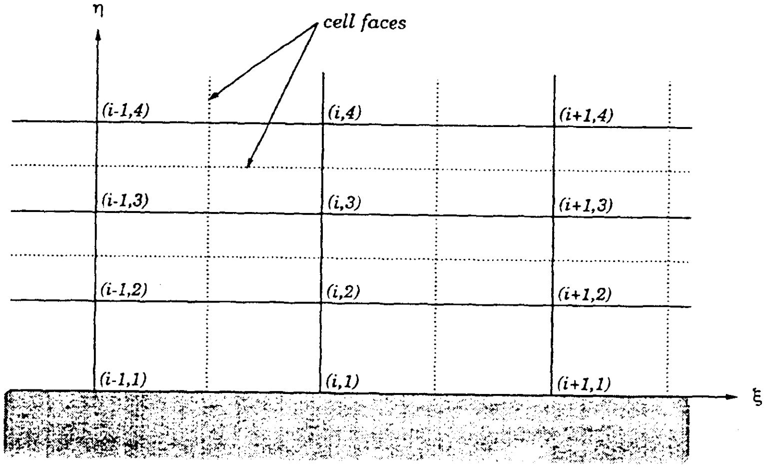

Figure 3.6: The grids at the wall boundaries

3.6.5 Trailing edge

The boundary conditions at the trailing edge are basically the same as the wall boundary conditions, but the two values at the trailing edge calculated from two different η direction ADI calculations were equated afterward by averaging. The trailing edge values are not updated in the ξ direction ADI calculations.

3.7 Moving grid

In unsteady calculations, the grids at $\eta < \eta_{max} - 2$ move as the blade moves. The corrections for the moving grid appear in two places.

In the explicit R.H.S, following terms representing the effect of the cell face motion are added in the S^* term of the discretized equations Eq.(3.2).

$$\begin{aligned}
& + \; h_{i+\frac{1}{2},j}(u_{b_{i+\frac{1}{2},j}}\Delta y'_{i+\frac{1}{2},j} - v_{b_{i+\frac{1}{2},j}}\Delta x'_{i+\frac{1}{2},j})\frac{1}{2}(Q^n_{i+1,j} - Q^n_{i,j}) \\
& + \; h_{i-\frac{1}{2},j}(u_{b_{i-\frac{1}{2},j}}\Delta y'_{i-\frac{1}{2},j} - v_{b_{i-\frac{1}{2},j}}\Delta x'_{i-\frac{1}{2},j})\frac{1}{2}(Q^n_{i,j} - Q^n_{i-1,j}) \\
& + \; h_{i,j+\frac{1}{2}}(u_{b_{i,j+\frac{1}{2}}}\Delta y'_{i,j+\frac{1}{2}} - v_{b_{i,j+\frac{1}{2}}}\Delta x'_{i,j+\frac{1}{2}})\frac{1}{2}(Q^n_{i,j+1} - Q^n_{i,j}) \\
& + \; h_{i,j-\frac{1}{2}}(u_{b_{i,j-\frac{1}{2}}}\Delta y'_{i,j-\frac{1}{2}} - v_{b_{i,j-\frac{1}{2}}}\Delta x'_{i,j-\frac{1}{2}})\frac{1}{2}(Q^n_{i,j} - Q^n_{i,j-1}),
\end{aligned} \tag{3.80}$$

where u_b and v_b are the velocity of a cell face in x and y direction, respectively.

In the L.H.S. the changes appear in the eigenvalues in the derivatives of the fluxes as shown in Eq.(3.21). For example, the grid moving speeds are subtracted from the eigenvalues as

$$\lambda_1 = \Delta s'_{i+\frac{1}{2},j}(u_n - a)_{i+\frac{1}{2},j} - (u_{b_{i+\frac{1}{2},j}}\Delta y'_{i+\frac{1}{2},j} - v_{b_{i+\frac{1}{2},j}}\Delta x'_{i+\frac{1}{2},j}). \tag{3.81}$$

Chapter 4

Grid

The quality of the calculation grid is very important in CFD. For the current calculation, the requirements for the grid can be summarized as follows.

1. The grid should have sufficient η-direction resolution in the boundary layer, while the remaining area should have far fewer grid nodes to avoid unnecessary increase in computational time.

2. The ξ-direction resolution should be sufficiently fine at the leading edge and the trailing edge, which are very sharp on a transonic compressor blade, and at the shockwave foot on the blade surface.

3. The grid should allow easy handling of arbitrary inter-blade phase angle in unsteady calculations.

4. The size of adjacent grids should not change abruptly, because the scheme assumes constant spacing for third-order flux differencing. Large grid size change can cause a numerical oscillation, and as a rule of thumb, the size change should be kept within ±20%.

5. The grid intersecting the solid surface should not be far from being perpendicular to the surface, because the scheme assumes such for the thin shear layer approximation.

4.1 Elliptic grid generator

An elliptic grid generator was used to get a nicely spaced grid. The grid control was generated by the non-uniform $\xi - \eta$ grid method [2]. The numerical scheme used to solve the elliptic partial differencial equation is the usual SOR (Successive Over Relaxation) method.

4.2 C grid

A C-type grid was chosen for current calculation because a C grid has less skew with fewer grids around the leading edge than a H-type grid. In the current calculations, the blade has a very sharp leading edge and the condition of interest is that with shockwave detached from the leading edge. So the flow around the leading edge impacts the whole flow field. An example of the grid is shown in Fig. 4.1. The inflow region of the grid is twisted to the axial direction, from the blade chordwise direction. This is a necessary treatment for stability with the elliptic grid generator. If the grid is extended straight to the chordwise direction, the grid breaks away from the lower corner of inflow boundary which has a very narrow angle. The example of this phenomenon is shown in Fig. 4.2. The rule of thumb to avoid such a phenomenon is that distances from the leading edge to the inflow boundary's upper edge and to the lower edge should be about the same.

After the SOR iteration, the grids around the corners of inflow boundary and the upper and lower side boundaries tend to be too stretched. This can be avoided by reducing the iteration number, but then the grids on the blade surface tend to be too skewed. This problem was solved by redistributing the grids near the inflow and the side boundaries after iterating enough to get a non-skewed grid on the blade surface. The redistribution was done by simple interpolation.

4.3 Neumann boundary condition on the wall

To keep the grid on the blade surface normal to the wall and have "nicely" spaced grid overall, the Neumann boundary condition was applied on the solid wall surface. Here, "nicely" means to have following qualities.

1. fine enough to represent the curve at the leading edge and the trailing edge,
2. coarse enough to save computation time and memory,
3. transfer from fine grid to coarse grid without having sudden grid size change more than 1.2 in the ratio of the grid lengths.

The grid position on the wall moves around to keep the grid normal to the wall during the SOR iteration of the elliptic grid generator. After the grid on the blade was "nicely" spaced, the surface grid positions were fixed and the elliptic generator was reiterated with the Dirichlet boundary condition on all the boundaries.

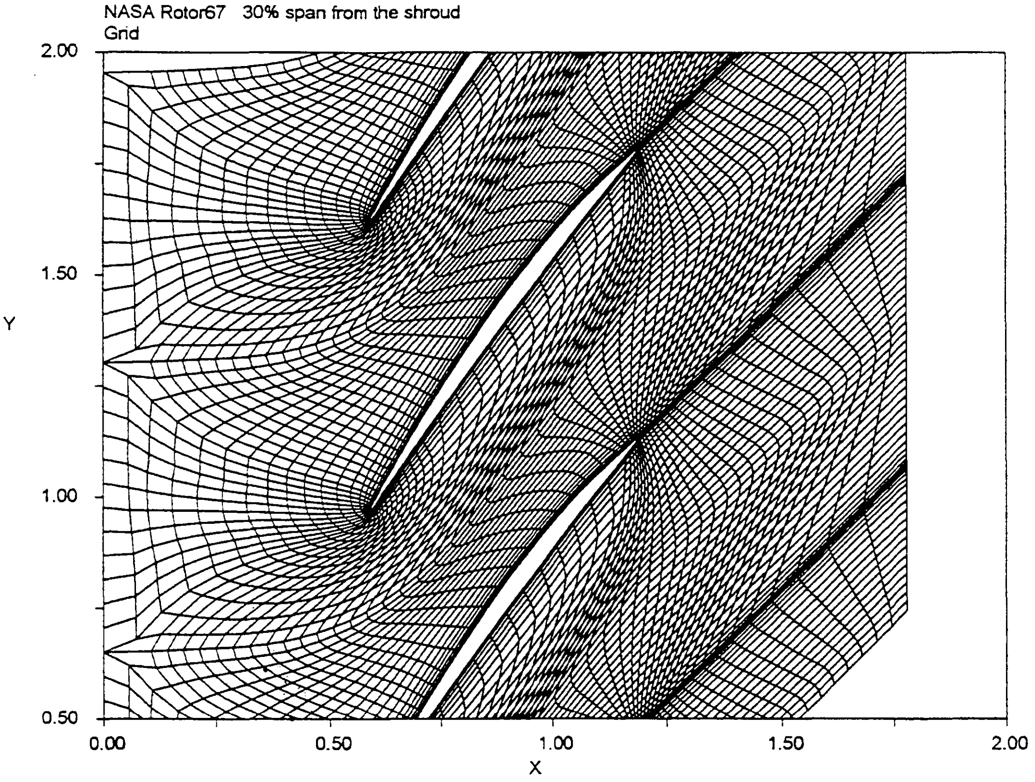

Figure 4.1: An example of the C grid around a transonic cascade

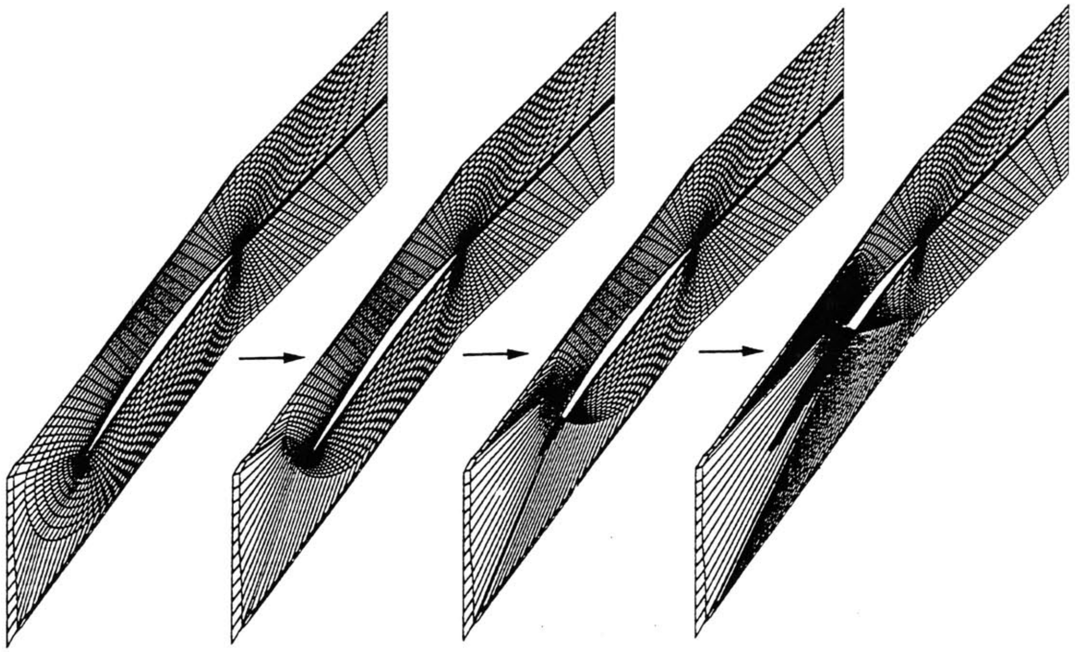

Figure 4.2: The phenomena seen in the grid with slanted inflow region

Chapter 5

Code test cases & comparisons

In this chapter, various test cases are calculated to validate the accuracy of the numerical code. The code developed is called FCASQ3. The ultimate test must be done by comparison to the experimental data, since the object of the computation in this research is to simulate the real flow. However, real data contain many complex fluid dynamic effects and it is hard to separate out each effect and accurately assess its accuracy. So the evaluation should first be done step by step by checking fluid dynamic effects, such as compressibility, viscosity, unsteadiness, turbulence model, etc, one by one. It is hard to get experimental data containing one and only one effect. However, it is the strength of the numerical calculation to have such selective data. Therefore most of the validation compared results to the numerical data produced by existing codes well proven for each fluid dynamic effect. Only one comparison with real transonic fan rig data was made at the end as a general check.

5.1 Quasi-1D unsteady compressible inviscid test case

A quasi-1D de Laval nozzle flow calculations with exit pressure oscillating was calculated, to check the code's capability to capture the unsteady shock movement crisply. Comparison was made to the calculation by Allmaras [1]. The exit pressure oscillated sinusoidally with the peak to peak amplitude 5 percent of its average value.

The result is shown in Fig. 5.1. The pressure waves are propagated upstream, passing through the throat, and reach the inflow boundary. The wave's propagation speed and the decay rate of its amplitude matched in the two calculations. The shockwave is captured very crisply within 3 grid points, which is the attractive feature of the upwinding scheme. At the inflow boundary, there is no reflection of the wave seen because non-reflecting boundary conditions were imposed.

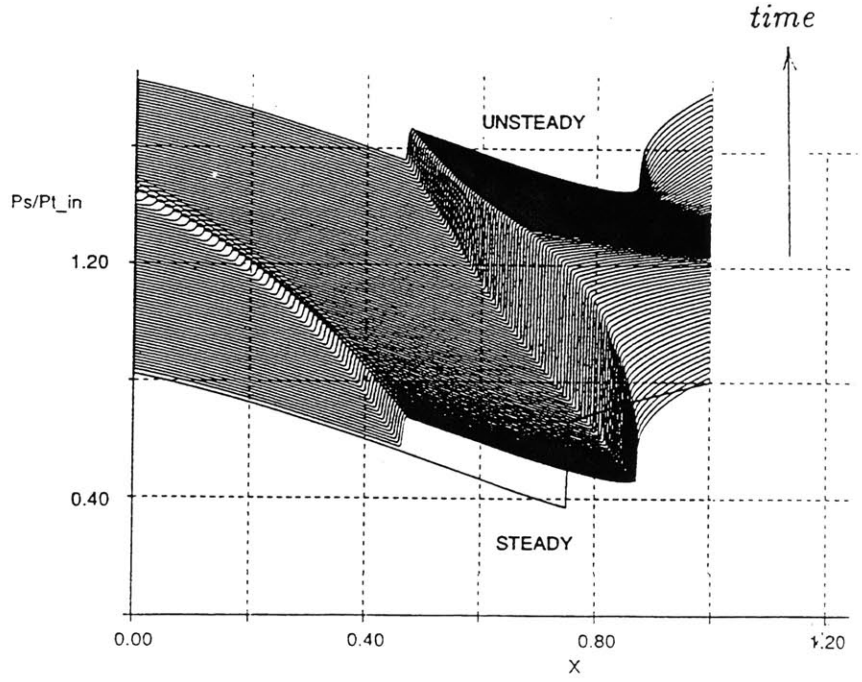

(a) current

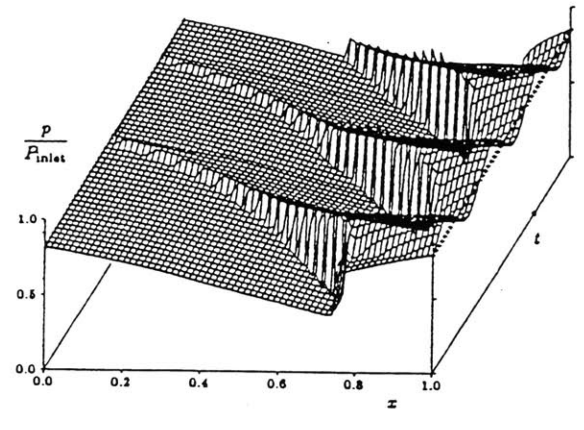

(b) Allmaras' result

Figure 5.1: Quasi-1D Laval nozzle with oscillating exit pressure

5.2 Unsteady 1-D non-reflecting boundary condition test case

1-D straight duct flow calculations with exit pressure oscillating were performed, to check the capability of unsteady non-reflecting boundary conditions to suppress the reflection at the calculation domain boundary. The result is shown in Fig 5.2. The exit pressure is oscillated sinusoidally or in saw-tooth shape with a peak-to-peak amplitude of 5 percent of the average value.

In the Laval nozzle case, Fig 5.1, the reflection from the inflow boundary was successfully suppressed, but in the straight duct with saw-tooth mode oscillation, a significant amount of the reflection remained. This is because the unsteady non-reflection boundary condition is formulated with a small perturbation assumption, which assumes that the amplitudes of the fluctuations at the boundary are more than an order smaller than the steady values. In the straight duct case, the amplitude of the pressure wave at the inflow boundary is 10 percent of the mean pressure, so the basic assumption of a small perturbation is no more valid. This shows the limit of non-reflecting boundary conditions in unsteady flow, which users should be aware of.

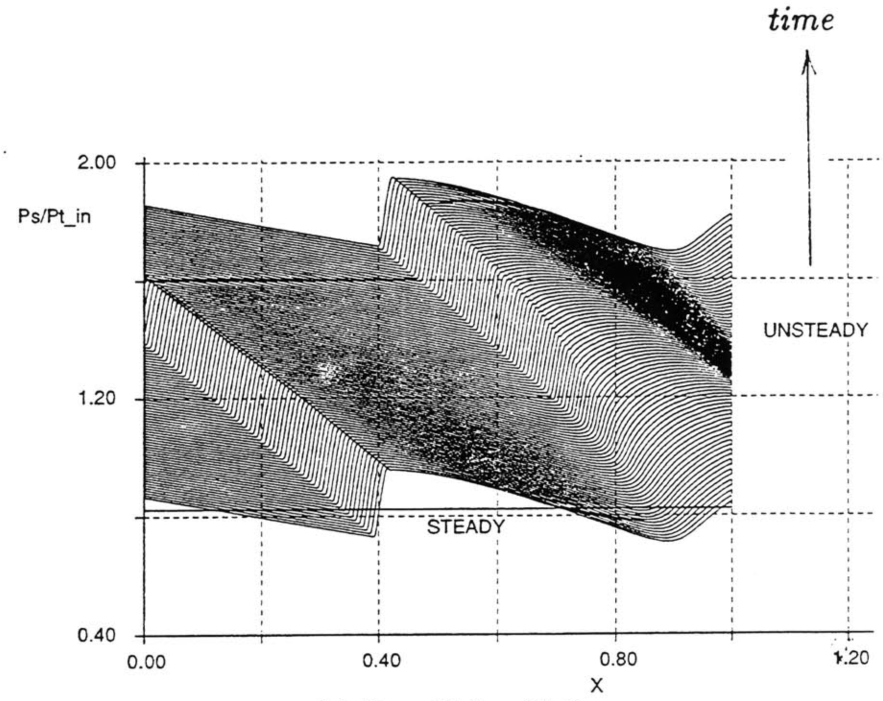

(a) Sinusoidal oscillation

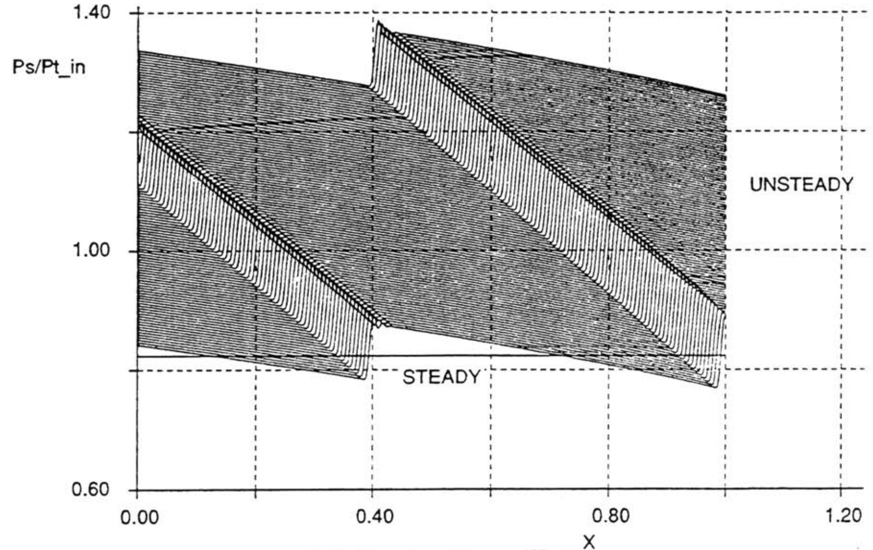

(b) Saw-tooth oscillation

Figure 5.2: Straight duct with oscillating exit pressure

5.3 Steady incompressible inviscid test cases

Steady flow around the Gostelow cascade was calculated to check the accuracy of quasi-2D steady incompressible flow calculation. This calculation shows the accuracy of the flux vector at each cell face. The calculation grid and the result is shown in Fig. 5.3. To reduce the compressibility effect in the calculation by the current code, the inflow Mach number was set to 0.05. Although there are some discrepancies around the leading edge and the trailing edge, where the flow acceleration is large and the compressibility effect takes places even with very small inflow Mach number, the result by the current code matches very well with the result by a potential flow code [12].

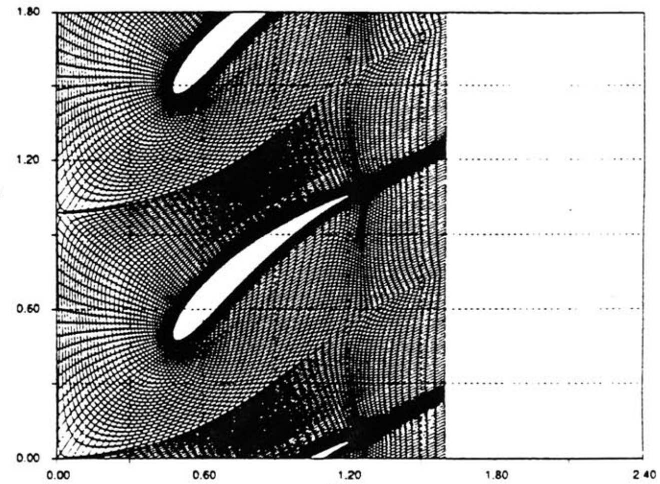

(a) calculation grid

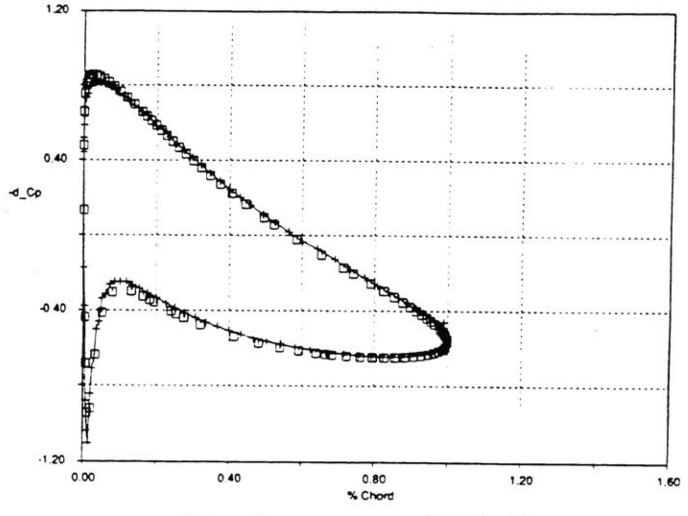

(b) surface pressure distribution

Figure 5.3: Steady incompressible flow around Gostelow cascade

5.4 Unsteady compressible inviscid test cases

Unsteady flat plate cascade flow calculations with the cascade oscillating in bending mode and in pitching mode were performed to check the code's accuracy of calculating unsteady pressure waves. The reference data was calculated by the program LINSUB. LINSUB is a linear compressible cascade flow program written by Whitehead. See [31] for details of the program. The calculation conditions are, Mach number $M_{in} = 0.2$, reduced frequency $K = 15.7$. The grid is shown in Fig. 5.4. The leading edge is contoured elliptic to avoid excessive expansion, and the trailing edge is cut off abruptly to save the grid number.

The results from the current code match very well with the LINSUB results in both bending and pitching oscillation mode with inter-blade phase angle, $\sigma = 0$ degree (Fig. 5.5 , 5.6). There is some discrepancy when $\sigma = 120$ degree. This is because the LINSUB result is not far enough from the resonance, which happens at around $\sigma = 180$ degree in the current case. Resonance is a phenomena peculiar to a linear system, and won't happen in the real cascade flow.

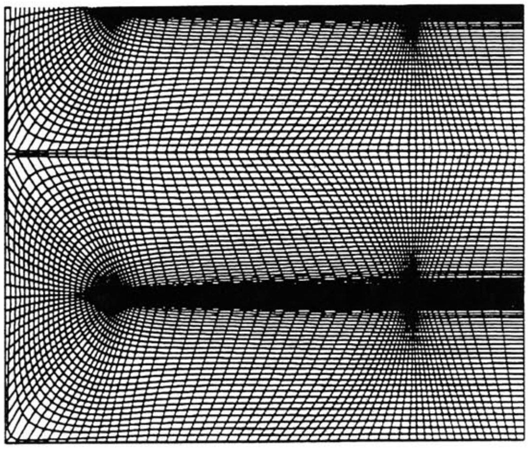

a) View of 1.5 pitch area

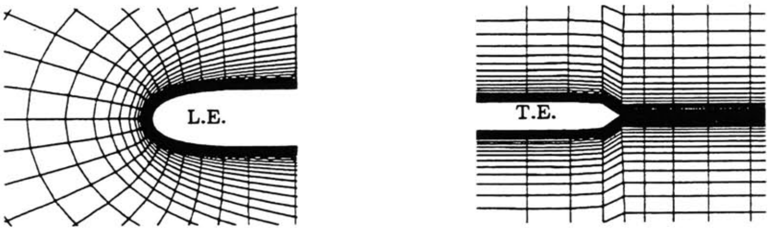

b) Grid blow up at the leading-edge c) Grid blow up at the trailing-edge

Figure 5.4: Grid for the flat plate flow calculations

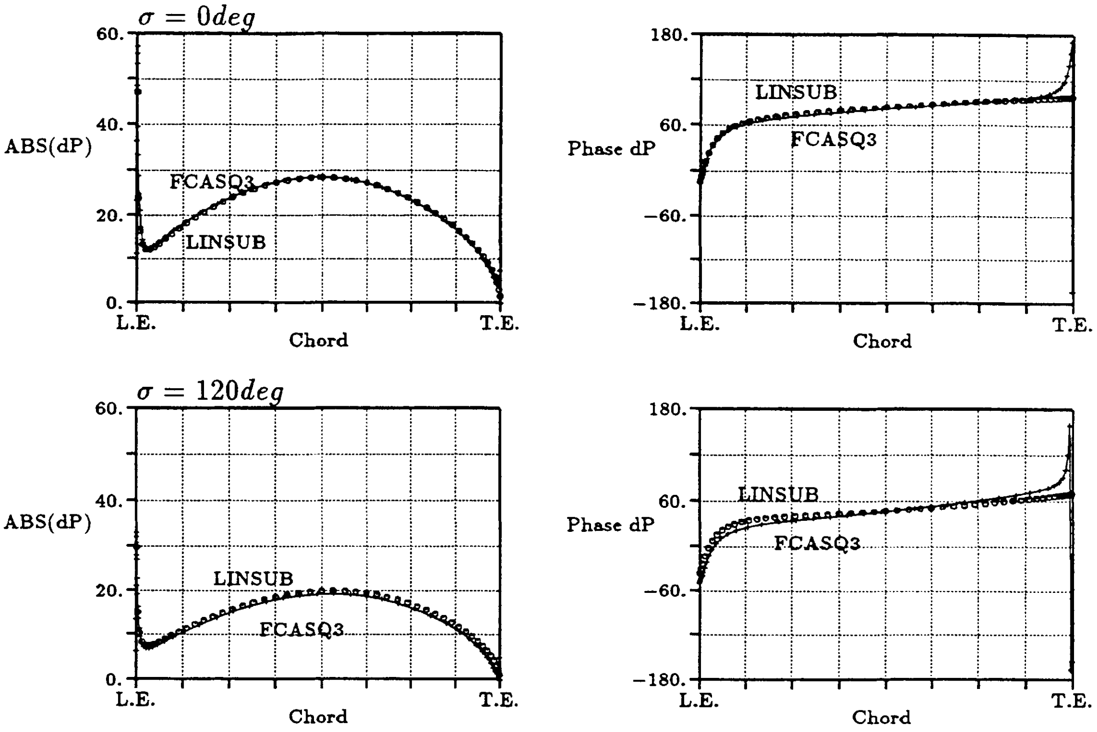

Amplitude

Phase

Figure 5.5: Unsteady surface pressure of flat plate cascade in bending oscillation

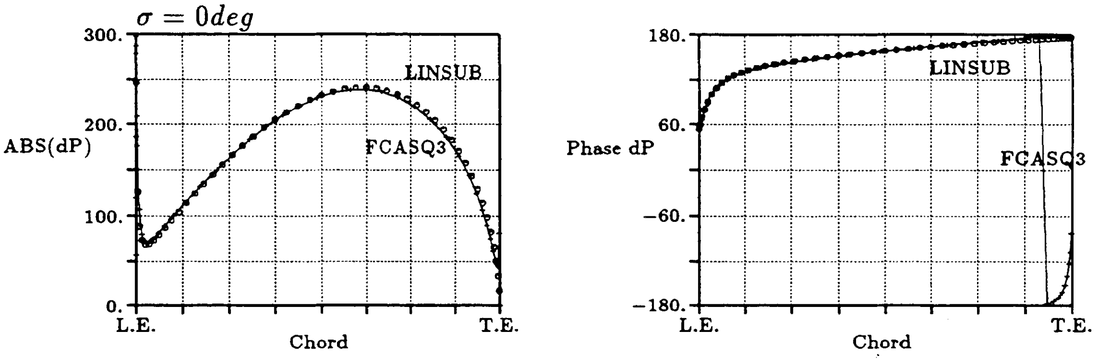

Amplitude

Phase

Figure 5.6: Unsteady surface pressure of flat plate cascade in pitching oscillation

5.5 Unsteady incompressible viscous test cases

Unsteady flat plate cascade flow calculation with the cascade oscillating in chordwise bending mode was performed to check the code's accuracy in calculating viscous effects. The analytical solution of the flow over the oscillating flat plate (known as Stokes' second problem) was used as the reference data. The basic equation of the Stokes' second problem is

$$\frac{\partial u}{\partial t} = \nu \frac{\partial^2 u}{\partial y^2}. \tag{5.1}$$

y is the direction normal to the wall surface, and the wall is oscillating in the direction normal to y. u is the velocity normal to the y direction, and ν is a kinematic viscosity. This equation contains only an unsteady term and a viscous term. The solution will indicate the velocity of the viscous effect propagation. Therefore this testcase can be a good check for the accuracy of the unsteady viscous effects in the code.

The result is shown in Fig. 5.7. The numerical calculation matches the theory very well.

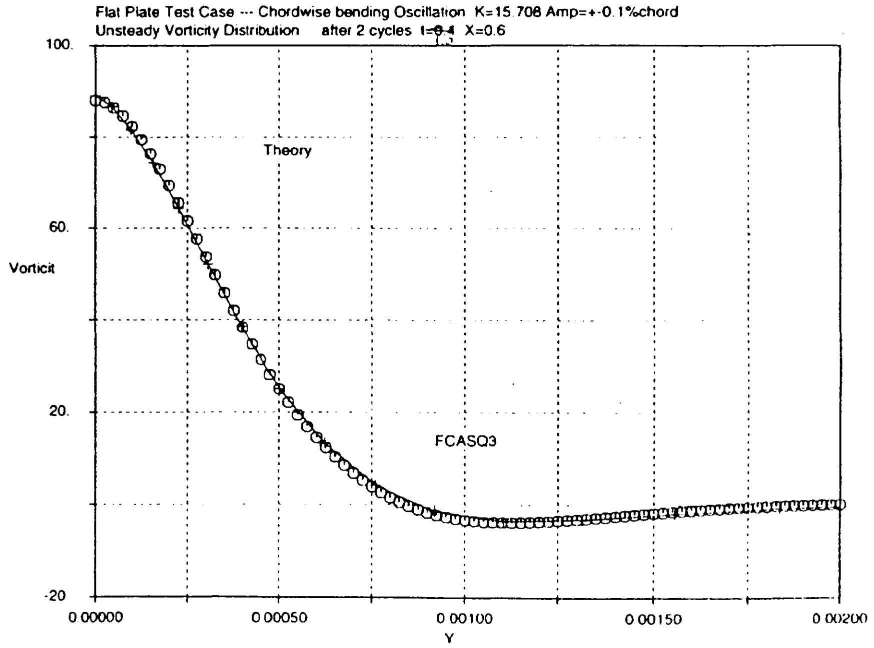

Figure 5.7: Vorticity distribution above the chordwise oscillating flat plate

5.6 Steady incompressible viscous turbulent flow test cases

Viscous flow calculations were performed under three conditions: laminar flow, turbulent flow with equilibrium turbulence model by Cebeci and Smith [4], and turbulent flow with non-equilibrium turbulence model by Johnson and King [14].

The displacement thicknesses δ, momentum thicknesses θ, and the boundary layer profiles match very well with flat-plate theory (Fig. 5.8 , 5.9). The skin friction coefficient C_f also matches very well, but the matching near the leading edge is a little bit off with equilibrium turbulence model. The non-equilibrium turbulence model by Johnson and King shows the merit over the equilibrium model by Cebeci and Smith in such a place.

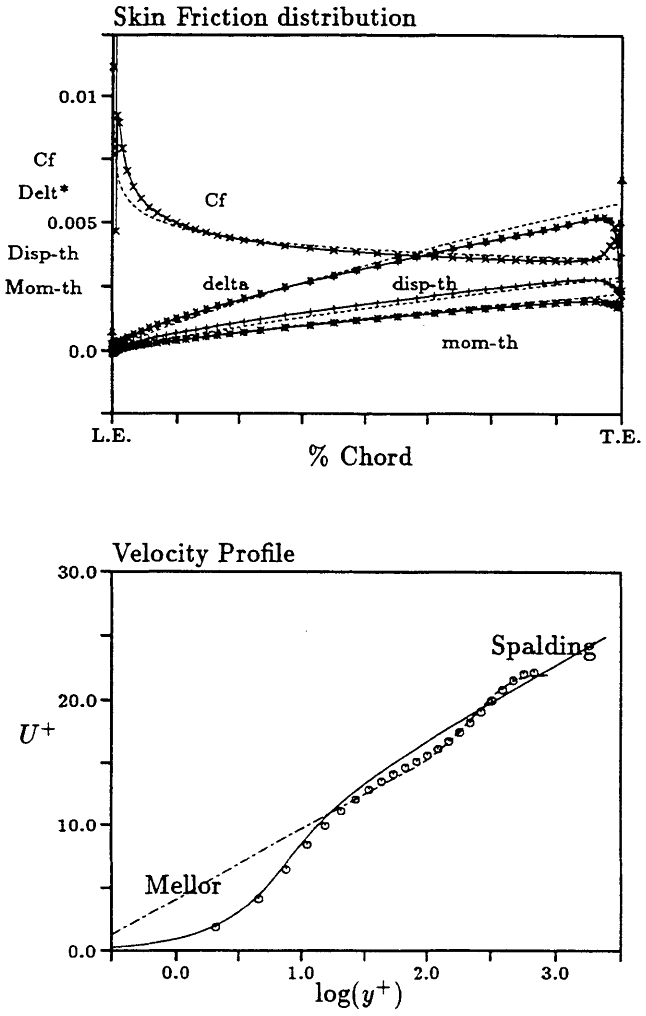

Figure 5.8: Turbulent boundary layer over a flat plate · · · Cebeci - Smith model

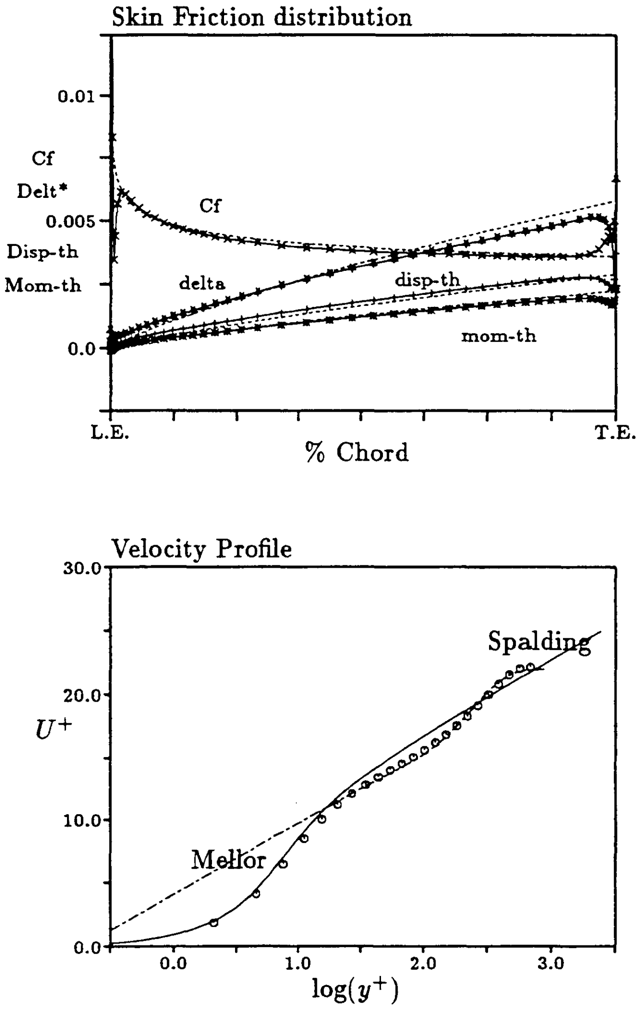

Figure 5.9: Turbulent boundary layer over a flat plate $\cdots$ Johnson - King model

5.7 Steady compressible viscous test cases

Two steady test cases were calculated to check the code's ability to calculate practical transonic compressor cascade flow. These test cases check not only the validity of the code itself, but the effect of the calculation grid. One case is a steady cascade test result, and the other is a rig test result. The cascade rig test case will show the ability to simulate a 2-D and a quasi 3-D flow, and the rig test case will show the ability to simulate the blade-to-blade flow field at a specific spanwise position in a 3-D transonic fan flow.

5.7.1 DFVLR cascade

The steady transonic cascade data were taken by H. Starken and H. A. Shereiber of DFVLR and are reported as the test case E/CA-4 in Ref. [26]. Two cases are tested and both cases are calculated here.

The specification of the linear cascade is as follows:

Blade shape	MCA	
Max. thickness	4.74	%Chord
Chord length	90	mm
Test section width	167	mm
Solidity	1.610	
Stagger angle	138.51	deg
Number of blades	6	

The test conditions are as follows:

	Test No. 53A	Test No. 115	
Inflow Mach No.	1.023	1.086	
Inflow angle	56.8	58.5	deg
Static pressure ratio	1.417	1.448	
AVDR	1.092	1.184	
Reynolds No.	1.54×10^6	1.49×10^6	
Total press. loss coeff.	0.061	0.084	,

where

$$\text{Total pressure loss coefficient} = \frac{P_{t_{in}} - P_{t_{ex}}}{P_{t_{in}} - P_{s_{in}}}$$

$$\text{AVDR} = \text{Axial Velocity Density Ratio} = \frac{(\rho u)_{ex}}{(\rho u)_{in}} .$$

Since $\rho u h$ is constant due to the mass conservation, AVDR is related to the stream-tube height by

$$\text{AVDR} = \frac{h_{in}}{h_{ex}}.$$

The resulting isentropic blade surface Mach number distributions and the Mach contours are shown in Fig. 5.10 through Fig. 5.13. The matching of the blade surface isentropic Mach number distribution is excellent except for the shock position in the test number 115. From the Mach contour, the reason for this mismatch looks to be due to the smearing of the shockwave due to the skewed grid. The shockwave is smeared while keeping its rear end at the correct position because the shock is fully detached, and the average position of the shock wave is shifted forward. It may be better to use an OH-type grid rather than a C grid in a transonic cascade flow calculation to prevent a skewed grid.

The total pressure loss coefficients were calculated as lower than the measured value. The calculated values for test No. 53A and No. 115 are 0.040 and 0.044, respectively, corresponding to 0.061 and 0.084 in the cascade test. These are even lower than the calculated results by H. Youngren using the program MISES (Ref. [33]), which are 0.0454 and 0.0588. One explanation of these mismatch is due to the modeling of the sidewall boundary layer by simple passage contraction model, as Youngren pointed out. The mismatch of current calculations from Youngren's results may be due to the coarse grid at the exit flow region. The mixing loss in the exit flow region is not simulated well in current calculations.

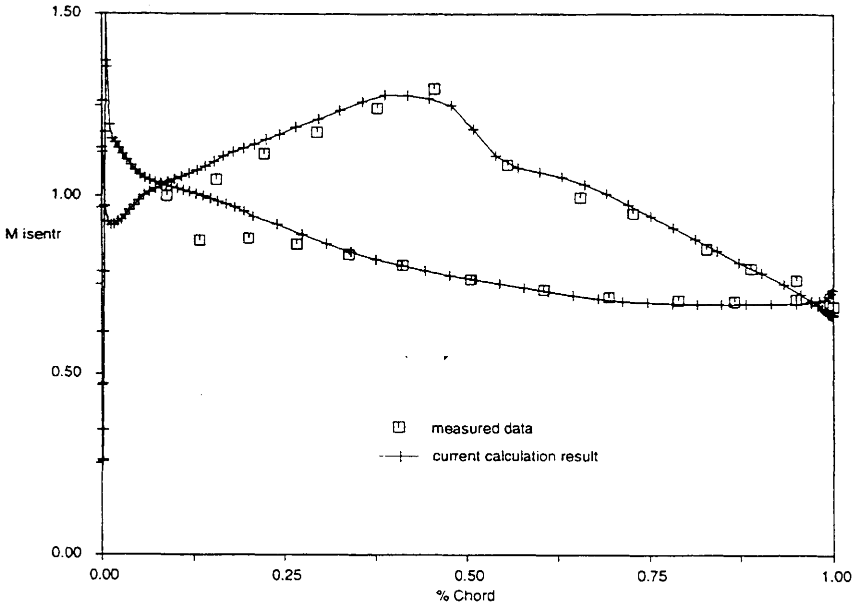

Figure 5.10: Blade surface isentropic Mach number distribution .. Test No. 53A

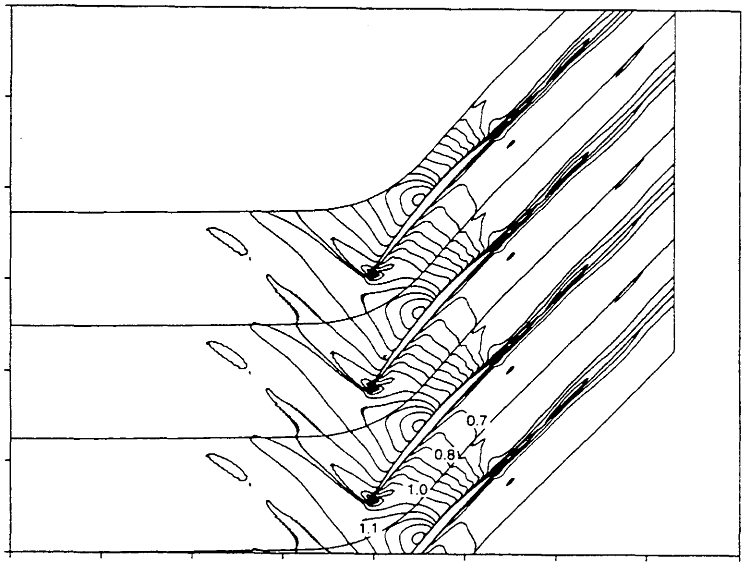

Figure 5.11: Mach contour of DFVLR cascade calculation .... Test No. 53A

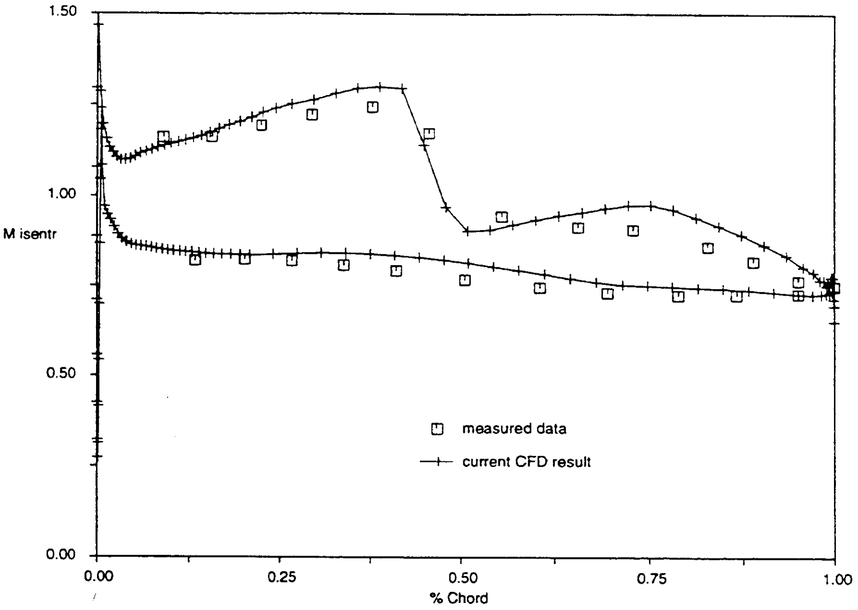

Figure 5.12: Blade surface isentropic Mach number distribution ... Test No. 115

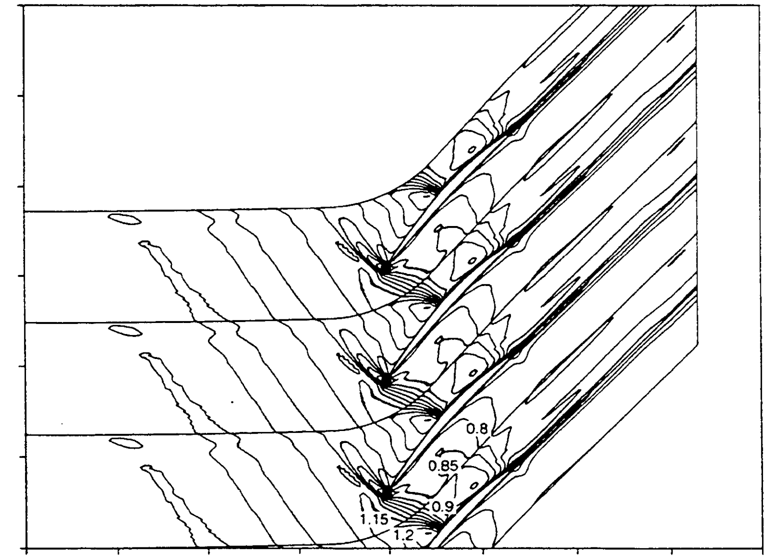

Figure 5.13: Mach contour of DFVLR cascade calculation .... Test No. 115

5.7.2 NASA Rotor 67

Steady simulation calculation of NASA rotor 67 blade to blade flow was performed to check the quasi-3D code's applicability to simulate three dimensional transonic fan flow. This research transonic fan has 22 rotor blades with the inlet diameter of 51.4cm and the inlet hub/tip ratio of 0.375. At the design point, the mass flow rate is 33.25 kg/sec, the pressure ratio is 1.63, tip relative Mach number is 1.38, and the fan speed is 16043 rpm. The rotor blades are snubberless wide chord blades, and the aspect ratio is 1.56 based on the average span and root axial chord. The reference data were taken from NASA's laser anemometer measurement data by Strazisar et al [27]. The axial and tangential velocities were measured at 50 points in tangential direction, 30 points in axial direction at approximately every 10 percent span. The data at each data point are the average of those of 17 different passages, and data at a point in a passage are the average of 10 to 70 measurements.

The calculations were done for the blade-to-blade flow at the "30% from the shroud" radial position of "near stall" and "peak efficiency" conditions. The input data used for the calculations are tabulated in Table 5.1.

The calculations never came to a steady state. The instantaneous Mach contour in Fig. 5.15 shows vortex shedding and resulting shock oscillation. The frequency of the vortex shedding is 10 to 22 kHz. This matches to the vortex shedding frequency of a transonic fan shown by Epstein et al [8].

The averaged Mach contours shown in Fig. 5.14-a and Fig. 5.17 match well to the NASA laser measurement data, except at the pressure surface just downstream of the leading edge of the "near stall" case. The laser data shows a thin region accelerating to supersonic, which is not seen in the averaged CFD result, but in instantaneous Mach contours in Fig. 5.15. The unsteady calculations revealed that the acceleration region on the pressure surface is due to periodic separation by shock oscillation. Timewise blade surface pressure distribution in Fig. 5.15 shows that the separation on the pressure surface appears when the shock wave is in rear position, and disappears when the shock is detached.

The position and the shape of the shock foot of the calculation match very well with the laser data in both "near stall" (Fig. 5.14) and "peak efficiency" (Fig. 5.17) cases. This implies that the separation behind the shock foot due to the shock-boundary layer interaction is simulated well. Accurate simulation of the shock-boundary layer interaction is an important feature for an accurate transonic flutter simulation calculation. Hence, by matching Mach contour very well with the measurement, the code has been verified as a plausible tool for the flutter mechanism study.

Table 5.1: Input data for NASA rotor 67 steady flow calculations

	near stall	peak efficiency	
Inflow relative Mach number	1.185	1.248	
Inflow relative velocity	393.3	409.6	[m/s]
Inflow angle	64.9	61.8	[deg]
Static pressure ratio	1.576	1.654	
Blade chord length	8.917	8.917	[cm]
Kinematic viscosity	1.779	1.847	$\times 10^{-5}$ [m^2/sec]
Reynolds number	1.971×10^6	1.978×10^6	

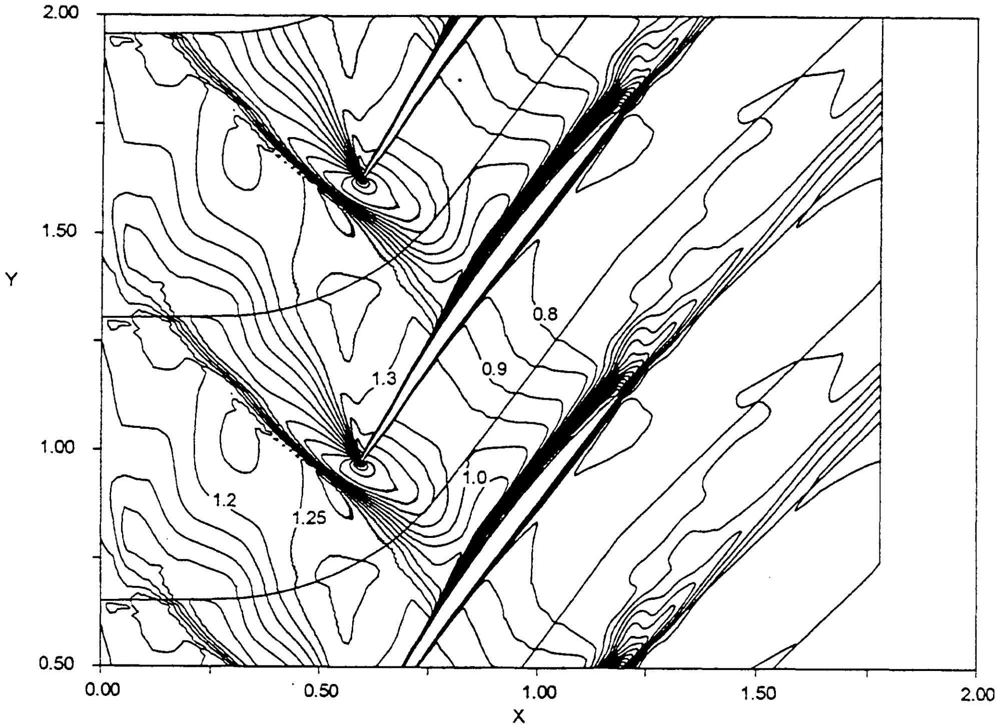

(a) current calculation (averaged data)

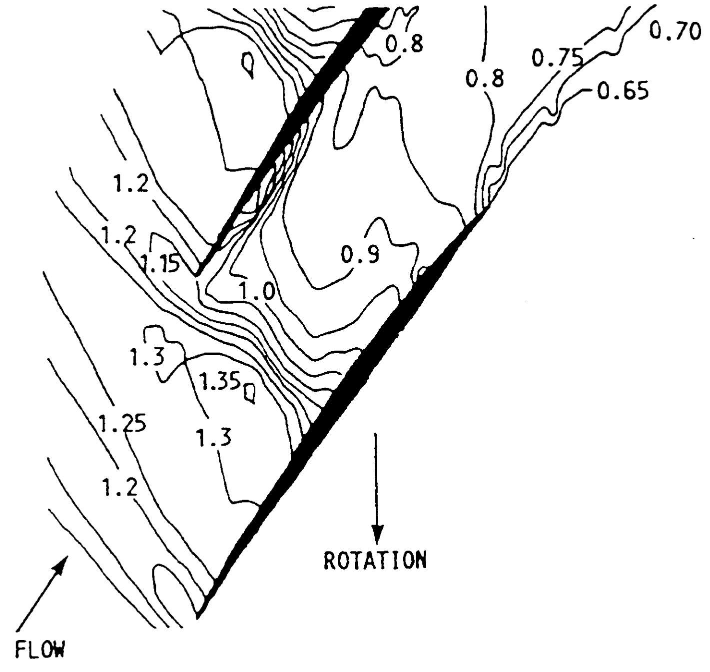

(b) NASA laser measurement (*from Strazisar [27]*)

Figure 5.14: NASA rotor 67 steady flow calculation .... "Near stall"

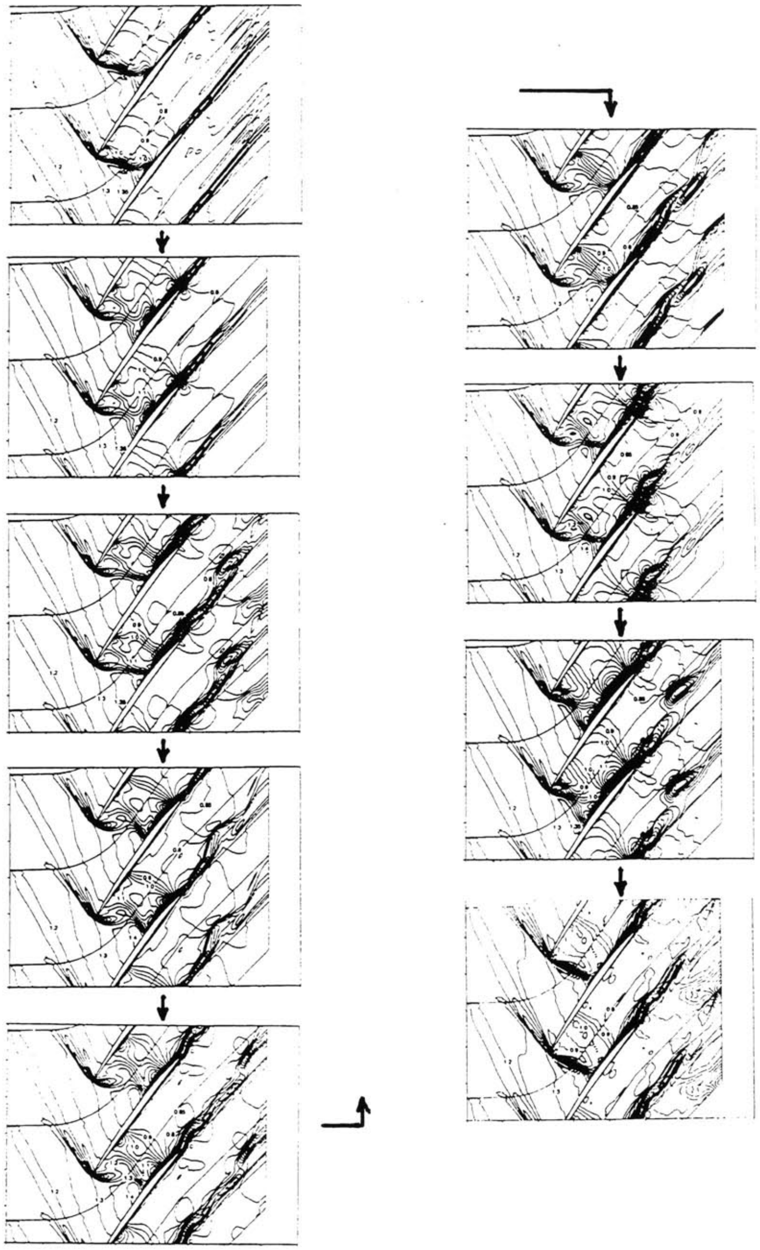

Figure 5.15: NASA rotor 67 steady flow calculation .... "Near stall"

Instantaneous Mach contours (plotted every 6×10^{-5} second)

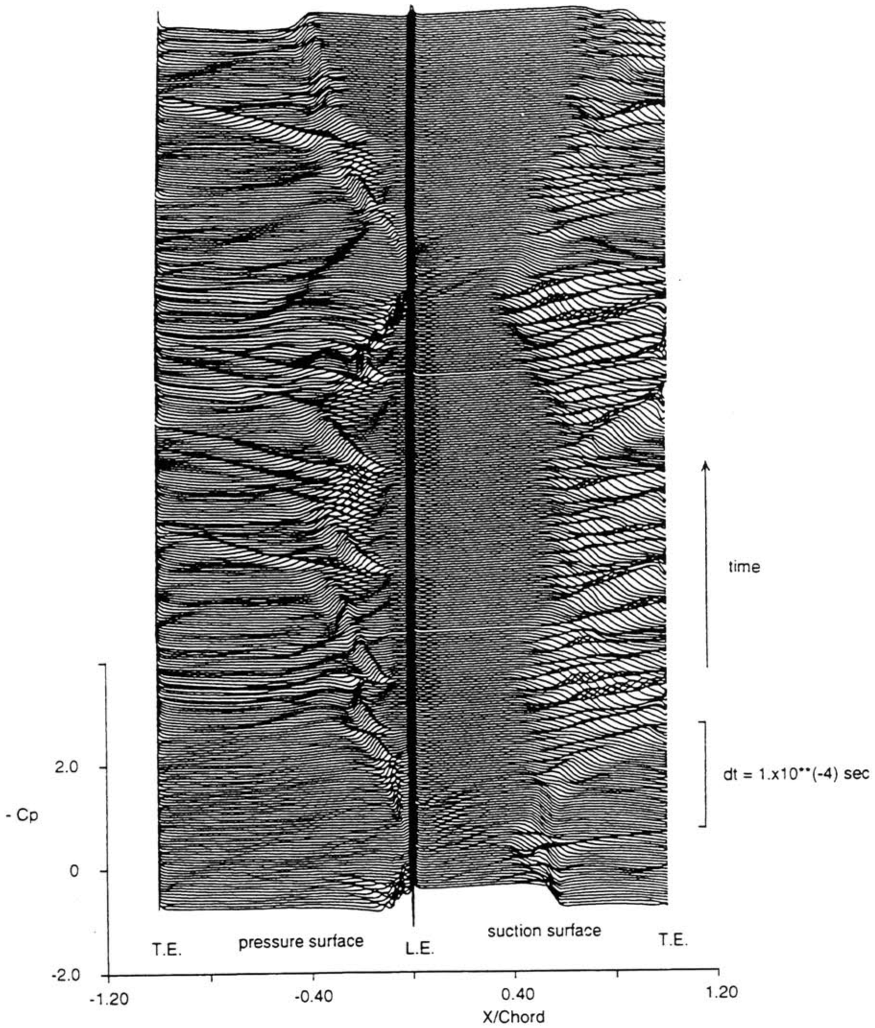

Figure 5.16: NASA rotor 67 steady flow calculation .... "Near stall"

Timewise blade surface pressure distribution

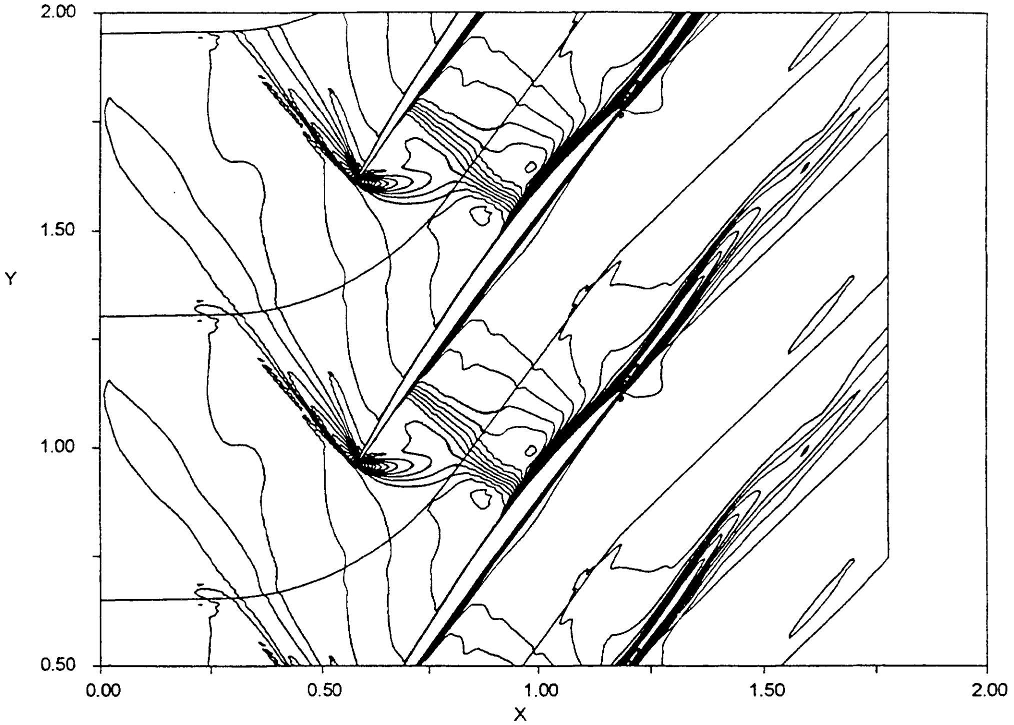

(a) current calculation (averaged data)

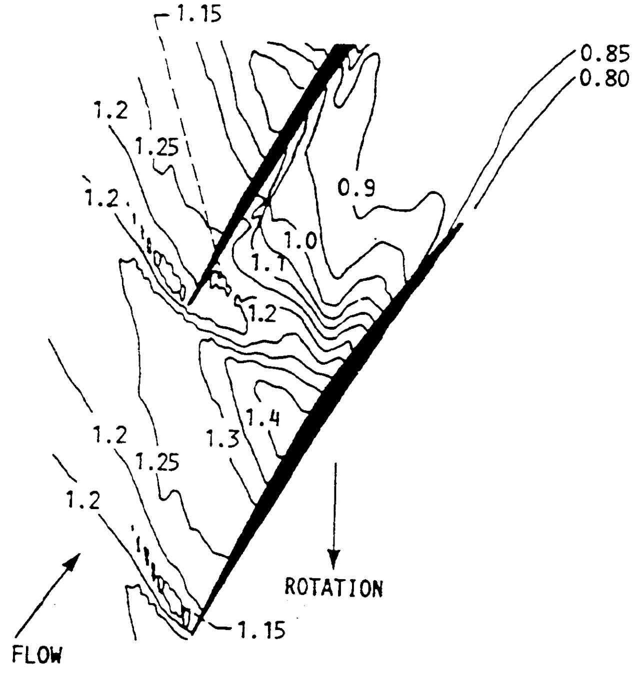

(b) NASA laser measurement (*from Strazisar [27]*)

Figure 5.17: NASA rotor 67 steady flow calculation ... "Peak efficiency"

5.8 Unsteady compressible viscous test cases

Calculations of oscillating transonic compressor cascade were performed to verify the ability of the code to simulate transonic flow in flutter. The test data used is the configuration No.7 in the standard configuration data set compiled by A. Bölcs and T. H. Fransson (Ref. [3]). The original data were taken in the Detroit Diesel Allison rectilinear air test facility under the sponsorship of NASA Lewis research center (Ref. [17]). The specifications of the test facility and the test cascade are listed below:

Number of blades	5	
Blade oscillation mode	Torsion	
Oscillating frequency	710 ~ 730	Hz
Axis of the torsional oscillation	50	% chord
Test section width	76.2	mm
Blade profile	MCA	
Chord length	76.2	mm
Max. thickness	3.4	% chord
Solidity	1.170	
Stagger angle	51.55	deg .

The test data set contains 12 different test cases. Most of the cases have rather large scatter in blade-to-blade uniformity of their oscillation amplitude and of the inter-blade phase angle. This is due to the high blade oscillation frequency (725Hz), and the considerable complications involved in measuring unsteady transonic flow in cascades. However, it should be noted that the quality of the data is representative for the state-of-the-art of aeroelastic experiments on compressors in transonic flow regime.

The case with the best blade-to-blade uniformity is selected for the calculation. The conditions of the case selected for the calculations are listed below:

Inflow Mach number	1.315	
Inflow angle	64.0	deg
Outflow Mach number	0.99	
Reduced frequency	0.44	
Amplitude of the oscillation	±0.1157	deg
Inter-blade phase angle	0.0	deg .

The scatter of the blade oscillation amplitudes and the inter-blade phase angles of the cascade test data are as follows.

	$\frac{\alpha^{-2}}{\alpha^{0}}$	$\frac{\alpha^{-1}}{\alpha^{0}}$	$\frac{\alpha^{+1}}{\alpha^{0}}$	$\frac{\alpha^{+2}}{\alpha^{0}}$
Amplitude of the oscillation	0.64	0.96	1.11	0.0

	$\sigma^{-2\rightarrow-1}$	$\sigma^{-1\rightarrow0}$	$\sigma^{0\rightarrow+1}$	$\sigma^{+1\rightarrow+2}$	
Inter-blade phase angle	-4	+8	-5	0	(deg)

The calculations were done by assuming uniform blade oscillation amplitude of 0.1157 degree and uniform inter-blade phase angle of 0.0 degree.

First, the steady state calculation was performed. The resulting blade surface pressure distribution is shown in Fig. 5.18. The calculation was performed by adjusting the passage contraction to let the calculation result match to the measured data, since the blockage effect data by the sidewall boundary layer are not supplied and the code already showed excellent match to the data in steady calculation when the passage contraction data were given. Also note that the passage contraction value used to match the steady results was similar to the value used in the DFVLR cascade cases.

Next, the unsteady calculation was performed for the case of interblade phase angle at 0 degrees. The resulting amplitude distribution and phase distribution of the blade surface aerodynamic pressure are shown in Fig. 5.19 and Fig. 5.20. Considering the scatter of the data, the matching of the calculated results to the cascade data is good. Although a discrepancy was seen in the phase behind the shock foot on the suction surface, the amplitude and the phase of the blade surface unsteady pressure upstream of the shock foot and on the pressure surface show a good match. The chordwise amplitude of the shock oscillation also shows a good match. Hence the code is validated as a plausible tool to simulate 2D unsteady transonic flow.

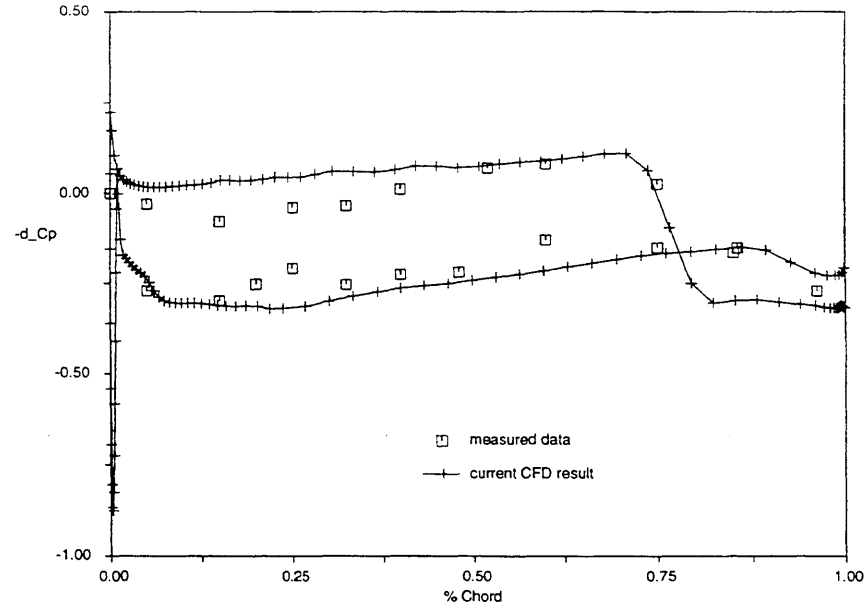

Figure 5.18: Blade surface pressure distribution of steady state condition of standard configuration # 7

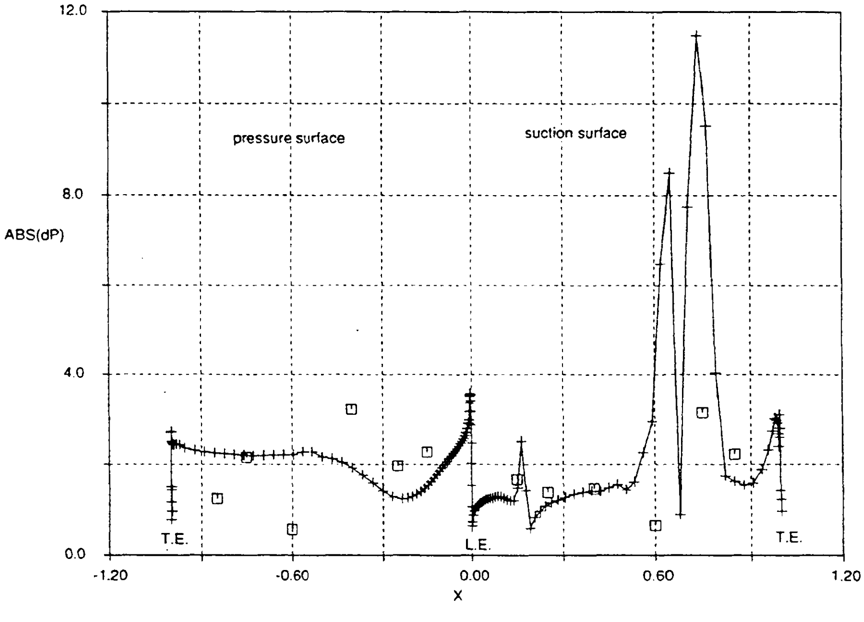

Figure 5.19: Blade surface amplitude distribution of the unsteady pressure. Standard configuration #7, $\sigma = 0$ deg.

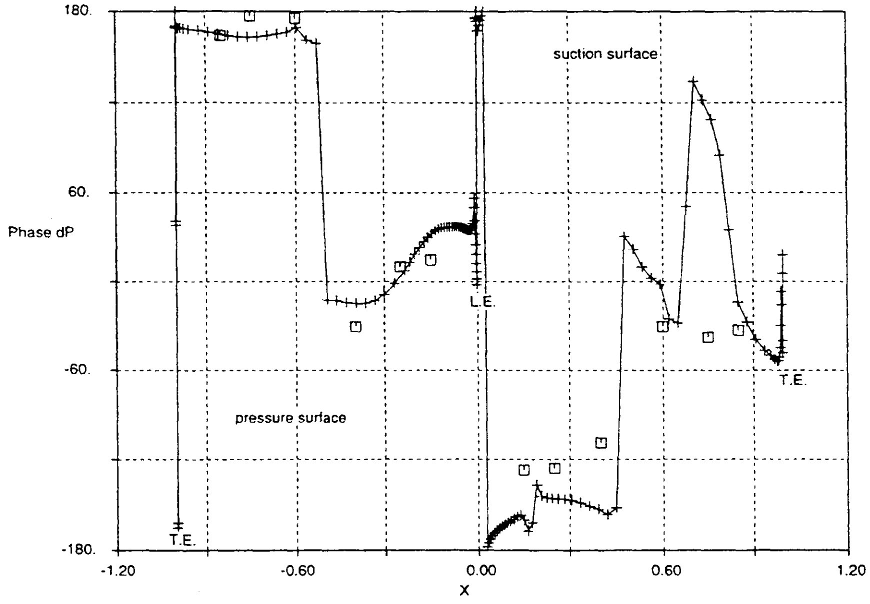

Figure 5.20: Blade surface phase distribution of the unsteady pressure. Standard configuration # 7, $\sigma = 0$ deg.

5.9 The importance of the turbulence model

In the NASA rotor 67 "near flutter" test case, calculations with two different turbulence models and a calculation with laminar flow were performed to check the importance of the turbulence model in the transonic blade to blade calculations. The calculation conditions are shown in Table 5.1 of the previous section. The timewise blade surface pressure distributions are shown in Fig. 5.21, and the snapshots of the blade to blade Mach contours are shown in Fig. 5.22.

The differences are significant. The laminar case shows a totally different boundary layer separation position. This indicates that turbulent transition keeps the flow attached on the suction surface behind the leading edge and thus turbulent calculation is essential for the transonic blade to blade calculations.

Turbulent calculation with the Cebeci-Smith model shows a long separation region behind the shock wave. The separation region is so long that the first half of the separation region will not be changed by the vortex shedding at the end of the separation region, and therefore the shock wave position does not move. This will cause totally different aerodynamic blade exciting force from the result of the Johnson-King model. It is really important to use a turbulence model which can correctly simulate the separation due to the shock-boundary layer interaction. The Johnson-King model was developed to handle shock-boundary layer interactions, and is known for its ability to simulate them well in steady 2D transonic flow. Although its ability in unsteady calculations is not well known, this model would be the best model we currently have available for these cases.

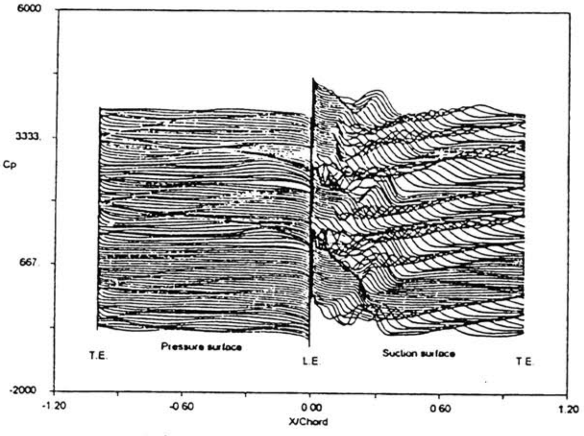

(a) Johnson-King model

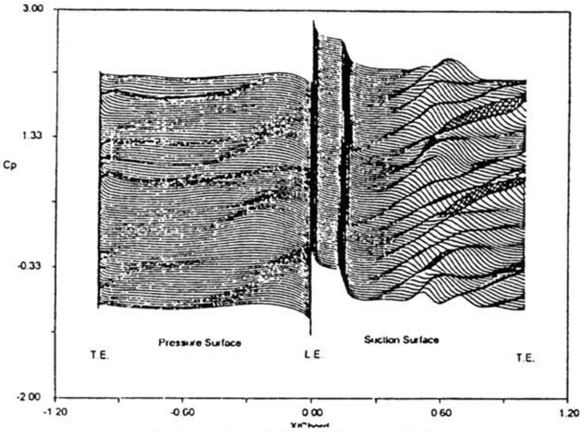

(b) Cebeci-Smith model

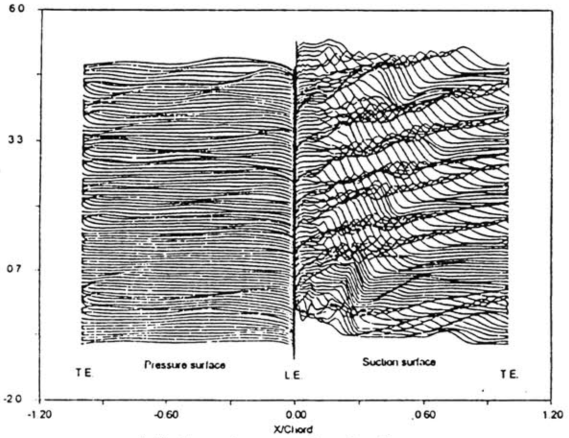

(c) Laminar calculation

Figure 5.21: The effect of different turbulence models

Timewise blade surface pressure distributions

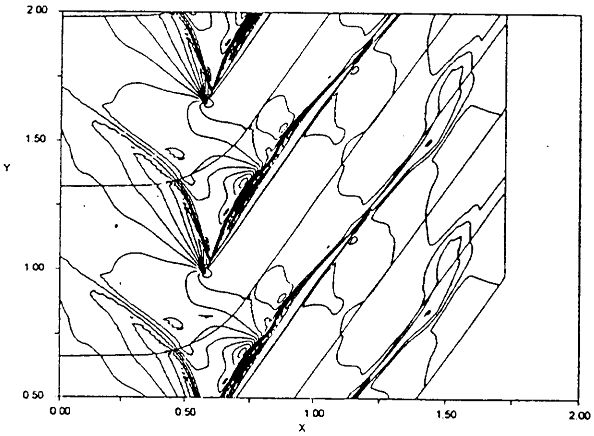

(a) Johnson-King model

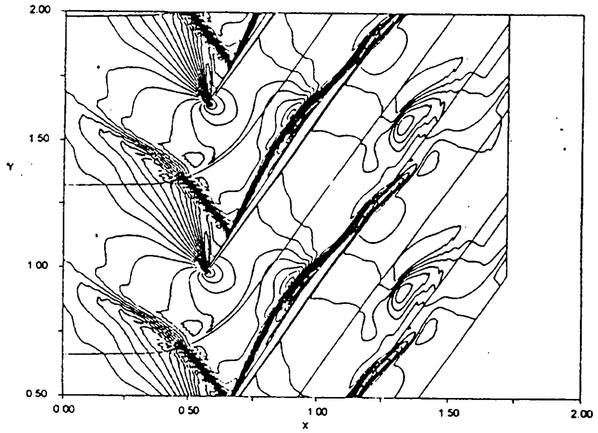

(b) Cebeci-Smith model

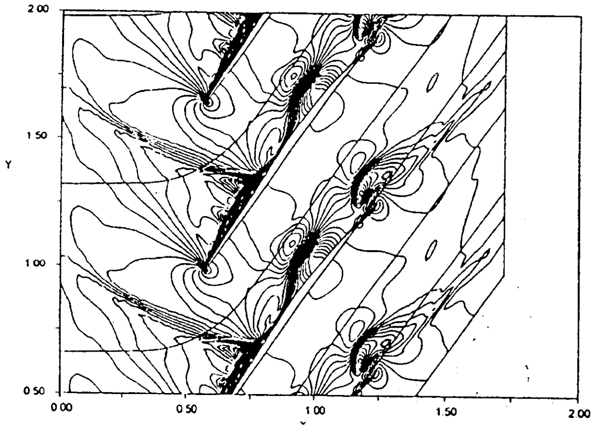

(c) Laminar calculation

Figure 5.22: The effect of different turbulence models

Instantaneous Mach contours

5.10 The importance of the transition point model

Motion of the transition point is modeled in the code using the experimental results reported by Schubauer and Klebanoff [19] as was previously explained in Section 3.5. Since Platzer reported [7] that the unsteady blade exciting aerodynamic force didn't emerge in the calculation with fixed transition point, it is worth checking the effect of the current transition point motion model on the blade exciting aerodynamic force in unsteady transonic cascade flow calculations.

Three cases of unsteady calculations with (1) current transition point motion model, (2) current model without downstream motion limiter, and (3) a fixed transition point, are compared to see the effect of the moving transition point model. A set of input data near flutter condition is taken from IHI research fan rig test. Details of the IHI research fan are described in Chapter.6.

The blade total unsteady aerodynamic forces are compared in Table 5.2. A difference is seen in the phase angle.

Table 5.2: The effect of moving transition point

	Current model	e^n only	Fixed transition point	
Amplitude	0.695	0.740	0.678	
Phase	-111.7	-125.7	-118.1	[deg]
Blade exciting energy	-0.646	-0.601	-0.598	

The motion of the transition point during a cycle of the blade oscillation of these cases are shown in Fig. 5.23. Triangular plots in the figures are the transition points. For the current model, periodic downstream-shedding of the transition points is seen, whereas for the case with only the e^n method, a larger scatter of transition points is seen and the transition points are located further downstream than the other cases. The average location of transition points differs greatly from the most upstream location calculated. In unsteady calculations, the e^n method does not give a stable transition location, and therefore it is important to have a model for the downstream shedding of transition points to simulate the unsteady behavior of the transition point better, even if the model is not perfect.

Although the difference in the calculated results tabulated in Table. 5.2 does not seem large, the difference in the blade surface energy distribution is large (Fig. 5.24). Not only the location of the shock waves, but also the location of the blade exciting energy are different. Therefore the downstream shedding model should be used with the e^n method in unsteady calculations. The limiter of the downstream motion of transition points played an important role in unsteady calculations.

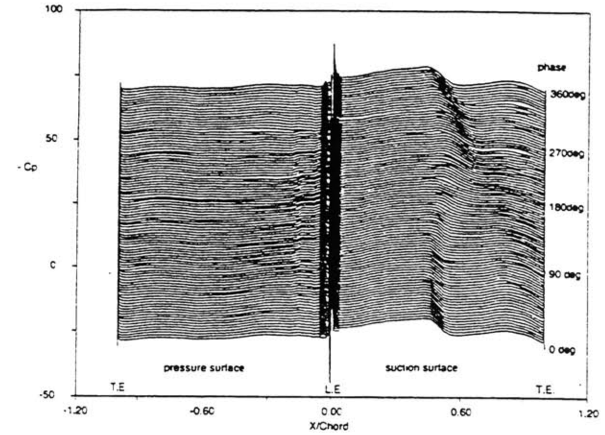

(a) Fixed transition point

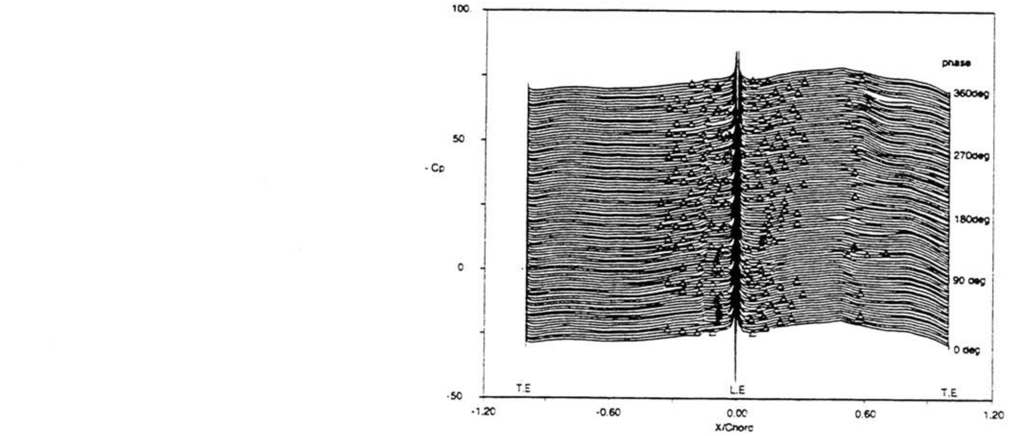

(b) Current model

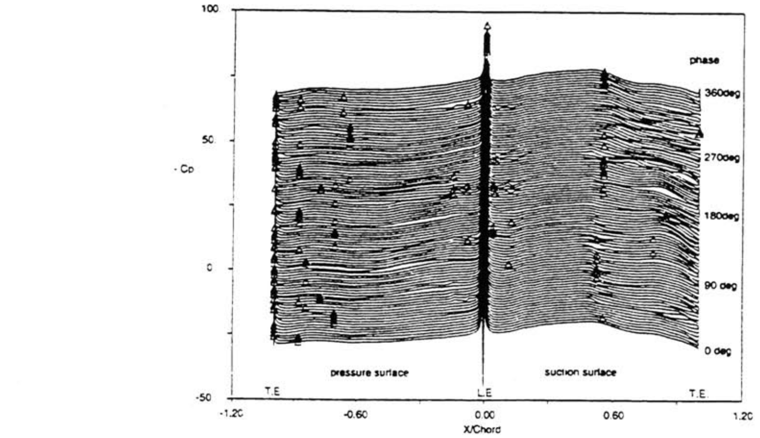

(c) e^n method only

Figure 5.23: Effect of the transition point model on the timewise blade surface pressure distribution

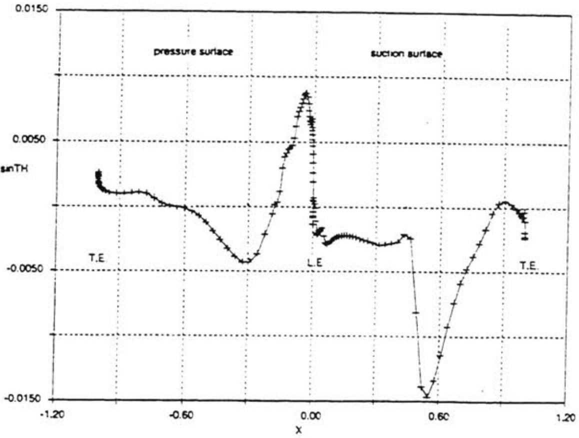

(a) Fixed transition point

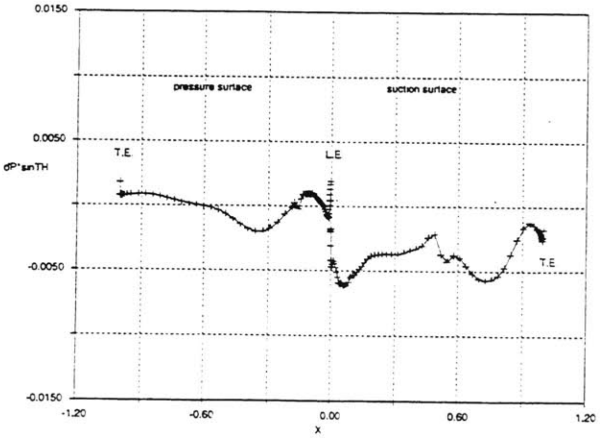

(b) Current model

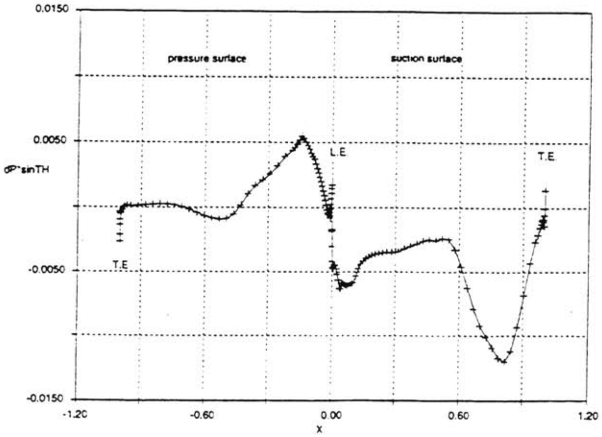

(c) e^n method only

Figure 5.24: Effect of the transition point model on the blade surface energy distribution

5.11 Cusping of the trailing edge

The code has been shown to be an plausible tool for the flutter mechanism study, but there remains a problem that the calculation time takes too long for the practical design calculations. The stationary calculation shown in Fig. 5.16 took about a week of calculation for 223 × 70 mesh points by DECstation 5000/200. Since the reduced frequency of the interest is very low, it was estimated that a case of the unsteady calculation with the blade oscillation would take a month. Therefore, a way to reduce the calculation time was sought. Of course the easiest way is to use a faster computer. But there is also room for improvement by modifying the code or the grid. One way is to reduce the number of grid points, but this depends on the case and is hard to generalize. Another way is to cusp off the trailing edge to increase the CFL number. From observations, most of the code failures occurred at the trailing edge where the grid direction suddenly turns 90 degrees. Adding a little pinch to the trailing edge shape could eliminate such a sudden direction change and can make the code more stable.

Fig. 5.25 show three types of the cusp studied. Type-A is just a little pinch and the grid still has the direction change as large as 40 degree. Type-B is a larger pinch and the maximum grid direction change is reduced to 20 degree. Type-C is the full cusp covering the whole trailing edge circle.

Fig. 5.26 shows the timewise blade surface pressure distribution of the case without a cusp and a case with type-B cusp. A significant difference in the frequency of the vortex-shedding is seen. But this is not a problem because the frequency of the vortex-shedding in the case without the cusp is two orders of magnitude higher than the blade natural frequency therefore this won't cause a difference in the blade exciting force. The averaged Mach contours of both cases are similar(Fig. 5.27). Therefore, it can be concluded that cusping off the trailing edge with type-B cusp won't affect the unsteady blade oscillating force which is our current interest.

The type-A cusp didn't show appreciable increase of the CFL number from the no-cusp case, and type-C cusp didn't show appreciable difference of the CFL number increase from type-B cusp case. So, it was concluded that type-B cusp is the best among the three cusps to use in current calculations.

Another possibility to increase the CFL number is to use combined O-C or O-H grid to eliminate any of the sudden grid direction change without altering the blade shape. This is also better because the grid around the blade surface can have a better distribution. However this option will be left just as a suggestion for future work.

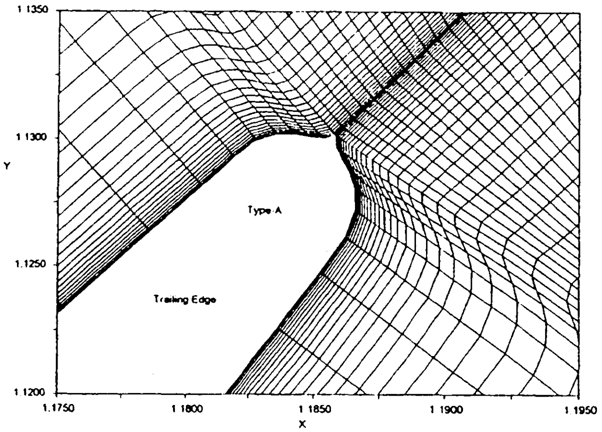

(a) Type-A

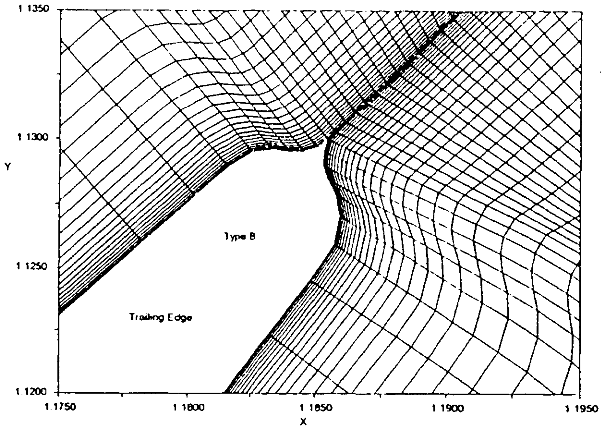

(b) Type-B

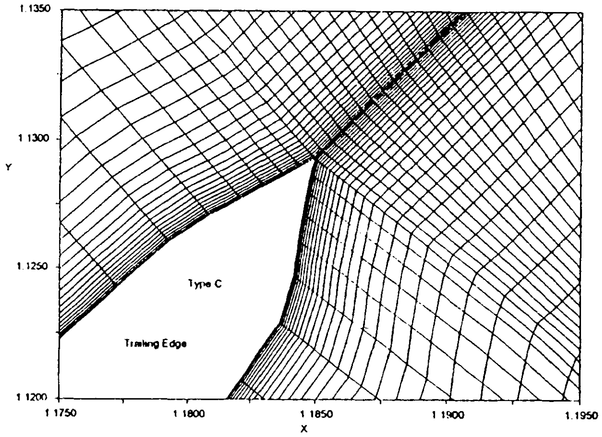

(c) Type-C

Figure 5.25: Three types of the cusps on the trailing edge of NASA rotor 67 30% span from the shroud

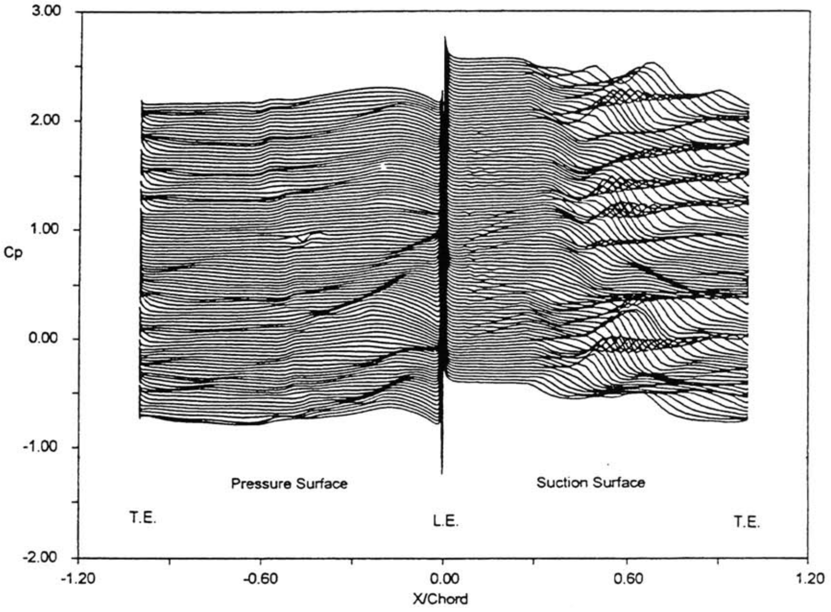

(a) Without cusp

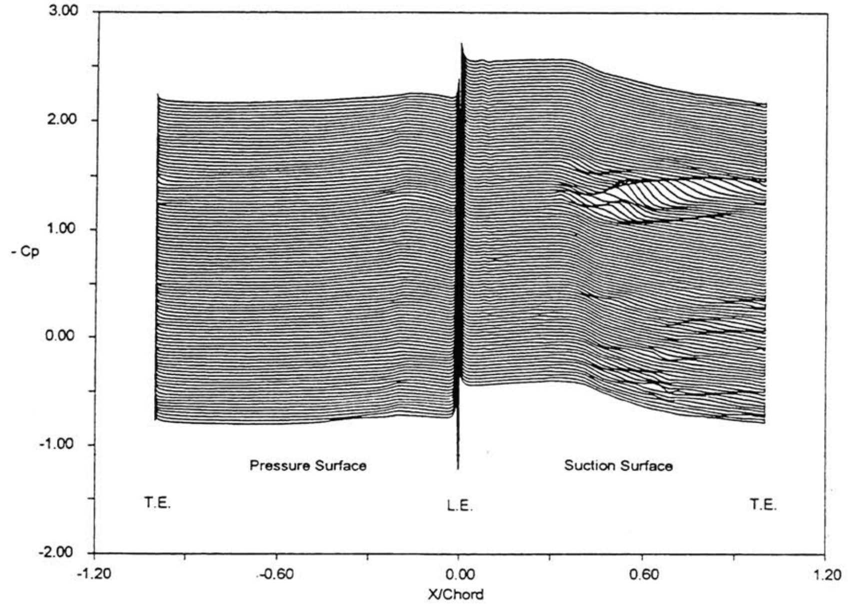

(b) With Type-B cusp

Figure 5.26: Timewise blade surface pressure distribution of the calculations with cusps

NASA rotor67 steady flow ....Near stall

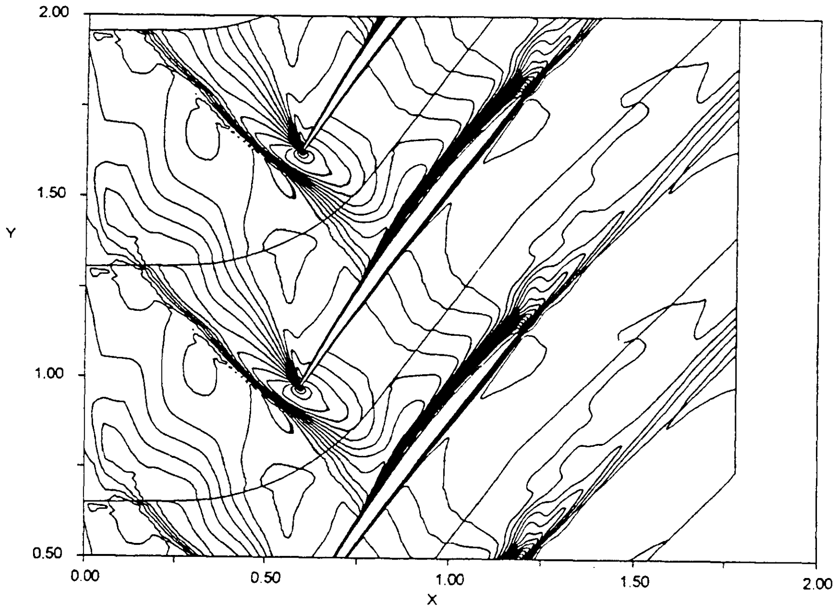

(a) Without cusp (Time averaged)

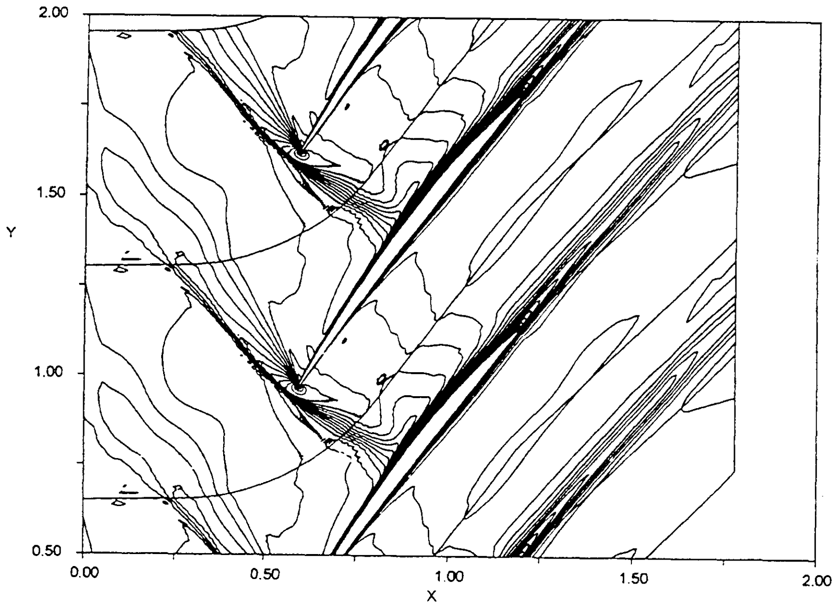

(b) with Type-B cusp (Instantaneous)

Figure 5.27: Mach contour of the calculations with cusps

NASA rotor67 steady flow ....Near stall

5.12 Effect of the downstream region length

In flutter simulations in transonic flow, the accurate simulation of the wave system is very important since the wave system will force the shock wave to move, or oscillate and the shock motion may generate the dominant unsteady blade exciting pressure. To eliminate the wave reflection from the inflow and the outflow boundary, a non-reflecting boundary condition is employed in the code. But the non-reflecting boundary condition used in the code is a one dimensional condition, and will only suppress the wave propagating normal to the boundary. The components of the wave in the dimension tangential to the boundary may reflect back to the blade and influence the shock wave system. The outflow boundary is more important than the inflow boundary because the pitchwise nonuniformity of the flow is larger due to the wake. On the other hand, the inflow boundary is set far enough from the blade so the shock wave becomes weak enough to be suppressed by the boundary condition.

A way to check if there is any influence of the wave reflecting back from the exit boundary is to compare calculation results with several different downstream region lengths. If there is no appreciable difference, the code is validated for its ability to simulate the unsteady transonic flow with shock waves.

Three calculations with different downstream region lengths were done at the inter-blade phase angle 240 degree. This case was chosen because clear shock motions were seen without extremely long calculations. Two cases, (1) 2.6 × chord, and (2) 1.1 × chord were done.

The results are shown in Fig. 5.28. No difference is seen in the blade surface unsteady wave system. Therefore it has been shown that there is no wave systems reflected from the outflow boundary affecting the unsteady calculation results, such as unsteady shock motion.

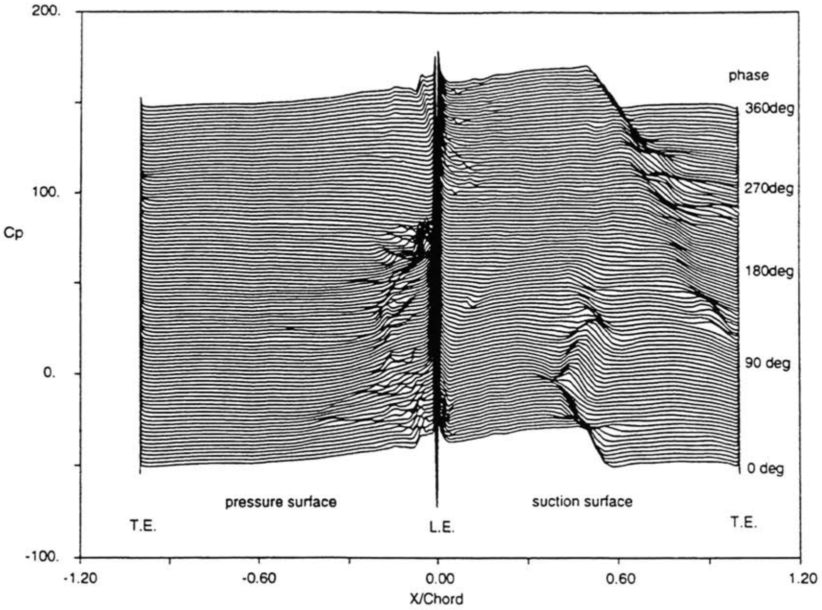

(a) Long exit region (2.6 × chord)

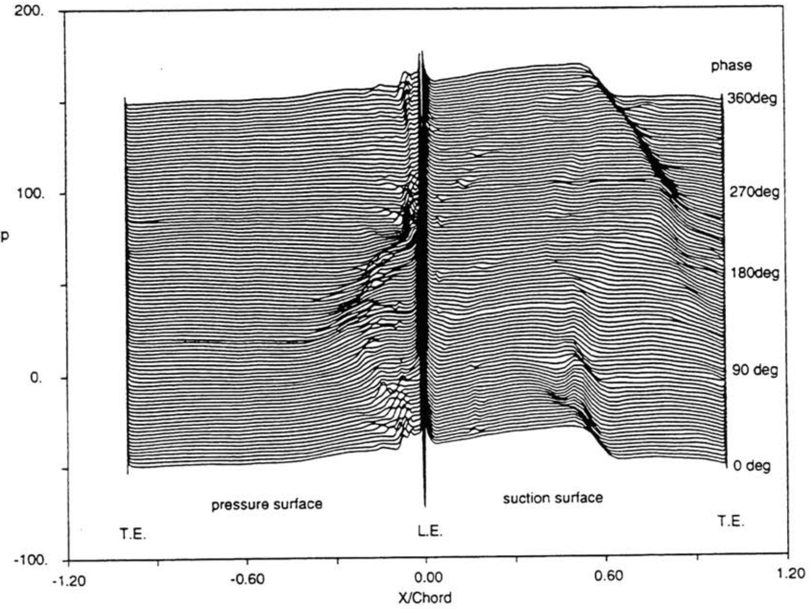

(b) Short exit region (1.1 × chord)

Figure 5.28: Effect of the downstream region length

NASA rotor 67 ....Near stall σ = 240 deg.

5.13 Summary of the code validations

From the series of the validation calculations described above, the code has been validated as a reasonable quasi-three-dimensional tool to simulate the unsteady flow in transonic cascades. Also from the test case of NASA rotor 67, the quasi-three-dimensional tool has been shown its capability of accurately simulating a slice of blade-to-blade flow in a three-dimensional flow field. From these results, the author has proceeded to flutter simulation calculations of a transonic fan by the code, FCASQ3.

Chapter 6

Flutter simulation of IHI transonic fan

A research transonic fan rig provided by IHI Co Ltd. has been used as the model for the flutter simulation calculation. The fan experienced flutter at mid-speed high pressure-ratio conditions during rig tests. The simulation calculations were performed at the near-flutter conditions and at in-flutter conditions. The input data for near-flutter aerodynamic condition calculations were obtained from through flow calculations using data measured in the rig test. The input data for in-flutter condition calculations were obtained by extrapolating the through flow calculation results from the points with no flutter because aerodynamic data could not be measured during flutter.

Using the rig data, parametric calculations were performed to answer questions listed in the section 1.3. One benefit of numerical simulations is that a single parameter can be easily perturbed at a time to separate the effect of the parameter. First, the effect of the vibration amplitude is checked to find a proper amplitude to use in the following calculations. Then the code is checked whether the flutter seen in the rig test can be simulated. This is done as follows.

1. Vary the inter-blade phase angle and see if the inter-blade phase angle to give the minimum aerodynamic stability matches that seen in the rig test, -32.7 degrees.
2. Perturb the pressure ratio to simulate increasing the pressure ratio along the constant speed line in the fan characteristic map. See if the blade-exciting aerodynamic energy appears at the pressure ratio which flutter was observed in the rig test.

The mechanisms of the flutter can also be found from these parametric studies, by observing the variation of the source of the blade exciting energy when the parameters are perturbed.

Some parametric studies provide information useful for blade design engineers. Two of these follow. The effect of the reduced frequency is studied to see if the increase of the natural frequency of the blade suppresses this flutter. The effect of the Reynolds number is studied to find out if a scaled rig test is a valid method to confirm the flutter boundary of the engine.

Finally, the spanwise variation and spanwise integration of the unsteady aerodynamic energy are examined to see if a strip-theory approach is applicable for quantitative prediction of the fan flutter.

In this chapter, the detail of the IHI fan rig data is explained first, followed by the results of the parametric calculations.

6.1 Rig data

The research fan rig has the cross section shown in Fig. 6.1. The specification of the fan is tabulated in Table 6.1. The blades have a multiple circular arc (MCA) type cross section, which is typical of modern transonic fans. The characteristics of the fan is shown in Fig. 6.2. From the characteristics, we can see a deep intrusion of the flutter boundary into the intended operating line at around 75% of the design fan speed high loading side. This intrusion forms a very sharp and narrow kink, as is shown in Fig. 6.3, and the fan tip relative Mach number at this kink is about unity. This kink cannot be predicted by classical methods, i.e. by the graph of the relation of reduced velocity (or reduced frequency) versus incidence as is shown in Fig. 6.4. The flutter boundary is jagged and the incidence angle varies by as much as 1.2 degrees. The jagged flutter boundary suggests that the mechanism of transonic flutter differs from that of subsonic stall flutter, for which the trailing edge stall due to high loading causes a phase shift in unsteady lift. One may imagine that shock waves may be involved in the mechanism of transonic flutter and therefore the classical method cannot work accurately enough as a tool to predict the flutter boundary for practical fan aero-mechanical design. Thus, we would like to find the mechanism of this flutter.

Table 6.1: Specifications of the IHI research fan

Number of the blades	22	
Fan diameter	75.8	[cm]
Fan inlet hub/tip ratio	0.302	
Design fan speed	10663	[rpm]
Design pressure ratio	1.6247	
Design flow rate	177.4	[kg/sec]
Design tip relative Mach number	1.474	
Blade L.E.span/tip chord	1.924	

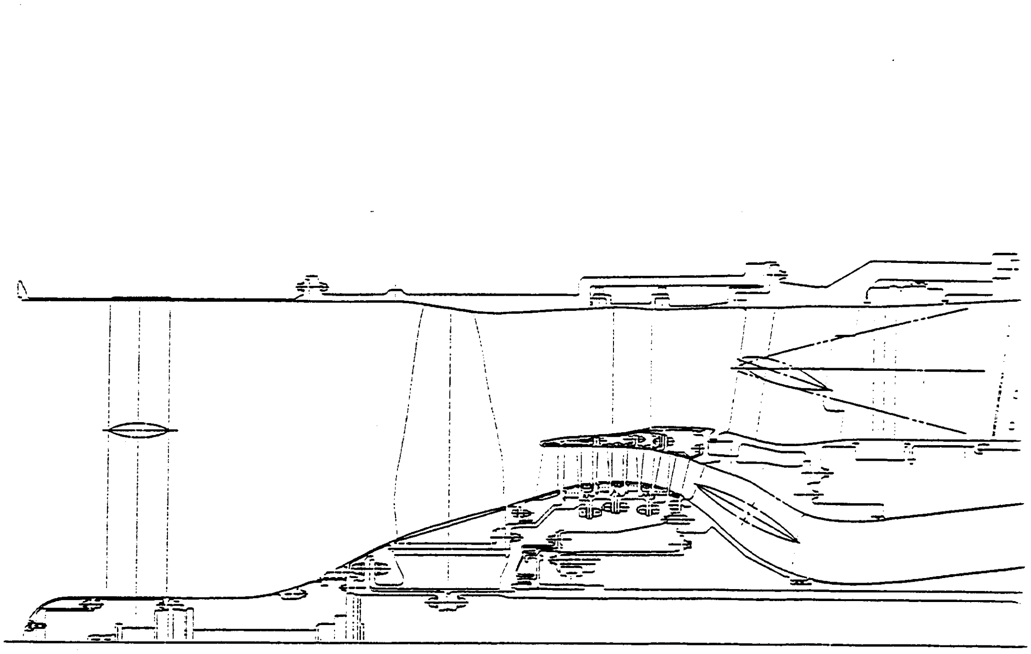

Figure 6.1: Cross section of the IHI transonic fan rig

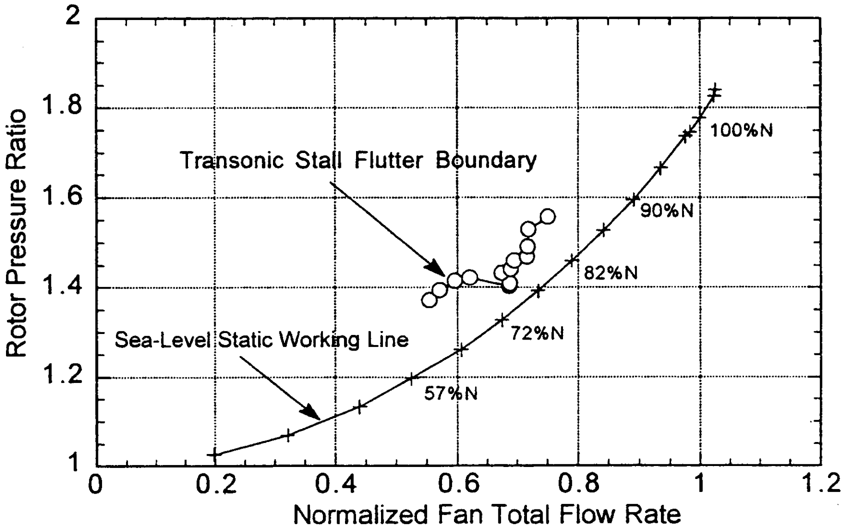

Figure 6.2: The flutter boundary of the IHI transonic fan rig

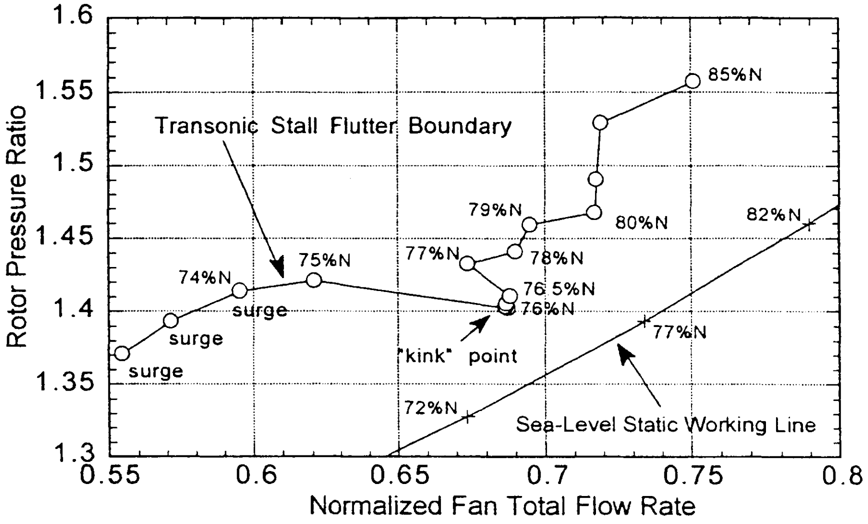

Figure 6.3: The blow up of the transonic flutter pinch point

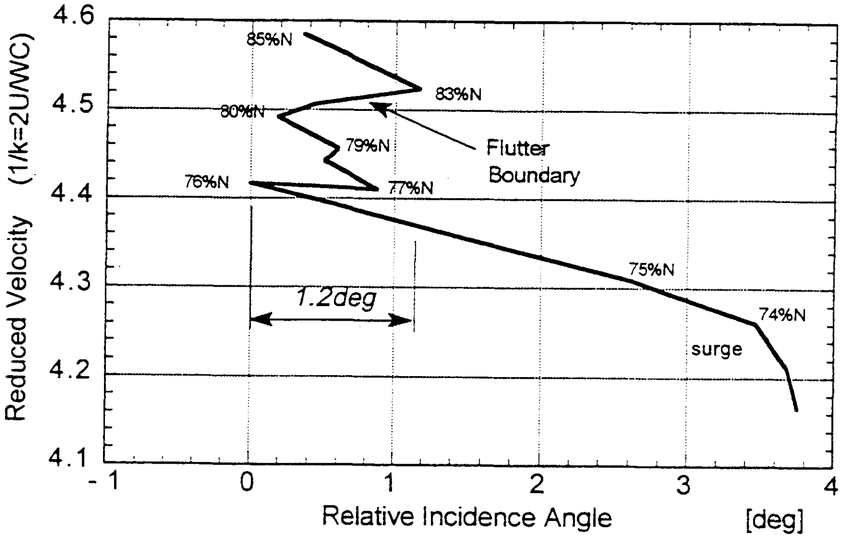

Figure 6.4: i-1/k diagram of the transonic flutter (at 85% span)

6.2 Input data

The blade geometries used in the simulation calculations are transformed from actual blade geometries along conical surfaces. The conical blade geometries are derived by interpolating the original constant-radius geometries using the streamlines calculated by a through-flow calculation (streamline curvature calculation) at the fan speed of interest. The blade-to-blade passages to be used in the calculations are transformed from the conical to a cylindrical surface by keeping the pitch at the leading edge and matching the rate of the passage area variation.

The radius for the blade-to-blade calculation is chosen by considering the radial distribution of the rotor pressure ratio rise. In Fig. 6.5, it is seen that the pressure ratio does not increase around the 85% span position when the fan overall pressure ratio is raised by closing the exit valve. Radial distribution of the loss coefficient $(\Delta P_t / P_{tin})$ calculated from rig data in Fig. 6.6 shows a large increase of the total pressure loss around this radius. The relative inflow Mach number is unity around this radius which implies the existence of a loss mechanism related to the normal shock wave at that spanwise position. However it is yet not clear whether a mechanism related to the flutter lies at this position or not.

Since the calculation code FCASQ3 is quasi-3D, the code cannot simulate three dimensional phenomena. Therefore, the phenomenon of not having pressure rise at 85% span should be checked to see if it can be handled by the current code. If it cannot be simulated by the current quasi-3D code, then the flowfield calculated by the quasi-3D code can be very different from the three-dimensional flowfield in the fan, and therefore this spanwise position should not be chosen for the flutter simulation calculations.

Steady calculations at the "*high*" valve position and the "*low*" valve position were each performed at the 79.3%, 85.6%, and 91.2% span positions. The results are shown in Fig. 6.7. The results showed the same tendency as the rig data, i.e. no pressure ratio rise at 85.3% span position. Therefore the capability of the current quasi-3D code to simulate this important aspect of the flowfield at 85.3% span has been shown, and this spanwise position has been chosen as the radius to start the flutter simulation calculations because the loss mechanism at this span position may be related to the flutter.

The static pressure contours of the flow fields are shown in Fig. 6.8. Among the shock waves shown here, the detached normal shock at the 85.3% span position is the strongest. The reason that there is no total pressure rise at 85.3% span is probably due to loss generated by the strong normal shock wave and by its interaction with the blade surface boundary layer.

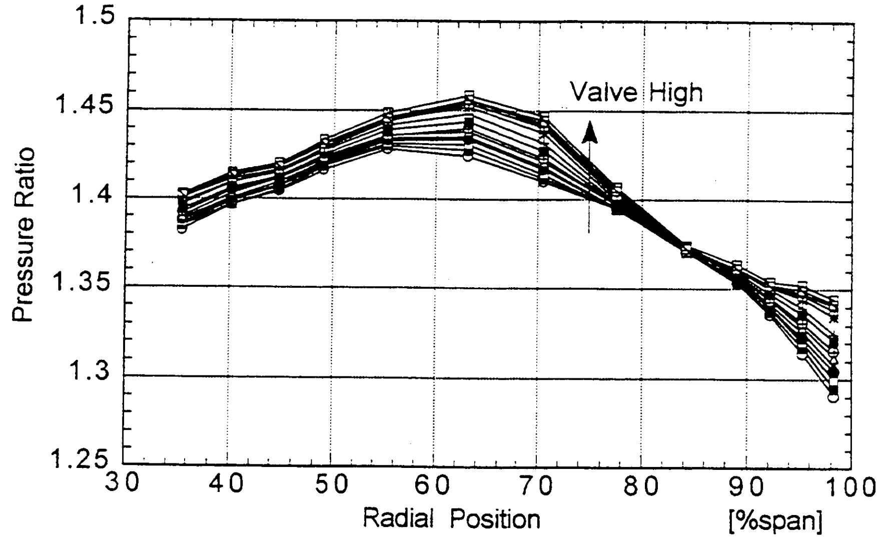

Figure 6.5: Change of the fan pressure ratio distribution by closing the exit valve

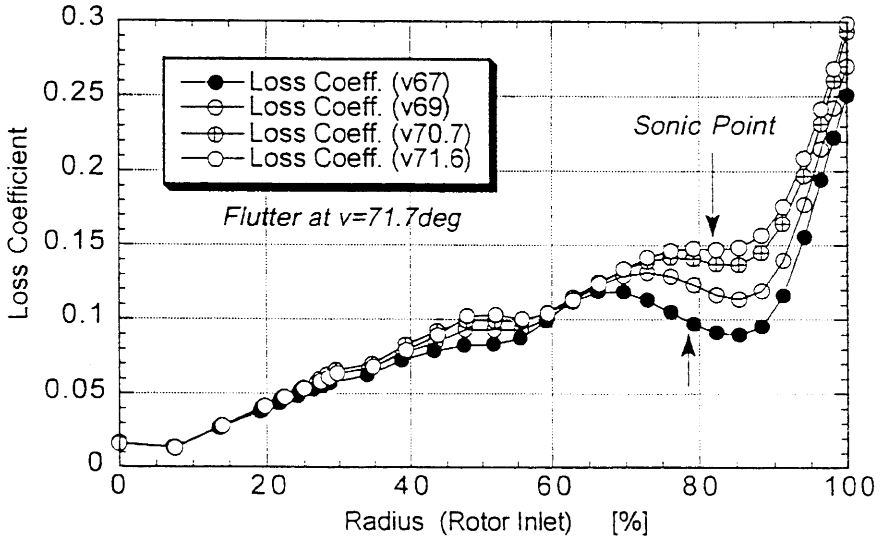

Figure 6.6: Change of the loss coefficient distribution by closing the exit valve

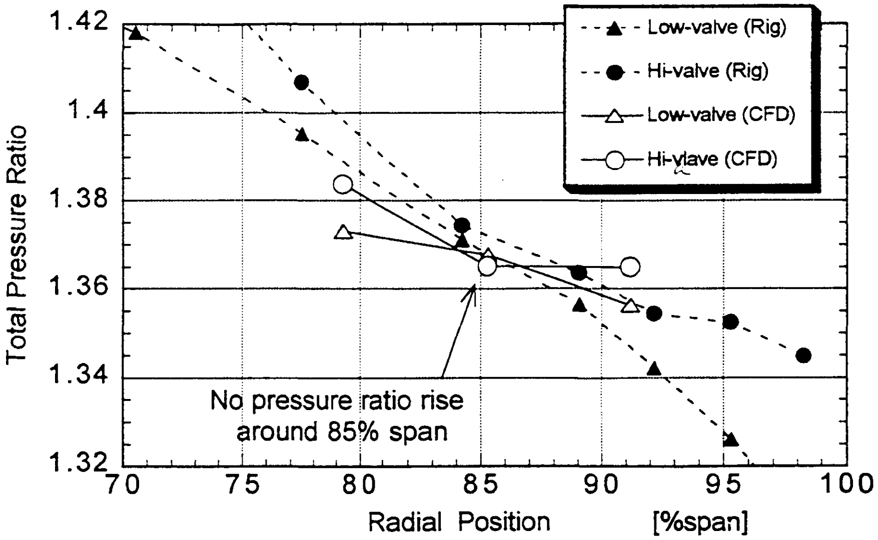

Figure 6.7: Fan pressure ratio distribution calculated by current quasi-3D code

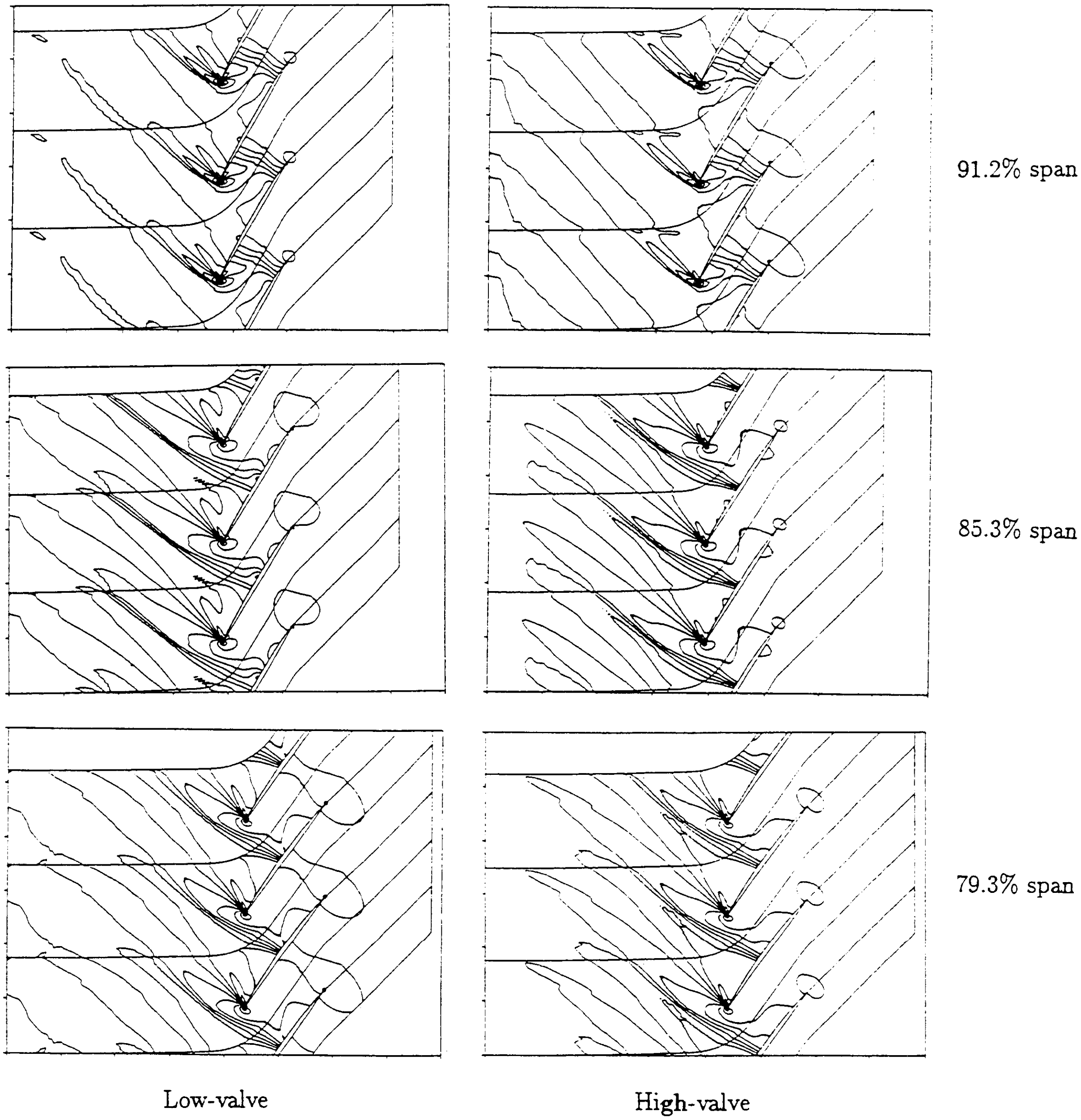

Figure 6.8: Static pressure contours of steady flowfield at 3 different spanwise positions

The aerodynamic data for non-flutter and near-flutter points were taken from the through-flow calculations based on the measured rig data, and those for in-flutter points were calculated by extrapolating the near-flutter and non-flutter points data. These points on the characteristic map are shown in Fig. 6.9. The data are tabulated in Table 6.2.

Table 6.2: Input data for IHI rotor flow calculations

Fan % speed	79%		76%		
Case	In flutter	Near flutter	In flutter	Near flutter	
Rel. Mach No.	1.012	1.0175	0.977	0.984	
Rel. velocity	336	338	324.5	326.5	[m/s]
Inflow angle	69.1	68.5	68.7	68.0	[deg]
P_s ratio	1.32	1.30	1.29	1.27	
Blade chord	14.67	14.67	14.67	14.67	[cm]
Kin. viscosity	1.779	1.847			$\times 10^{-5}$ [m^2/sec]
Reynolds No.	2.77	2.68			$\times 10^6$

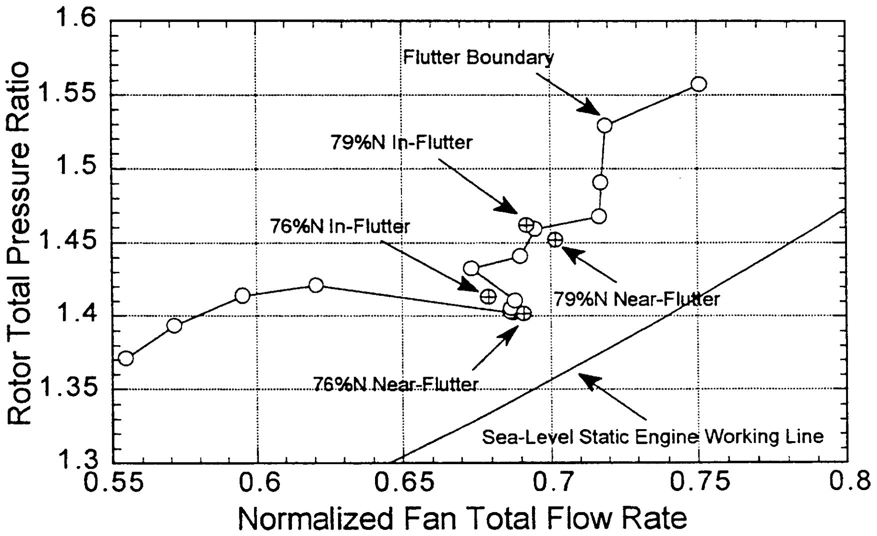

Figure 6.9: The operating points of the simulation calculations

The operating point of the flutter calculation was chosen to be not at the flutter kink, but at slightly higher speed, 79% speed. This is due to the observation during the rig test that the repeatability of the flutter boundary is better at the fan speed above the kink. Although the error of the rig measured data is less than 1%, the rig data showed poor repeatability of the flutter boundary at the fan speed below the kink point. There is also an error in the CFD results which arose from the circumferentially averaged inflow and outflow boundary conditions taken from the through-flow calculations based on the measurements. In addition, the growth of the blade vibration amplitude at the flutter boundary is far faster at this point than the region around the kink. Thus the calculation at 79% speed is less likely to miss simulating the flutter condition than at the kink point.

6.3 Steady flow field at 79% speed, 85.3% span

At 79% fan speed, it was observed during the rig flutter test that the blades developed strong flutter with just a slight change of exit valve angle, and that the flutter boundary had good repeatability. Therefore this speed has been chosen as the point to perform a variety of investigations to reveal the general mechanisms of transonic flutter.

Steady-state flowfields at the fan speed and the spanwise position chosen to conduct flutter simulation calculations are shown here to see such features as the position of the shock waves and the extent of the separations.

The Mach contour of the steady calculation at "Near Flutter" point (Fig. 6.10) shows that the shock wave has just detached, while the shock wave is fully detached at the "In Flutter" condition (Fig. 6.11). While the "Near Flutter" case has the flow attached even on the suction surface behind the shock foot (Fig. 6.12), the "In Flutter" case shows rather large separation region on the suction surface behind the shock foot (Fig. 6.13).

A second steady state calculation with "In Flutter" condition is performed, but with the static pressure ratio raised from 1.32 to 1.34 to investigate the sensitivity of the steady state shock position to the pressure ratio. This condition is called the "Deep In Flutter" condition. A separation region exists as shown in Fig. 6.14, but the scale of the region is smaller than that of the "In Flutter" case. The Mach contour in Fig. 6.15 shows that the shock position has moved forward, and the shock wave is now fully detached.

The important differences of the flowfield observed at these conditions are summarized in Table. 6.3.

Table 6.3: The important differences in the flowfield in & out of flutter

Flutter condition	Aerodynamic events
Near flutter	Shock just detached.
In flutter	Large separation behind the detached shock.
Deep in flutter	Fully detached shock. Smaller separation region.

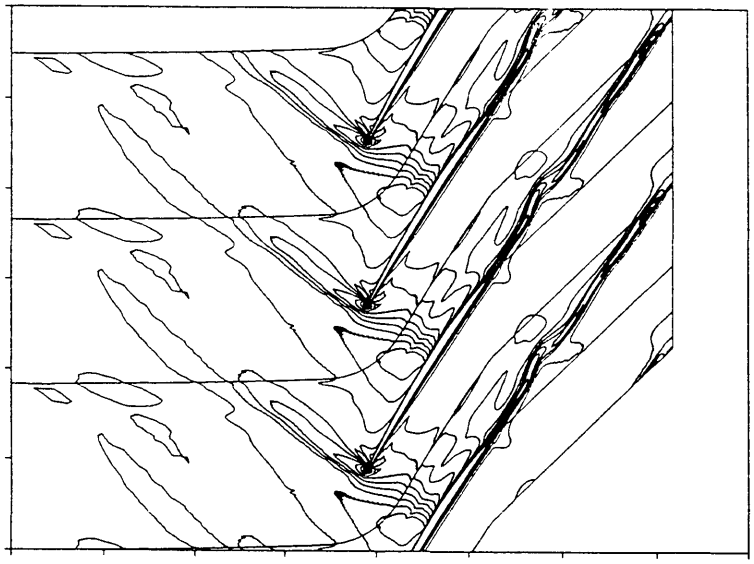

Figure 6.10: Mach contour of the steady calculation of IHI transonic research fan at a "Near Flutter" condition

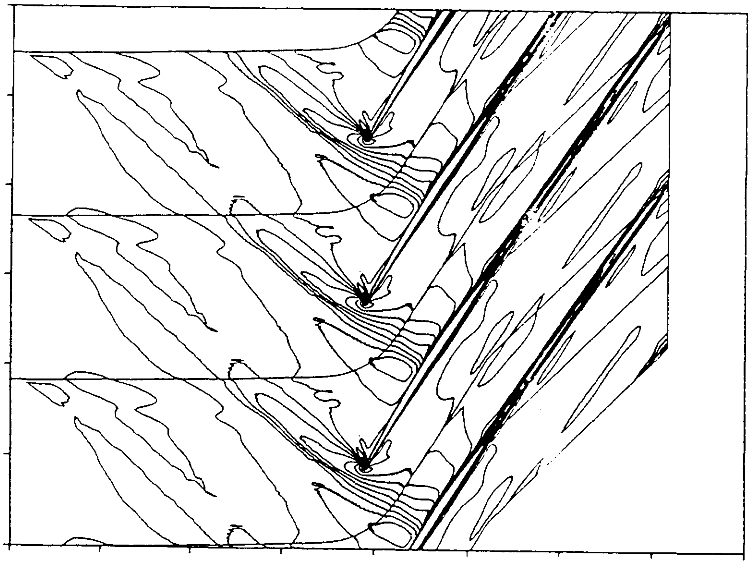

Figure 6.11: Mach contour of the steady calculation of IHI transonic research fan at a "In Flutter" condition

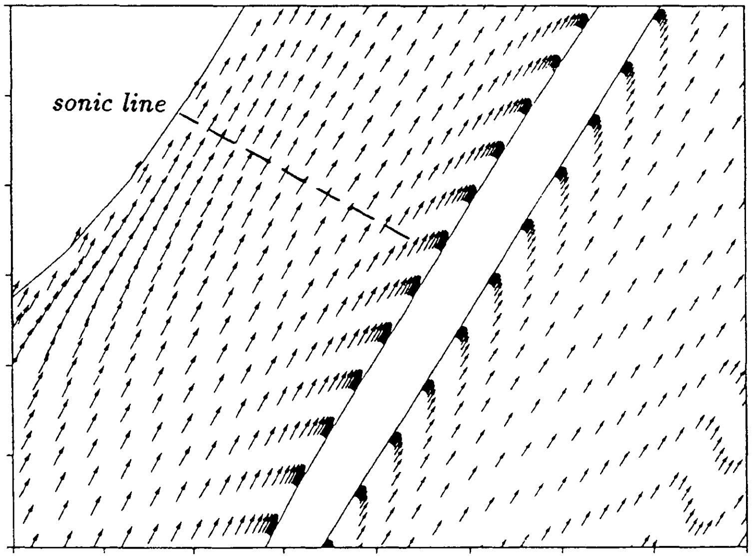

Figure 6.12: Velocity distribution behind the shock foot at a "Near Flutter" condition

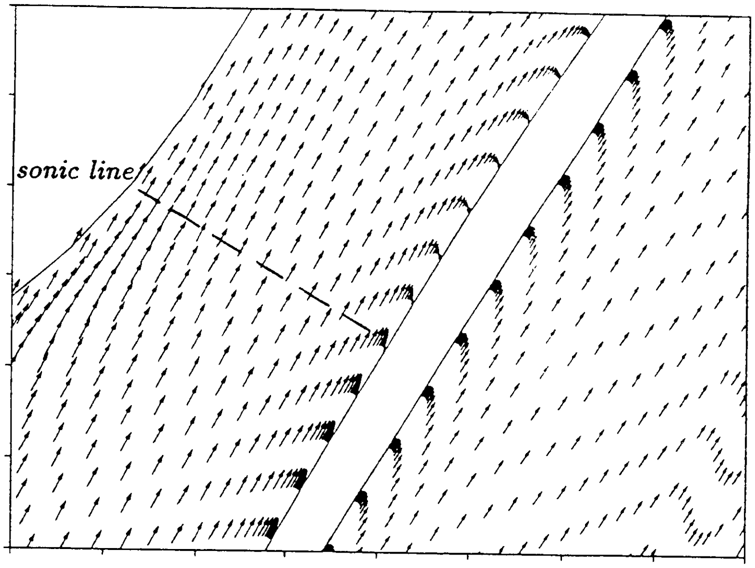

Figure 6.13: Velocity distribution behind the shock foot at a "In Flutter" condition

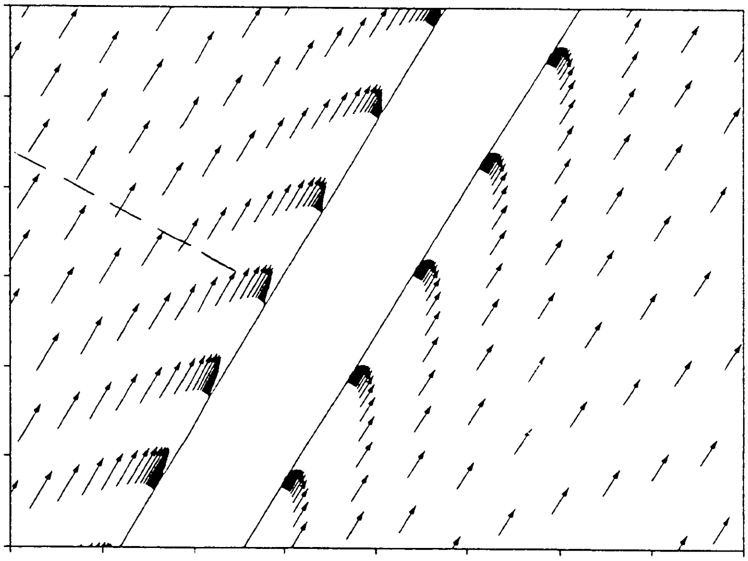

Figure 6.14: Velocity distribution behind the shock foot at a "Deep In Flutter" condition

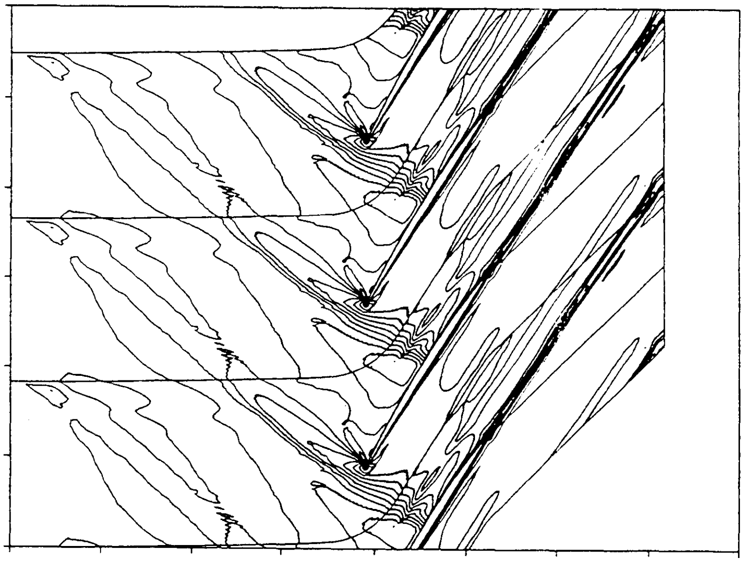

Figure 6.15: Mach contour of the steady calculation of IHI transonic research fan at a “Deep In Flutter” condition

6.4 Effect of vibration amplitude

If the blade oscillating amplitude affects our phenomena of interest, a careful selection of the range of the amplitudes for the simulation calculation is required so that important fluid dynamic phenomena are not missed. However, if the blade oscillating amplitude does not affect the aerodynamic event, calculations at one typical amplitude are enough. Therefore the influence of the blade vibration amplitude on the aerodynamic instability is checked here.

The amplitudes calculated were chosen from 2.5% pitch to 7% pitch, which are representative amplitudes encountered during flutters in engines and rigs.

The results in Table 6.4 and Fig. 6.16 shows no appreciable difference over the range of blade oscillation amplitude except for the 2.5% pitch case, where the phase angle showed large difference cycle to cycle of the blade oscillation. The reason for the difference in the 2.5% pitch case is that the absolute amplitude of the blade surface unsteady pressure due to blade oscillation is not large enough to lock the frequency of the mild separation and shock oscillation onto the blade oscillation frequency. Therefore a 2.5% pitch amplitude is not large enough for reliable calculations.

The other results showed good agreement regardless of the blade oscillation amplitude. This implies that the phenomenon causing flutter is insensitive to the blade oscillation amplitude, which rules out sudden occurrence of large separation from a certain blade oscillation amplitude, etc. The calculation can be done at any amplitude in this range and the results will hardly differ. Therefore the amplitude for the remaining calculations was chosen to be 4.5% pitch.

Table 6.4: Results of various reduced frequency calculations

blade oscillation amp.	amp.	phase
% pitch	C_p	deg
2.5	0.944	-17.1
4.5	1.041	-21.8
5.0	1.030	-22.6
7.0	0.869	-23.5

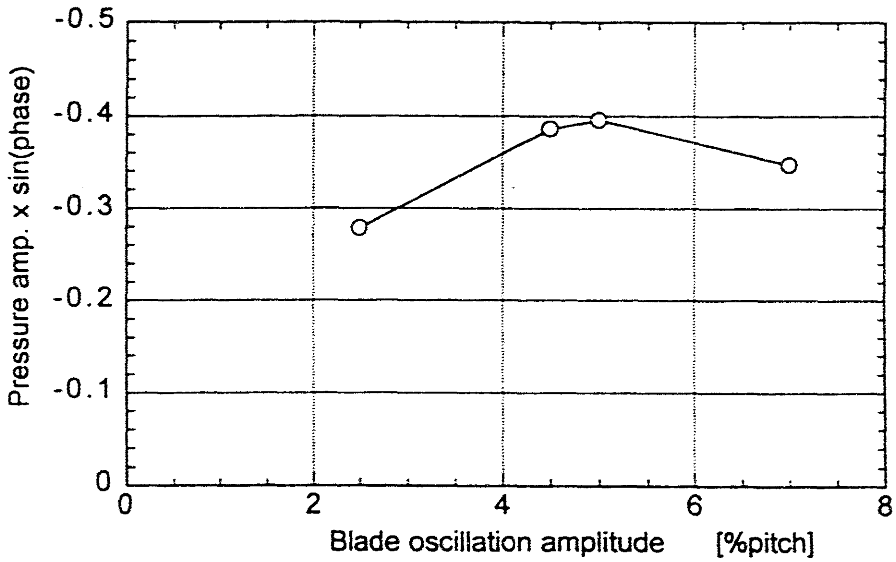

Figure 6.16: Aerodynamic stability change due to the blade vibration amplitude

6.5 Effect of inter-blade phase angle

Unsteady calculations at various inter-blade phase angles were performed to see whether the inter-blade phase angle which yields the minimum stability in the calculations matches that observed in the rig test, and to see what aerodynamic mechanisms generate the minimum stability at this inter-blade phase angle.

The variation of the blade exciting energy against the inter-blade phase angle at the "In flutter" condition is shown in Fig. 6.17. The blade exciting unsteady aerodynamic energy is calculated to be the largest (smallest damping force) at the inter-blade phase angle -32.7 degrees. This result agrees with the observation in the rig test.

The breakdown of the unsteady aerodynamic energies on the blade surface into five characteristic regions, namely shock-foot region, upstream of the shock-foot region, and downstream of the shock-foot region on both suction and pressure surfaces is shown in Fig. 6.18. It can be seen from this figure how the source of blade exciting energy varies according to the inter-blade phase angle. Note that the ordinate is the unsteady exciting energy per unit area. So a large value does not necessarily mean large blade exciting energy, because the area can be small depending on the magnitude of the shock oscillation amplitude (chordwise displacement). It is seen from the figure that the shock-foot on the suction surface and the shock foot on the pressure surface (due to the passage shock) work approximately in opposition energies. The sum of these two energies almost corresponds to the shape of the Fig. 6.17, implying that these two energies are the dominant energies working on the blade. It is the balance between these two energies which define the stability of the blade section. It can be seen from Fig. 6.18 that the source of the unstable blade total energy at inter-blade phase angle -32.7 degrees in Fig. 6.17 is the shock foot on the pressure surface.

Now that we recognize that the balance between the unsteady pressures due to the two shock feet controls the aerodynamic stability of the blade section, the mechanisms that vary the strength of the two shock feet are investigated. Fig. 6.19-a,b shows the variation of the amplitude and the phase of the unsteady pressure at the two shock feet. The amplitude of the shock foot on the suction surface is always larger than that on the pressure surface, and the difference of the two amplitudes stays approximately the same. So the variation of the amplitude is not responsible for the variation of the aerodynamic energy. Thus the phase must be responsible for the difference of the relative strength of the two energies. Fig. 6.19-b shows roughly symmetric phase variations but the phase of the energy on the pressure surface is shifted to left. This left shift results in the difference of the blade exciting energies.

The separation region behind the shock foot on the suction surface which is marked "S. S. downstream" in Fig. 6.18 works as a blade damping force at all the inter-blade phase angles. Therefore it has been shown that this flutter is not a stall flutter. The source of the blade exciting force is not a stall, but the unsteady shock foot of a passage shock near the blade's leading edge on the pressure surface.

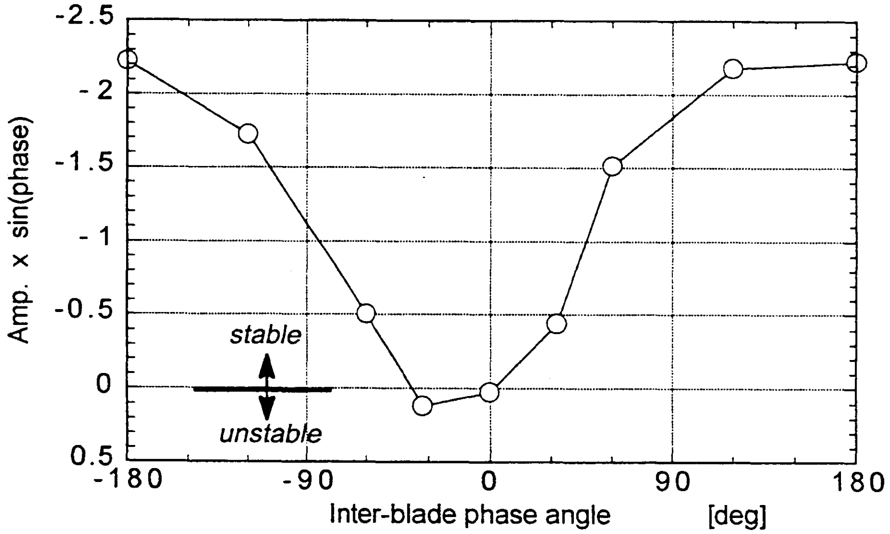

Figure 6.17: The effect of the inter-blade phase angle on aerodynamic blade exciting force

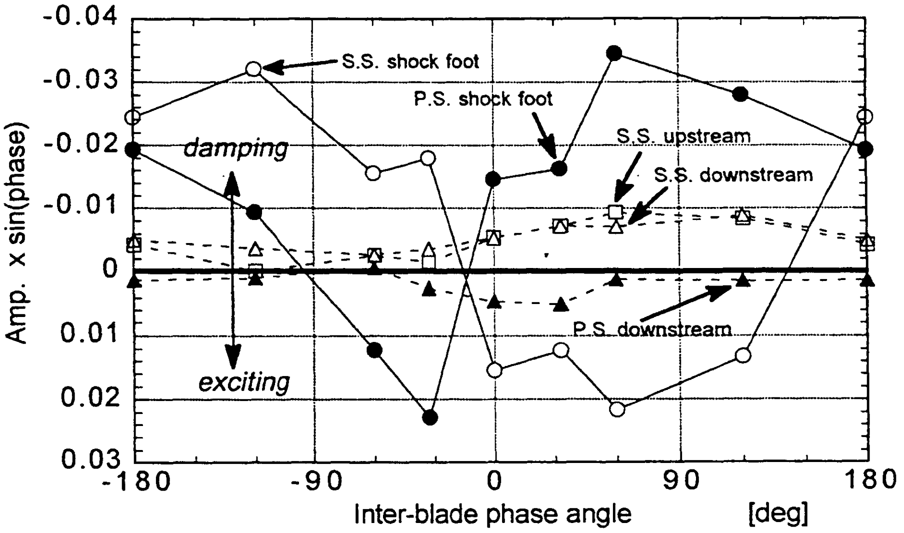

Figure 6.18: The effect of the inter-blade phase angle on the components of the aerodynamic force

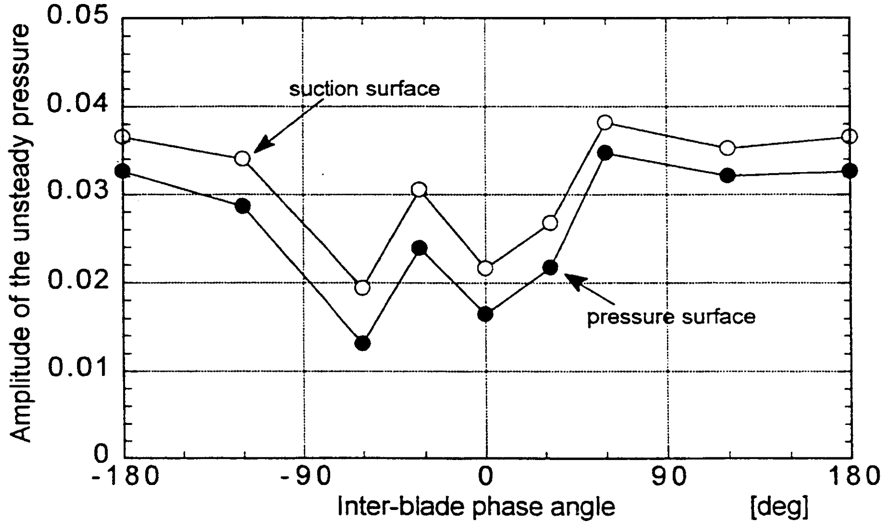

(a) Amplitude

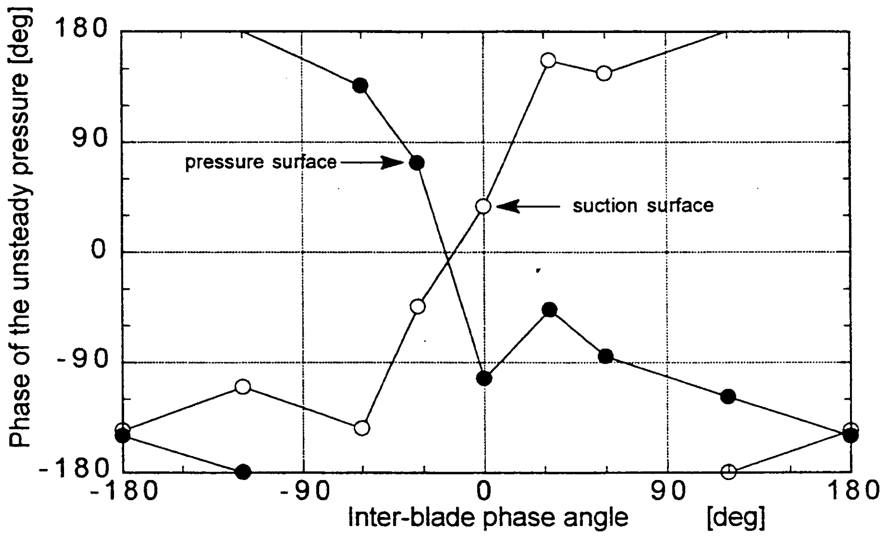

(b) Phase angle

Figure 6.19: The effect of the inter-blade phase angle on the amplitude and the phase of the unsteady blade surface pressure at the shock feet

6.6 Effect of fan pressure ratio

Calculations perturbing the rotor static pressure ratio were performed to investigate the effect of the pressure ratio. The pressure ratio is perturbed along the constant speed line in the fan characteristic map shown in Fig. 6.20. Therefore the inflow angle and the inflow Mach number are also perturbed accordingly. The idea is to investigate the effect of the blade loading through one parameter, the pressure ratio. The static pressure ratios were chosen to be around the point which the shock wave has just unstarted, i.e. 1.32. The inter-blade phase angle is -32.7 deg.

The result is shown in Fig. 6.21. Although the amplitude is not a maximum in Fig. 6.21-a, the phase angle in Fig. 6.21-b causes an unstable exciting energy at the static pressure ratio 1.32. The figure shows that the aerodynamic instability appears at the static pressure ratio 1.32, and the unsteady pressure is working as a blade exciting force only in the vicinity of this pressure ratio. This agrees with the observation in the rig test that the flutter subsided by further closing the exit valve at some fan speed. At most fan speeds, the exit valve could not be further closed because of the fan vibration amplitude limit for safe operation, so it could not be checked if this observation is true at all fan speeds.

The details of the unsteady blade surface pressures are seen qualitatively in a time-wise surface pressure distribution in Fig. 6.22. In the case of pressure ratio 1.30, a shock foot is visible on each surface, but the shock oscillation is less on the pressure surface. At pressure ratio 1.32, large shock oscillations are seen on both suction and pressure surfaces. In the case of pressure ratio 1.34, the shock wave is detached and the shock foot on the pressure surface has almost disappeared.

For the three pressure ratios, quantitative details of the unsteady pressure can be seen from the blade surface unsteady pressure amplitude distributions, phase distributions and energy distributions shown in Fig. 6.23, 6.24, 6.25, respectively. The unsteady pressure amplitude distributions in Fig. 6.23 show that the amplitude on the pressure surface is the largest in the case of pressure ratio 1.32, where the passage shock wave is just about to unstart. The phase distribution in Fig. 6.24 shows that the phase of the shock foot on the pressure surface has shifted to approximately 70 degrees at the pressure ratio 1.32, while it is approximately 180 degrees at the other pressure ratios. A phase angle contributes to a maximum blade exciting energy at 90 degrees and no blade exciting energy at 180 degrees. So the shock foot on the pressure surface works as a large blade exciting energy only at the pressure ratio 1.32. The blade surface energy distributions in Fig. 6.25 show that the shock foot on the suction surface behaves as a blade damping energy, and the passage shock foot on the pressure surface works as a blade exciting energy in the whole calculated pressure ratio range. Note that in Fig. 6.25 the unstable blade-exciting positive energies are shown with the positive axis up; in Fig. 6.21-c the positive axis was down. It is a balance between these two unsteady aerodynamic enérgies which determines the stability of the blade section. The displacement of the passage shock foot on the pressure surface becomes very large when the shock is in between the started and the unstarted positions, and this exerts the dominant blade exciting energy.

In each of these cases, no blade exciting force due to stall was detected. So the flutter could only have been caused by the displacement of the pressure side passage shock.

In summary the key mechanism that causes transonic flutter is the reduction of aerodynamic stability due to the position of the passage shock wave. The stability of the blade due to the unsteady aerodynamic energy reduces when the passage shock wave comes close to unstarting. The reasons for the blade exciting energy becoming large on the pressure surface near the leading edge at the pressure ratio 1.32 are:

1. the chordwise displacement of the shock motion is large at this pressure ratio when the shock is just about to detach, and
2. the steady pressure is high near the leading edge so the pressure jump due to the shock wave passing is large, and
3. the phase angle of the shock oscillation becomes a value which causes the phase angle of the unsteady pressure to be close to 90 degrees.

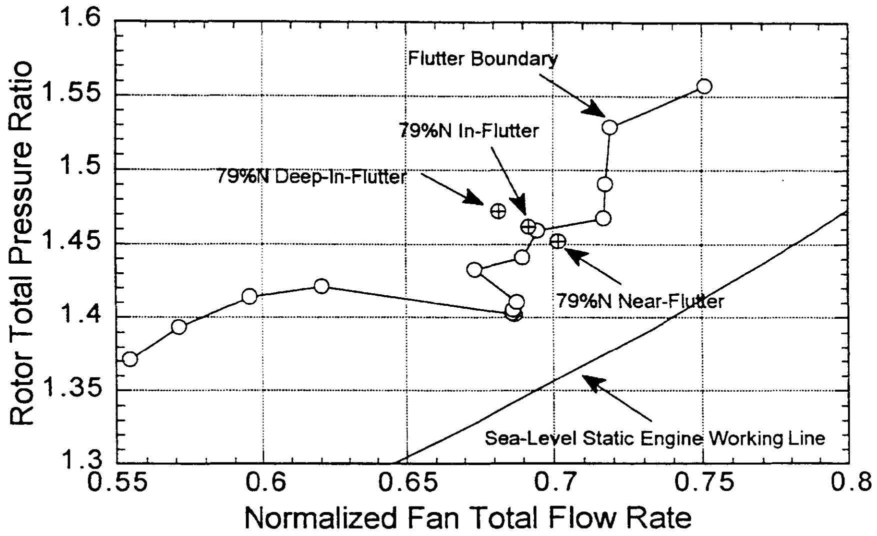

Figure 6.20: The fan operating points used in the perturbed pressure ratio calculations

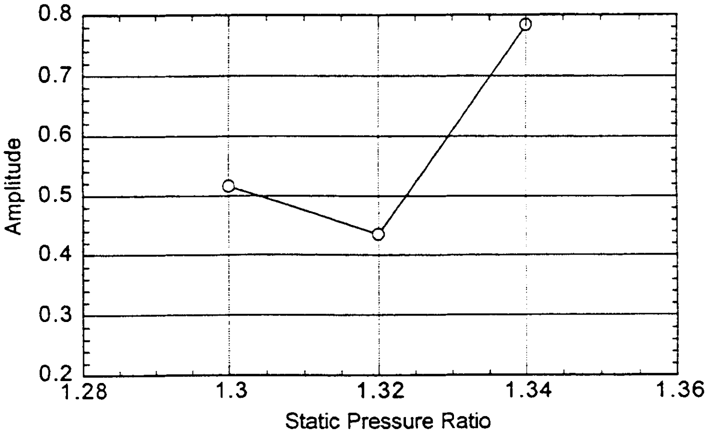

(a) Amplitude of the unsteady pressure

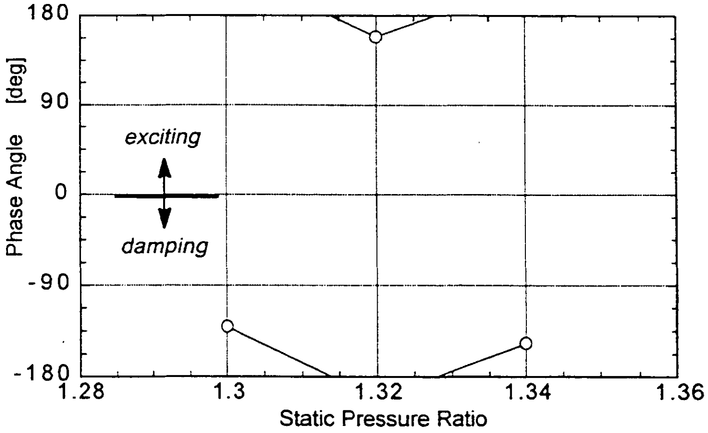

(b) Phase of the unsteady pressure

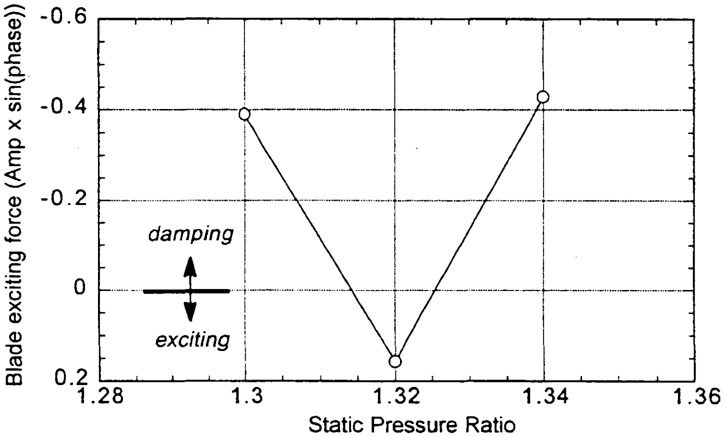

(c) Blade exciting force

Figure 6.21: Aerodynamic stability change due to the pressure ratio

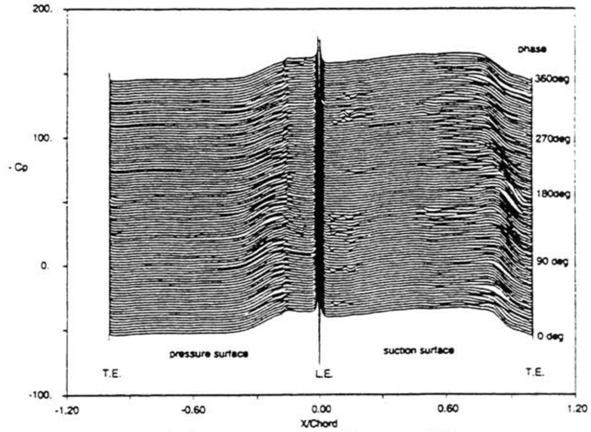

(a) pressure ratio = 1.30

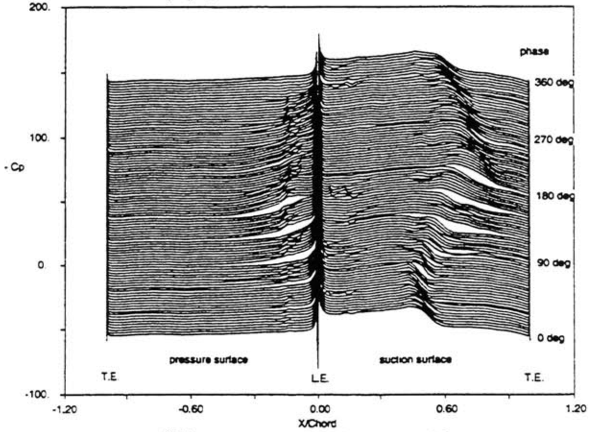

(b) pressure ratio = 1.32

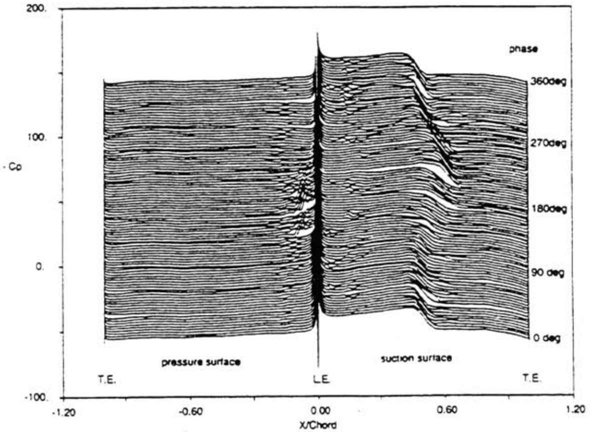

(c) pressure ratio = 1.34

Figure 6.22: Timewise blade surface pressure distribution (inter-blade phase angle -32.7 degree)

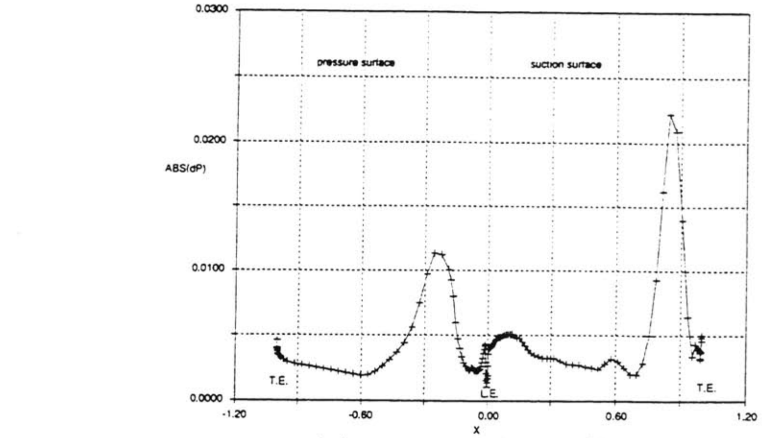

(a) pressure ratio = 1.30

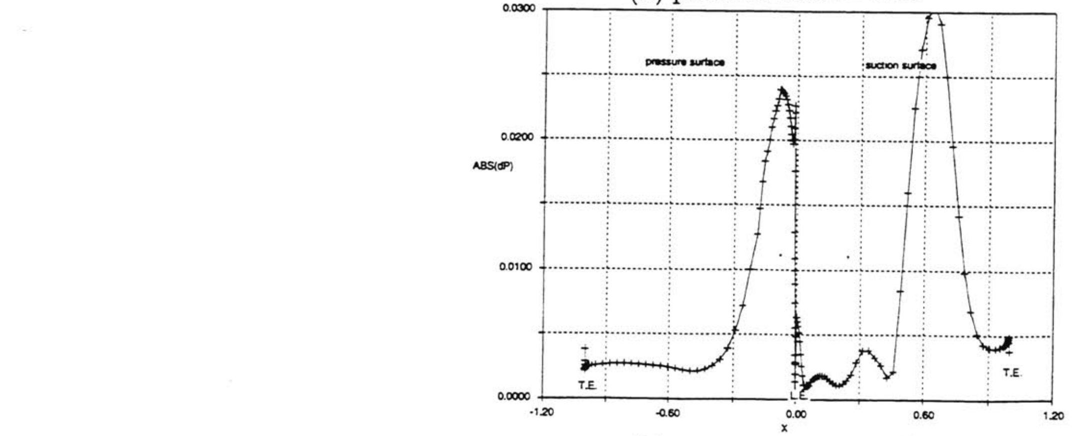

(b) pressure ratio = 1.32

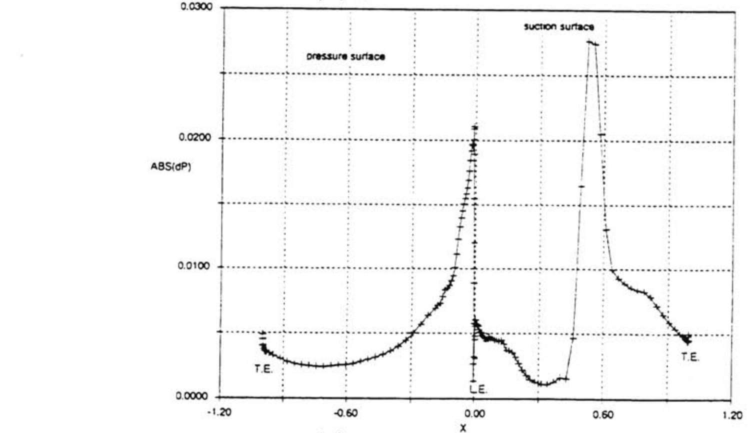

(c) pressure ratio = 1.34

Figure 6.23: Blade surface distribution of the amplitude of the unsteady pressure (inter-blade phase angle -32.7 degree)

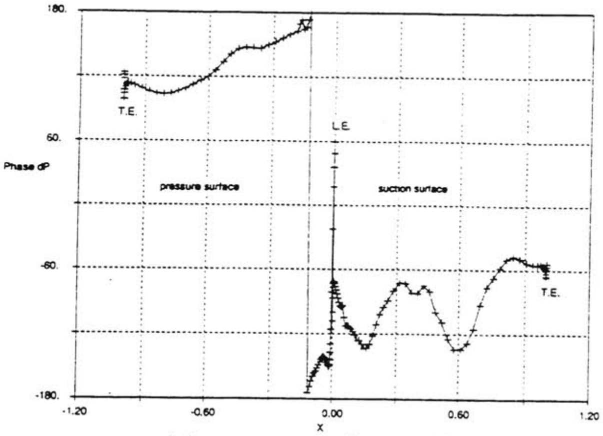

(a) pressure ratio = 1.30

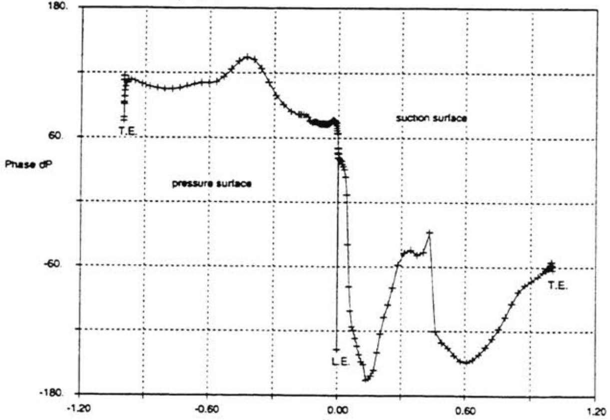

(b) pressure ratio = 1.32

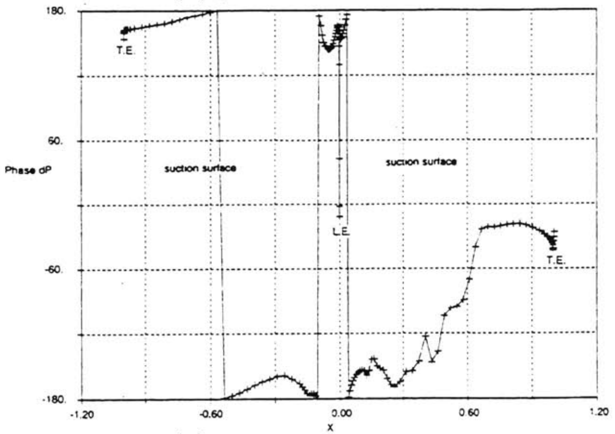

(c) pressure ratio = 1.34

Figure 6.24: Blade surface distribution of the phase of the unsteady pressure (inter-blade phase angle -32.7 degree)

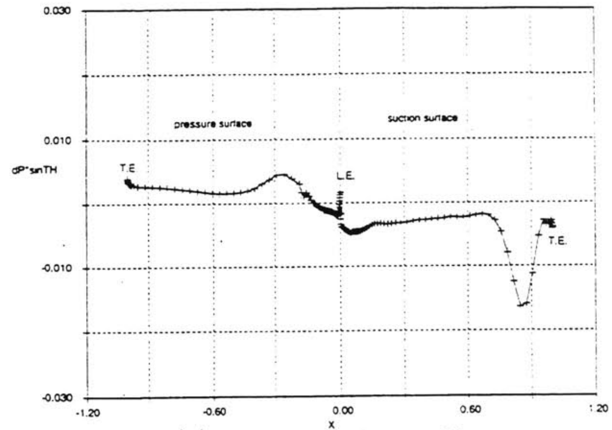

(a) pressure ratio = 1.30

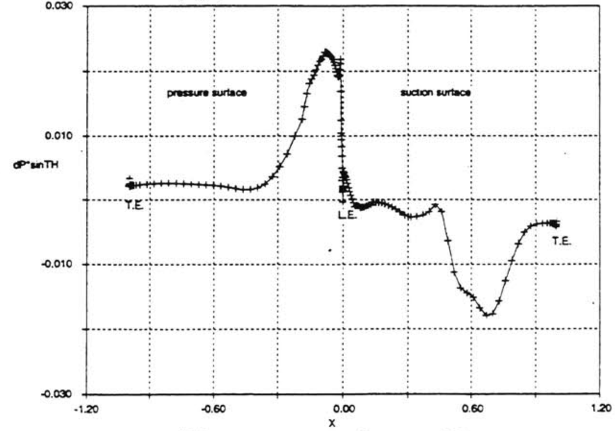

(b) pressure ratio = 1.32

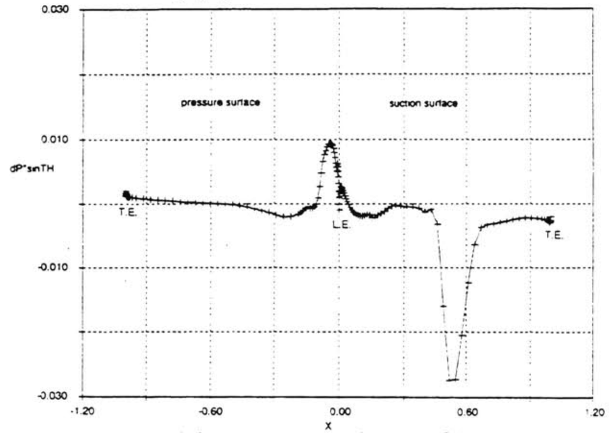

(c) pressure ratio = 1.34

Figure 6.25: Blade surface aerodynamic stability distribution (inter-blade phase angle -32.7 degree)

6.7 Effect of incidence angle

In a transonic fan, the shock position is defined by the inflow Mach number, the pressure ratio, and the passage area contraction, but not directly by the incidence angle. The incidence angle does change as a result of changes in the pressure ratio, and the inflow Mach number, or in the stagger angle, but the incidence angle itself does not change the inflow Mach number and the pressure ratio. The inflow Mach number and the pressure ratio are defined by the passage area change. In the case of a stagger angle change, the change in the stagger angle can cause the blade passage throat area to change, and will result in a change of the inflow Mach number. Therefore an incidence angle change affects the shock position indirectly instead of directly. The effect of the incidence angle change due to the pressure ratio change was discussed in the previous chapter. In current research, the data is limited to those of a transonic fan rig which has only one stagger angle, so the effect of changing stagger angle was not studied. This will be left as a subject for work in the future.

6.8 Effect of reduced frequency

The flutter in the rig occurred at the reduced frequency $K = \frac{\omega C}{U} = 0.44$. The effect of increasing the natural frequency of the blade on this flutter is investigated here. It is a common practice to increase the natural frequency of the blade to avoid flutter, and it is useful for designers to know whether this approach is effective for this flutter or not. This investigation checks whether the selected reduced frequency is high enough to be truly unsteady, or whether this phenomena can be treated by a quasi-steady approach gives this useful information on how to handle the problem most efficiently in practical flutter prediction calculations.

Calculations at various reduced frequencies were performed. All the calculations here were done at an inter-blade phase angle of 0 degrees, and static pressure ratio 1.32.

The results are shown in Table 6.5 and Fig. 6.26. At the reduced frequency (K) between 0.44 and 0.88, the phase decreases monotonically as K increases, and the aerodynamic stability increases. Therefore it has been shown that increasing the blade's natural frequency is an efficient method to suppress this flutter.

At K less than equal to 0.44, some flow separations were seen. At $K = 0.22$, flow separation causes large scatter of the phase because the period of the unsteady separation is not locked onto the blade oscillation period.

At $K = 0.44$, the unsteady flow separation and the blade oscillation is synchronized. Since the synchronization of the unsteady separation and the blade oscillation depends on the reduced frequency, the phenomena cannot be treated by quasi-steady methods. It is necessary to use unsteady tools to analyze this type of flutter.

Table 6.5: Results of various reduced frequency calculations

reduced frequency $K = \frac{\omega C}{U}$	pressure amp. C_p	pressure phase deg	note
0.22	-	-	scatter too large
0.44	0.758	-23.4	
0.66	0.743	-76.4	
0.88	0.684	-89.9	
1.32	0.275	-38.8	

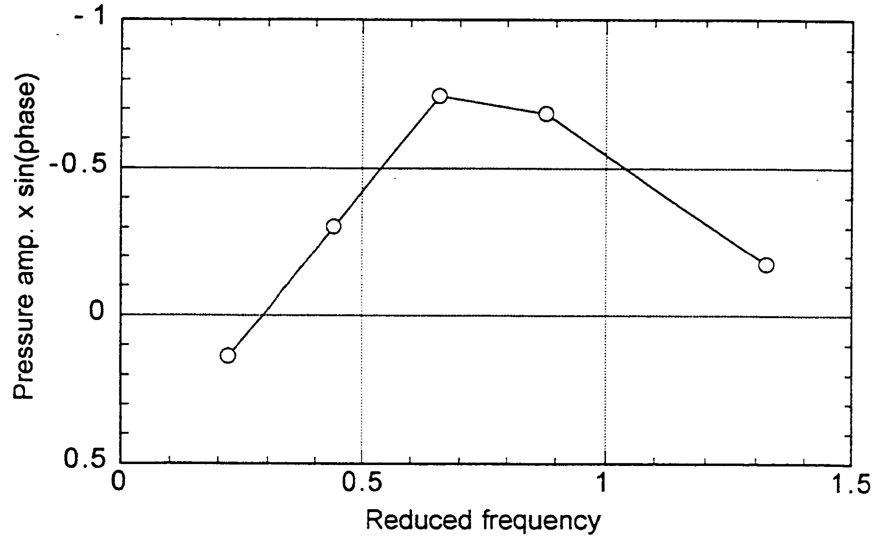

Figure 6.26: Aerodynamic stability change due to the reduced frequency

6.9 Effect of Reynolds number

In industry, it is common practice to use scaled rigs to develop engines. In high bypass fan engines, the diameter of the engine is especially large and therefore half-scale fan rigs are often used for aerodynamic performance tests to save cost. In such cases, the tip relative Mach number is matched to the engines, and the Reynolds number cannot be matched. The question in such rig tests is whether the flutter boundaries observed in rig tests represent the flutter of the engine.

Since it has been shown that transonic flutter is caused by the shock wave oscillating between attached and detached positions, the flutter onset can be very sensitive to the Reynolds number. Although the shock position itself is usually thought as not being strongly dependent on the Reynolds number, it is different in transonic cascade flow. Boundary layer thickenings or separations always exist behind the shock foot, and the displacement thickness of the boundary layer will change the passage area behind the shock wave. Since the shock position is very sensitive to the passage area, the onset of the transonic flutter can be very sensitive to the Reynolds number. Calculations at the inter-blade phase angle -32.7 degrees at 91.2% span were performed to check the effect of the Reynolds number. The Reynolds number was increased from 1.77×10^6 to 3.77×10^6 which correspond to that of the rig and the engine, respectively. The calculation results are shown in Fig. 6.27 and Fig. 6.28.

The results show only small variation with Reynolds number. This implies that the passage contraction due to the thickness of the boundary layer does not affect transonic flutter much in this Reynolds number range. Thus, the flutter boundary found in half scale rig tests can be taken as those of engines.

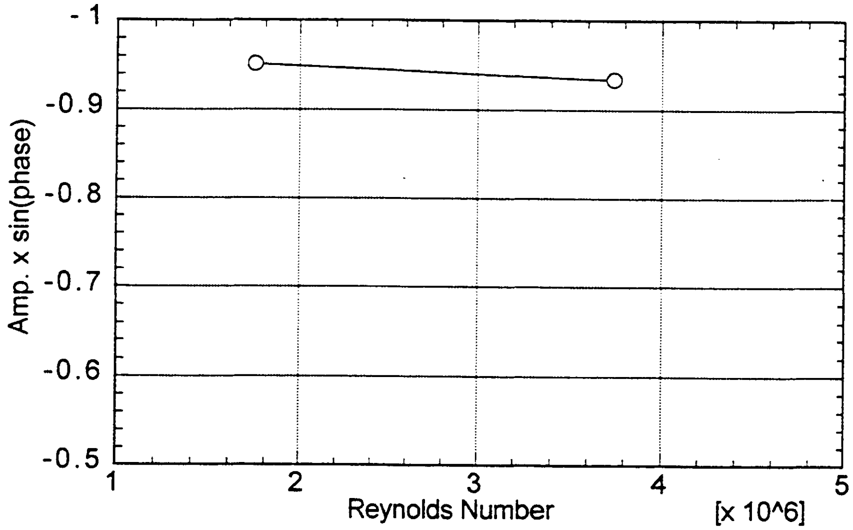

Figure 6.27: Aerodynamic stability change due to the Reynolds number

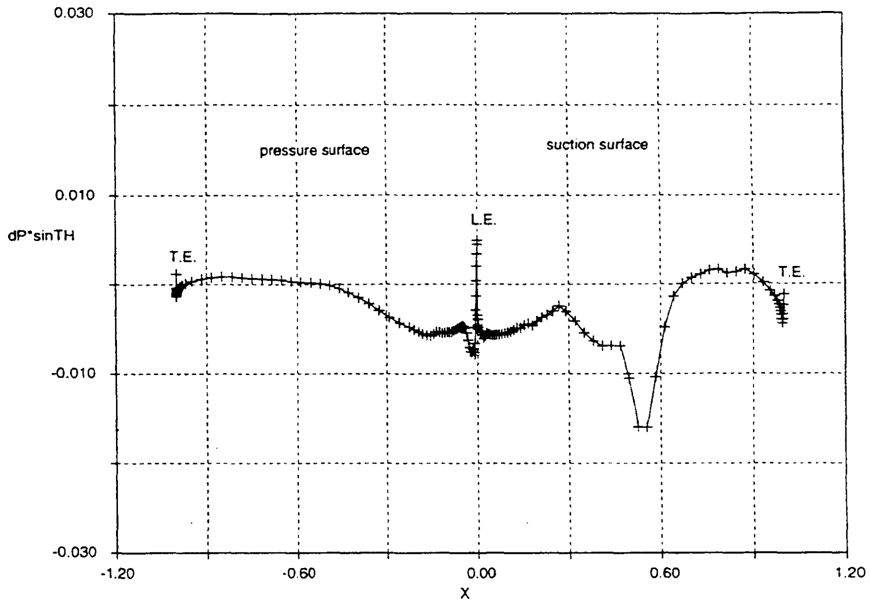

(a) $Re = 1.77 \times 10^6$

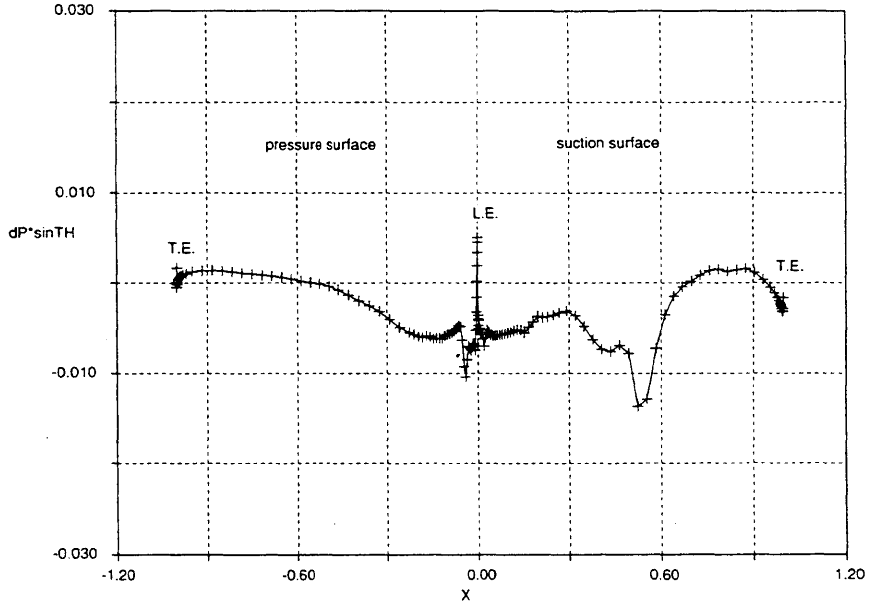

(b) $Re = 3.77 \times 10^6$

Figure 6.28: Effect of Reynolds number on blade surface energy distribution (91.2% span, $\sigma = -32.7 degrees$, low valve)

6.10 Spanwise variation and total blade exciting energy

So far, all the calculations were done at the 85.3% span position, and 2-dimensional aerodynamic mechanisms of flutter were explored only at this position. Although the possibility of flutter was found by such a "typical section" approach, this will not yield the flutter boundary of the real fan. In reality, the flow field in a transonic fan is 3-dimensional, and the fan will flutter only when the total unsteady energy moment on a whole blade becomes unstable. To get the flutter boundary of the whole blade, one should evaluate the total blade exciting energy moment by summing the blade exciting energy at each section after multiplying it by the distance of the section from the root of the blade. This is called the "strip theory" approach.

It is generally believed that the spanwise section above 70% span has the dominant influence on the total blade exciting energy since the unsteady aerodynamic force is large due to high relative Mach number, and the moment arm from the root of the blade is long. Therefore, for the strip theory calculation, only three spanwise sections, namely 79.3% span, 85.3% span, and 91.2% span were used. 95.3% span section was omitted because large three dimensionality due to the end wall and tip clearance flow was anticipated.

The blade exciting energies on the three sections to use in the strip theory approach are shown in Fig. 6.29. The stability is minimum at 85.3% span and the blade exciting energy is seen only at this position at the pressure ratio 1.32. The reasons can be seen in the timewise blade surface pressure distribution in Fig. 6.30, and in the blade surface unsteady energy distribution in Fig. 6.31. At 91.2% span, the shock wave is located closer to the trailing edge and is weaker than for the 85.3% span case. Although a small blade exciting energy is seen at the downstream of the shock foot on the suction surface, the blade exciting energy due to the shock foot on the pressure surface has weakened and the total blade exciting energy at the section has become a blade damping energy. At 79.3% span the shock wave is detached and no blade exciting energy due to a shock foot on the pressure surface is seen. The mechanism of the blade exciting energy change due to the spanwise position variation is similar to that due to the static pressure ratio variation. The key mechanism is that the blade exciting aerodynamic energy due to the shock foot on the pressure surface emerges when the shock wave is just about to detach. This matches the observation that the flutter appeared only when the fan is operating at a tip relative Mach number over unity.

In a transonic fan operating with the tip Mach number over unity, a spanwise position at which the shock wave detaches always exists. Therefore transonic fans can have an aerodynamically unstable radius whenever the tip Mach number exceeds unity.

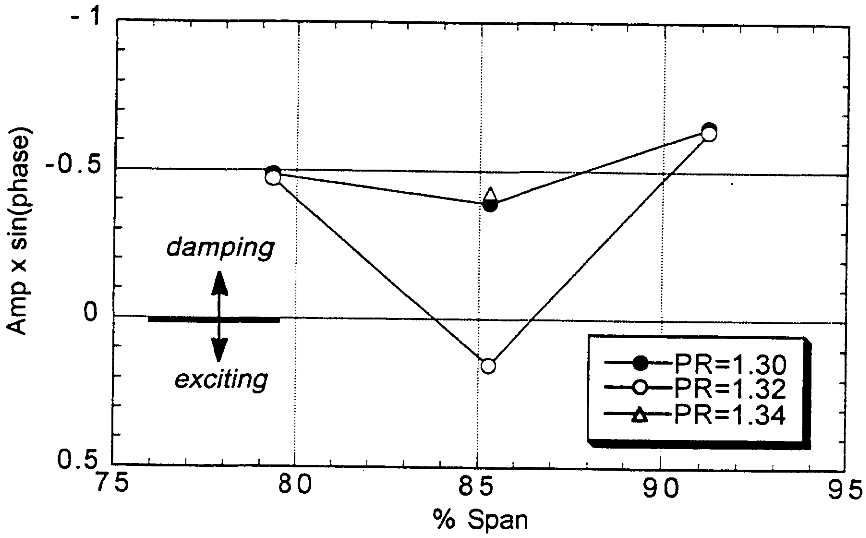

Figure 6.29: Aerodynamic stability change due to the spanwise position

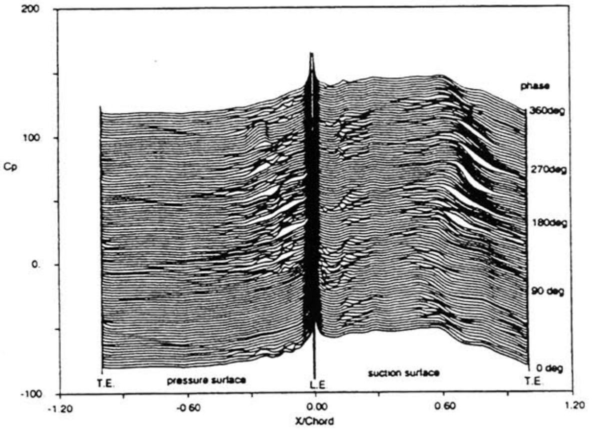

(a) 91.2% span

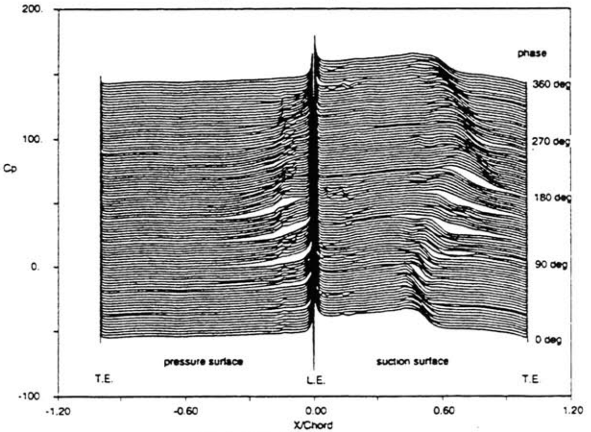

(b) 85.3% span

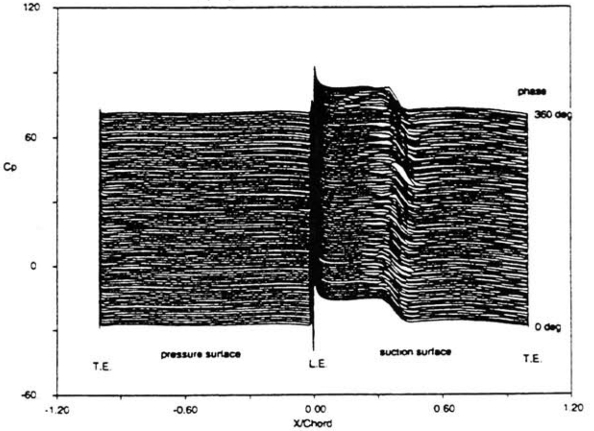

(c) 79.3% span

Figure 6.30: Spanwise variation of the timewise blade surface pressure distribution (inter-blade phase angle -32.7 degree, π = 1.32)

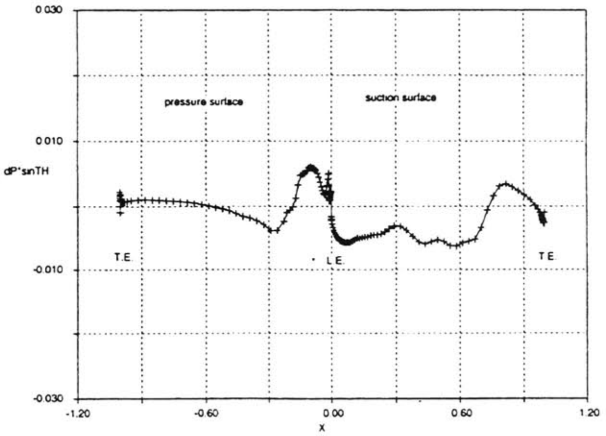

(a) 91.2% span

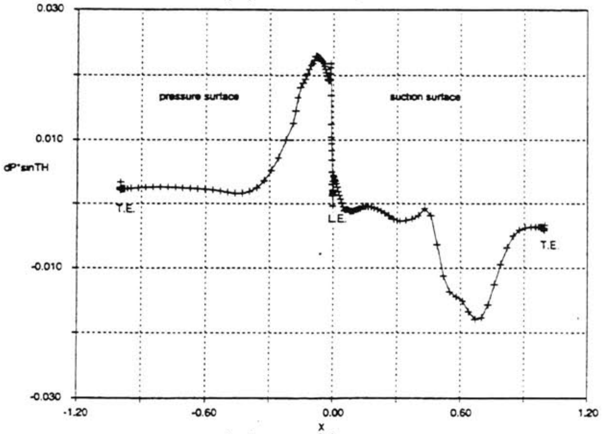

(b) 85.3% span

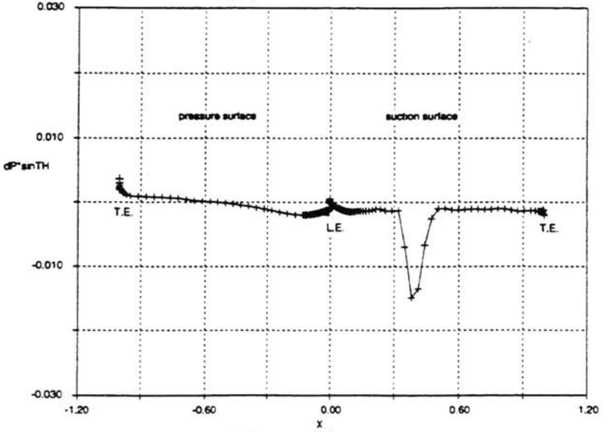

(c) 79.3% span

Figure 6.31: Spanwise variation of the blade surface aerodynamic stability distribution
(inter-blade phase angle -32.7 degree, $\pi = 1.32$)

The spanwise integrated energy moments at several different pressure ratios are plotted in Fig. 6.32. Since the blade exciting energy was seen only at 85.3% span pressure ratio 1.32 case, no blade total exciting energy moment is calculated. The reason for this mismatch with the rig result is not clear now. The research to find this reason may need full 3-D calculations, and therefore is left as a research topic for future. To use the current code for practical flutter boundary predictions, a "typical section" approach calibrated by a certain data point appears to be acceptable.

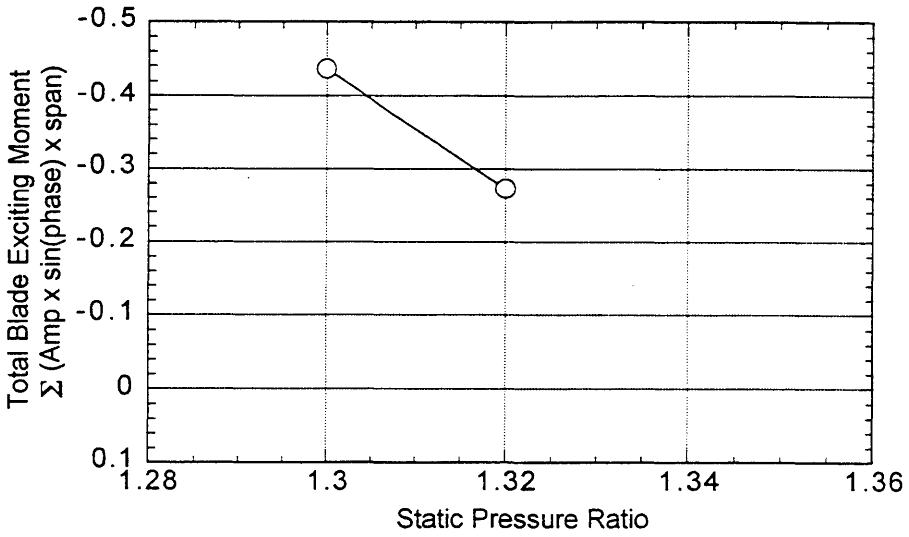

Figure 6.32: Total blade exciting force variation

6.11 Summary of the flutter mechanism at 79% speed

An unsteady quasi-3D viscous calculation has demonstrated the aerodynamic mechanisms of the flutter at high loading condition in an IHI transonic fan. For the transonic fan oscillating in bending mode, the dominant unsteady aerodynamic energies are generated by the unsteady pressure at the shock feet on both suction and pressure surfaces due to the passage shock. The shock foot on the suction surface works as a blade damping energy, but that on the pressure surface works as a blade exciting energy at the inter-blade phase angle observed in the rig flutter test, -32.7 degrees. The sum of these two energies determines the stability of the blade section.

The instability of the shock wave becomes large just before it detaches, and the shock oscillates at a large chordwise displacement. The foot of this oscillating shock wave on the pressure surface of the blade exerts the dominant blade exciting energy. Therefore the flutter boundary is sensitive to the position of the shock wave and to the pressure ratio, because the pressure ratio affects the position of the shock wave. Transonic flutter will be resumed when the shock wave is fully detached because there is no shock foot on the pressure surface, and the shock oscillation reduces.

The flutter observed in an IHI transonic fan has been demonstrated to not be a stall flutter. It is the unsteady pressure due to the large oscillation of the passage shock wave which generates the large blade exciting energy, and not the separation behind the shock wave.

If the pressure ratio is further increased, and/or the incidence angle become large, a classical stall flutter due to trailing edge separation may emerge, overwhelming transonic flutter. For sophisticated modern fan designs, a transonic flutter due to the shock unstarting appears to occur first. This mechanism explains why it was sometimes observed at conditions around the kink in the flutter boundary plot, that flutter subsided by further closing the fan exit valve during the rig tests.

The reduced frequency was found to have large effect on this flutter. Increase of the natural frequency of the blades is an efficient method to suppress this flutter.

The Reynolds number was found not to have a large influence on the flutter boundary. Therefore a scaled rig test can represent the flutter boundary of the engine as far as the material and the structure of the blade are the same and the reduced frequency is not changed.

When strip theory was applied to the results of the calculations, this research indicated no flutter under any conditions. To use current code for practical flutter boundary prediction, a "typical section" approach with calibration to a certain data point is recommended.

Chapter 7

Summary and conclusions

7.1 Summary of the work

1. A quasi-3D viscous unsteady code has been developed to calculate the blade-to-blade flow of a modern transonic fan with shock waves. The code has been validated by a series of calculations so that the result of calculations can be trusted as representing physically true phenomena.

2. Johnson and King's one-half equation turbulence model has been implemented in the code. It performed well on simulating the shock/boundary-layer interaction on a transonic blade section. Laminar calculations and turbulent calculations with an equilibrium model such as Cebeci-Smith's gave totally different flow fields which was inconsistent with experiments. The importance of choosing the proper turbulence model has been shown.

3. The importance of properly modeling the motion of transition points in unsteady calculations has been shown. In steady calculations, the e^n method is sufficient to model the transition point, but in unsteady calculations it has been shown that a model which simulates the streamwise shedding of the transition point is needed.

4. The ability to use a quasi-3D code for simulating the unsteady blade-to-blade flow in modern transonic fan has been demonstrated. The calculation by "typical section" approach showed that the largest aerodynamic instability occurred at the same inter-blade phase angle as seen in the flutter of the rig test. Also, the calculation confirmed that a blade-exciting aerodynamic energy appears at the boundary condition taken from the rig data when the flutter occurred.

7.2 Conclusions

Mechanisms and characteristics of a transonic fan flutter at a high loading condition have been shown by quasi-3D unsteady viscous calculations.

1. The flutter observed in the IHI fan rig was found not to be a classical stall flutter, but it is a flutter due to shock oscillation. While the shock oscillation produces a dominant blade exciting energy, the separation behind the shock foot was found to not produce a blade exciting aerodynamic energy during the flutter.
2. The shock wave has been found to be playing an important role in the mechanisms of this flutter.
   (a) The key mechanism of the transonic fan flutter lies in the oscillation of the shock wave as it detaches. At a pressure ratio close to the value at which the shock wave detaches, the stability of the shock wave reduces, and the shock wave oscillates between the started and the unstarted positions with minor blade oscillation. At such a condition, the unsteady blade surface pressure on the pressure surface generated by the foot of the passage shock wave becomes a dominant blade oscillating force.
   (b) The unsteady blade surface pressure at the shock foot on the suction surface works as a blade damping force when the flutter occurred.
   (c) Flutter due to the shock oscillation will occur at conditions near the shock unstarting point. This kind of flutter will not occur when the shock wave is fully detached.
3. The effect of Reynolds number on the flutter is small. No appreciable difference was seen in the blade exciting energy when the Reynolds number was changed from 1.77×10^6 to 3.77×10^6. Therefore a flutter test by a scaled rig will represent the flutter boundary of the engine.
4. The reduced frequency has large effect on this flutter. As with other type of flutters in a cascade, an increase of the natural frequency of the blade is effective to suppress the flutter.

5. The mechanism of the flutter is unsteady, and therefore quasi-steady analysis is not a proper approach to analyze this flutter.

7.3 Recommendations for future work

1. A study on the effect of the blade design parameters, such as the camber angle, stagger angle, and the curvature of the blade passage between unstarted position and the started position is suggested to develop a method to design a transonic fan that is much more robust to high loading flutter.

2. Three dimensional effects, such as unsteady passage contraction, end-wall boundary layers, tip-clearance vortices, and spanwise slanted shock waves should be checked by full 3D calculations.

3. Spanwise integration of the unsteady aerodynamic energy, i.e. strip theory, did not show flutter at the conditions studied. The reason why it did not show flutter should be clarified. This work may need 3D calculations.

4. Unsteady viscous calculations with multiple blade passages take a tremendously long time even with today's high speed workstations. Methods to reduce the calculation time are very important from a practical point of view. Some possibilities worth trying to shorten the calculation time are:

   (a) parallelize the code to run over multiple workstations, and

   (b) use a better grid, such as an O-H grid to improve the numerical stability of the calculations.

Bibliography

[1] S. R. Allmaras. *A Coupled Euler/Navier-Stokes Algorithm for 2-D Unsteady Transonic Shock/Boundary-Layer Interaction.* M.I.T. GTL Report No.196, March 1989.

[2] D. A. Anderson, J. C. Tanhill, and R. H. Pletcher. *Computational Fluid Dynamic and Heat Transfer.* Hemisphere Publishing Co., 1984.

[3] A. Bölcs and T. H. Fransson, editors. *Aeroelasticity in Turbomachines, Comparison of Theoretical and Experimental Cascade Results, Communication du Laboratoire de Thermique Appliquée et de Turbomachines Nr. 13*, chapter 7. Seventh Standard Configuration. École Polytechnique Fédérale de Lausanne, 1986.

[4] T. Cebeci and A. M. O. Smith. *Analysis for Turbulent Boundary Layers.* Academic Press, 1974.

[5] M. R. Chi. *Unsteady Aerodynamics in Stalled Cascade and Stall Flutter prediction.* ASME 80-C2/Aero-1, August 1980.

[6] T. J. Coakley. *Turbulence Modeling methods for the Compressible Navier-Stokes Equations.* AIAA-83-1693, 1983.

[7] J. A. Ekaterrinaris and M. F. Platzer. "Progress in the Analysis of Blade Stall Flutter." In *7th International Symposium of Unsteady Aerodynamics and Aeroacoustics in Turbomachines*, pp. 287–302, Elsevier, 1994.

[8] A. H. Epstein, J. B. Gertz, P. R. Owen, and M. B. Giles. "Vortex Shedding in High-Speed Compressor Blade Wakes." *AIAA Journal of Propulsion and Power*, 4(3):236–244, May-June 1988.

[9] J. I. Erdos, E. Alzner, and W. McNally. "Numerical Solution of Periodic Transonic Flow Through a Fan Stage." *AIAA Journal*, 15(11):1559–1568, November 1977.

[10] M. B. Giles. *A Numerical Method for the Calculation of Unsteady Flow in Turbomachinery.* M.I.T. GTL Report No.205, May 1991.

[11] M. B. Giles. *Numerical Methods for Unsteady Turbomachinery Flow.* M.I.T. CFDL-TR-89-3, April 1989.

[12] J. P. Gostelow. *Cascade Aerodynamiocs.* Pergamon Press, 1984.

[13] D. A. Johnson and T. J. Coakley. "Improvements to a Nonequilibrium Algebraic Turbulence Model." *AIAA Journal*, 28(11):2000–2003, November 1990.

[14] D. A. Johnson and L. S. King. *A Mathematically Simple Turbulence Closure Model for Attached and Separated Turbulenct Boundary Layers.* AIAA-84-0175, Jan 1984.

[15] H. Joubert. *Supersonic Flutter in Axial Flow Compressors.* Unsteady Aerodynamics of Turbomachines and Propellers, Sept 1984.

[16] M. M. Rai. *Unsteady Three-dimensional Navier-Stokes Simulations of Turbine Rotor-Stator Interaction.* AIAA-87-2058, June 1987.

[17] R. E. Riffel and M. D. Rothrock. *Experimental Determination of Unsteady Blade Element Aerodynamics in Cascades; Torsional Mode Final Report.* NASA CR-159831, 1980.

[18] P. L. Roe. *Characteristic-Based Schemes for the Euler Equations*, pp. 337–365. Vol. 18, ARF, 1986.

[19] G. B. Schubauer and P. S. Klebanoff. *Contributions on the Mechanics of Boundary-Layer Transition.* NACA Rep. 1289, 1956.

[20] F. Sisto. *AGARD manual on Aeroelasticity in Axial-Flow Turbomachines, AGARDograph No. 298*, chapter 7, Stall Flutter. Vol. 1, Unsteady Turbomachinery Aerodynamics, AGARD, 1987.

[21] F. Sisto. "Stall-Flutter in Cascades." *Journal of the Aeronautical Science*, 20(9):598–604, Sept 1953.

[22] F. Sisto, W. Wu, S. Thangam, and S. Jonnavithula. "Computational Aerodynamics of Oscillating Cascades with the Evolution of Stall." *AIAA Journal*, 27(4):462–471, April 1989.

[23] P. R. Spalart. *Two Recent Extensions of the Vortex Method.* AIAA-84-0343, Jan 1984.

[24] P. R. Spalart and S. R. Allmaras. *A One-Equation Turbulence Model for Aerodynamic Flows.* AIAA-92-0439, January 1992.

[25] H. Stargardter. *Subsonic/Transonic Stall Flutter Study.* NASA CR-165256, June 1979.

[26] H. Starken and H. A. Schreiber. *Test Cases for Computation of Internal Flows in Aero Engine Components, AGARD-AR-275*, chapter V.4 Test Case E/CA-4: Low supersonic compressor cascade MCA. AGARD, 1990.

[27] A. J. Strazisar, J. R. Wood, M. D. Hathaway, and K. L. Suder. *Laser Anemometer Measurements in a Transonic Axial-Flow Fan Rotor.* NASA TP-2879, Nov 1989.

[28] E. Szechenyi. *AGARD manual on Aeroelasticity in Axial-Flow Turbomachines, AGARDograph No. 298*, chapter 10, Understanding Fan Blade Flutter Through Linear Cascade Aeroelastic Testing. Vol. 1, Unsteady Turbomachinery Aerodynamics, AGARD, 1987.

[29] B. van Leer, W. Lee, and K. G. Powell. *Sonic-Point Capturing.* AIAA-89-1945, 1989.

[30] F. M. White. *Viscous Fluid Flow.* McGraw Hill, 1974.

[31] D. S. Whitehead. *AGARD manual on Aeroelasticity in Axial-Flow Turbomachines, AGARDograph No. 298*, chapter 3, Classical Two-Dimensional Methods. Vol. 1, Unsteady Turbomachinery Aerodynamics, AGARD, 1987.

[32] S. Yashima and H. Tanaka. *Torsional Flutter in Stalled Cascade.* ASME 77-GT-72, March 1977.

[33] H. H. Youngren. *Analysis and Design of Transonic Cascades with Splitter Vanes.* MIT GTL Report #279, February 1991.